

Investigation of transport phenomena of thermal acoustic
excitations in semi-crystalline and amorphous materials
using transient grating spectroscopy

Thesis by
Taeyong Kim

In Partial Fulfillment of the Requirements for the
Degree of
Doctor of Philosophy

The logo for the California Institute of Technology (Caltech), featuring the word "Caltech" in a bold, orange, sans-serif font.

CALIFORNIA INSTITUTE OF TECHNOLOGY
Pasadena, California

2020
Defended August 27, 2020

© 2020

Taeyong Kim

ORCID: 0000-0003-2452-1065

All rights reserved

ACKNOWLEDGEMENTS

Throughout my six-year journey for my graduate study at Caltech, I have been fortunate for being helped by many great people. Without their support, I would not have been able to complete my thesis work. I cannot list all the names here, but I would like to express my sincere gratitude to all of them.

First and foremost, I would like to present my sincere thank to my academic advisor, Prof. Austin Minnich for his unconditional support, passion and patience. When I just joined his group, he helped me by walking me through thermal science, which I would never forget. He always dedicated his time and efforts to advise me, which, for me, became a source for overcoming any risky challenges that I had, especially when I got lost. I am grateful to him for the discussions that I had with him, from which I was able to improve my scientific insights. Not only as a researcher, but also as a mentor, Austin was my role model. I sincerely thank him for constantly encouraging me during my years at Caltech, and for providing me advice on my career paths when I became a senior graduate student.

I would like to thank Prof. Brent Fultz, Prof. Kerry Vahala, and Prof. Andrei Faraon, who graciously serve on my dissertation committee, for providing useful comments and discussions for my works over many years.

I wish to acknowledge the financial support from the Jeongsong graduate fellowship, Light-Material Interactions in Energy Conversion Energy Frontier Research Center (LMI-EFRC) at Caltech, GIST-Caltech Research Collaboration, and Office of Naval Research.

I benefited from the support of many people at Caltech. I thank the Joint-Center for Artificial Photosynthesis (JCAP) for allowing me to build a time-resolved setup. Thank you to the post-docs and students at JCAP, especially to Dr. Ke Sun, and Dr. Stefan Omelchenko. I also wish to acknowledge Kavli Nanoscience Institute (KNI) for letting me use their great facilities. Thank you to the staff members at KNI, especially Matthew Hunt and Nathan Sangkook Lee. I also want to thank Dr. Tiziana Luccio in Prof. Julie Kornfield's group for fruitful discussions. I am also grateful to Prof. Harry Atwater and his research group for allowing me to use their research facilities. Thank you to the staff members at Caltech for their support: Sonya Lincoln, Jennifer Blankenship, and Tiffany Kimoto.

I had the good fortune of collaborating with many researchers from various institutes.

Thanks to my collaborators for providing me a lot of a great source for my research. I am grateful to Prof. Young-dahl Jho, and Dr. Jong-Hyuck Yim at Gwangju Institute of Science and Technology (GIST) in South Korea. I am also thankful to Prof. Sara Ronca, Prof. Ignacio Martin-Faviany, and Dr. Stavros Drakopoulos at Loughborough University in the UK. I am grateful to Prof. Clivia Sotomayor-Torres and her group at Catalan Institute of Nanoscience and Nanotechnology (ICN2) in Spain. I thank Prof. Brian Daly at Vassar College for useful discussions on sound attenuation measurements.

For the past six years, I have been able to work with past and contemporary Minnich lab members. Thank you to Andrew Robbins, Ding Ding, Nate Thomas, Nick Dou, Chengyun hua, Navaneetha Ravichandran, Junlong Kou, Xiangwen Cheng, and Jaeyun Moon. Particularly, I would like to express my sincere thanks to Andrew Robbins and Ding Ding, without whom many parts of my thesis would not have been made. I also would like to acknowledge current Minnich group members: Alex Choi, Peishi Cheng, Adrian Tan, Erika Ye, Shi-Ning Sun, Zoila Jurado, and other members.

I thank friends at Caltech for their friendships. Thanks to many Korean friends at Caltech, especially Jaeyun Moon, Myung-gyun Suh, Jeeseon Choi, Yonil Jung, Chang Ho Sohn, Youngjoon Choi, Dennis Sungtae Kim, Areum Kim, Gunho Kim, Hyun-Gi Yoon, Kyuhyun Lee, Yonghwi Kim, Dr. Sonjong Hwang, and Dr. Byung-kuk Yoo. Thank you all to other friends at Caltech, especially to John Pang, Jinglin Huang, Hengjiang Ren, and Ke Ke. A special thanks to Daniel Naftalovich for being my terrific roommate in my first year at Caltech, and for a life-long friendship.

Last, but not the least, I sincerely thank my family for their love, support, and the sacrifices that they had to make for me. I would like to thank my mom, dad, and my sister without whom I would not have been able to be a grown up. Thanks to you, I was able to endure many ups and downs during my doctoral years.

ABSTRACT

The physics of transport of heat-carrying atomic vibrations in amorphous and semi-crystalline solids is a topic of fundamental interest. Diverse tools have been employed to study thermal transport in these materials, including cryogenic thermal conductivity measurements and various inelastic scattering tools. However, unambiguously identifying the damping mechanisms of few THz and smaller frequency excitations remains difficult owing to the lack of the experimental probes in the frequency band. As a result, debate has remained regarding the microscopic origin of weak acoustic damping in amorphous silicon (Si), the unusually high thermal conductivity of ultra-drawn polyethylene, and other topics.

In this thesis, we investigate the transport properties of heat-carrying acoustic excitations in semi-crystalline and amorphous solids using transient grating spectroscopy. This optical method permits the creation of thermal gradients over sub-micron length scales which may be comparable to the attenuation lengths of the excitations. We show how these measurements can be used to constrain the damping mechanisms in the sub-THz range that has been historically inaccessible by typical methods such as inelastic scattering.

First, we report measurements of the bulk thermal conductivity and elastic properties of MoS₂ thin films. Specifically, we use TG to measure the in-plane longitudinal sound velocity and thermal conductivity. We do not observe any size effects of thermal conductivity with grating period, indicating that the propagating distance of heat-carrying acoustic phonons are smaller than the thermal length scale accessible in the experiment. This result is consistent with the mean free paths predicted from ab-initio numerical methods.

Second, we utilize the capability of TG to resolve the microscopic heat transport properties of phonons in highly oriented semi-crystalline polyethylene (PE). Earlier experimental studies have reported thermal conductivities of up to $\sim 100 \text{ Wm}^{-1}\text{K}^{-1}$ in crystalline polyethylene, orders of magnitude larger than the bulk value of $\sim 0.4 \text{ Wm}^{-1}\text{K}^{-1}$. However, the microscopic origin of the high thermal conductivity remains unclear. We address this question by applying TG to highly oriented polyethylene to show that mean free paths on micron length scales are the dominant heat carriers. Using a low-energy anisotropic Debye model to interpret these data, we find evidence of one-dimensional phonon density of states for ex-

citations of frequency less than ~ 2 THz. This transition frequency is consistent with the unique features of ultradrawn PE, in particular the stiff longitudinal branch leading to wavelengths of 8 nm at 2 THz frequency; and fiber diameters < 10 nm observed in prior structural studies of ultradrawn polymers; so that the wavelength does indeed exceed the fiber diameter at the relevant frequencies.

Finally, we report the measurements of the frequency-resolved mean free path of heat-carrying acoustic excitation in amorphous silicon (aSi), for the first time. The heat-carrying acoustic excitations of amorphous silicon are of interest because their mean free paths approach the micron scale at room temperature. Despite extensive investigation, the origin of the weak acoustic damping in the heat-carrying frequencies remains a topic of debate for decades. A prior study suggested a framework of classifying the vibrations into propagons, diffusons, and locons. Propagons were considered phonon-like, delocalized, propagating vibrations; locons as localized vibrations, and diffusons as delocalized yet non-propagating vibrations. Following the framework, numerous works have predicted mechanism of acoustic damping in aSi, but the predictions have contradicted to observations in experiments. In this work, we obtained measurements of the frequency-dependent mean free path in amorphous silicon thin films from $\sim 0.1 - 3$ THz and over temperatures from 60 - 315 K using picosecond acoustics (PSA) and transient grating spectroscopy. We first describe our PSA experiments to resolve the attenuation of 0.1 THz acoustic excitations in aSi. We then present our table-top approach to resolve MFP of heat-carrying acoustic excitation between $\sim 0.1 - 3$ using TG spectroscopy. The mean free paths are independent of temperature and exhibit a Rayleigh scattering trend over most of this frequency range. The observed trend is inconsistent with the predictions of numerical studies based on normal mode analysis, but agrees with diverse measurements on other glasses. The micron-scale MFPs in amorphous Si arise from the absence of Akhiezer and two-level system damping in the sub-THz frequencies, leading to heat-carrying acoustic excitations with room-temperature damping comparable to that of other glasses at cryogenic temperatures. Our results allow us to establish a clear picture for the origin of micron-scale damping in aSi by understanding vibrations as acoustic excitation rather than propagons, diffusons, and locons.

PUBLISHED CONTENT AND CONTRIBUTIONS

- [1] Ding Ding, Taeyong Kim, and Austin J. Minnich. Active thermal extraction of near-field thermal radiation. *Phys. Rev. B*, 93:081402, 2 2016. doi: 10.1103/PhysRevB.93.081402. URL <https://link.aps.org/doi/10.1103/PhysRevB.93.081402>.
T.K. conducted the calculations, and analyzed the results.
- [2] Ding Ding, Taeyong Kim, and Austin J. Minnich. Active thermal extraction and temperature sensing of near-field thermal radiation. *Scientific Reports*, 6(1): 32744, 2016. doi: 10.1038/srep32744. URL <https://doi.org/10.1038/srep32744>.
T.K. conducted the calculations, and analyzed the results.
- [3] Taeyong Kim, Ding Ding, Jong-Hyuck Yim, Young-Dahl Jho, and Austin J. Minnich. Elastic and thermal properties of free-standing molybdenum disulfide membranes measured using ultrafast transient grating spectroscopy. *APL Materials*, 5(8):086105, 2017. doi: 10.1063/1.4999225. URL <https://doi.org/10.1063/1.4999225>.
T.K. prepared the experimental data, analyzed the results, and participated in the writing of the manuscript.
- [4] Taeyong Kim, Jaeyun Moon, and Austin J. Minnich. Origin of micron-scale propagation lengths of heat-carrying acoustic excitations in amorphous silicon. July 2020. URL <https://arxiv.org/abs/2007.15777v1>.
T.K. participated in the conception of the project, prepared the experimental data, analyzed the results, and participated in the writing of the manuscript.
- [5] Taeyong Kim, Andrew B. Robbins, Stavros X. Drakopoulos, Ignacio Martin-Fabiani, Sara Ronca, and Austin J. Minnich. Heat-carrying phonons with micron-scale mean free paths in highly oriented polyethylene (in preparation).
T.K. participated in the conception of the project, prepared the experimental data, analyzed the results, and participated in the writing of the manuscript, 2020.
- [6] Stavros X. Drakopoulos, Georgios C. Psarras, Aurora Nogales, Tiberio A. Ezquerro, Taeyong Kim, Andrew B Robbins, Austin J. Minnich, Georgia C. Manika, Gianfranco Claudio, Ignacio Martin-Fabiani, and Sara Ronca. Gold/ultra high molecular weight polyethylene nanocomposites for electrical energy storage: Enhanced recovery efficiency and thermal conductivity upon uniaxial deformation (in review).
T.K. prepared the thermal characterization data, analyzed the thermal characterization results, and participated in the writing of the manuscript, 2020.

CONTENTS

Acknowledgements	iii
Abstract	v
Published Content and Contributions	vii
Bibliography	vii
Contents	vii
Chapter I: Introduction	1
Chapter II: Introduction to transient grating spectroscopy	9
2.1 Fundamentals	9
2.2 Signal monitoring via heterodyne detection	12
2.3 Thermal signal traces and fitting	15
2.4 TG arrangements	16
2.5 Summary	19
Chapter III: In-plane elastic and thermal properties of Molybdenum disulfide	21
Bibliography	21
3.1 Ultrafast transient grating	21
3.2 Material: Molybdenum disulfide	28
3.3 TG experiments on MoS ₂	31
3.4 Summary	37
Chapter IV: Heat-carrying phonons with micron-scale mean free paths in highly oriented polyethylene	39
Bibliography	39
4.1 Background	39
4.2 Bulk thermal property of PE	42
4.3 TG application on highly oriented PE	44
4.4 Grating period dependent thermal conductivity	51
4.5 Ballistic transport of the heat-carrying phonons in DR196	53
4.6 Low energy Debye model	58
4.7 Modeling	58
4.8 Discussion	62
4.9 Summary	64
Chapter V: Origin of acoustic excitations in amorphous silicon	65
Bibliography	65
5.1 Motivation	65
5.2 Anomalous thermal properties observed in amorphous materials	67
5.3 Prior empirical models	71
5.4 Picosecond sound acoustics (PSA) on aSi	76
5.5 Thermal characterization of aSi	83
5.6 Unusually weak damping of acoustic excitation in aSi	94
5.7 Summary	97

Chapter VI: Conclusion and future works	98
6.1 Summary	98
6.2 Outlook and future insight	99
Bibliography	102

Chapter 1

INTRODUCTION

Thermal conductivity of polymers and amorphous materials

Bulk amorphous dielectric materials and polymers are of importance for modern device applications due to unusual properties compared to their crystalline counterparts. For instance, owing to cost-effectiveness and chemical stability combined with excellent electronic and optical properties, these substances have been used in various applications such as photovoltaic solar cells, gate dielectrics for transistors, channel materials for thin-film transistors, and mini-channel heat exchangers [1–3].

Concerning the thermal perspective, polymers were traditional thermal insulator materials. Due to the lack of long-range structural order, thermal conductivity on the order of $\sim 0.1 \text{ Wm}^{-1}\text{K}^{-1}$ was reported [4]. Contrary to the traditional understanding, some of earlier studies have reported orders of magnitude increase. For instance, a factor 6 of increase in thermal conductivity was observed in stretched polyacetylene [5]. Several other studies have also reported observed thermal conductivity enhancement in polymethylmethacrylate (PMMA), polyethylene (PE), polypropylene, and polyethylene [6–8].

Despite great strides that have been made, its microscopic origin that leads to these dramatic changes is poorly understood. For instance, some of the prior works have argued that overall thermal conductivity increase originates from a substantial increase in the amorphous fraction, while the others demonstrated the opposite reports. For instance, Xu and Chen have shown that the thermal conductivity of 110 times stretched PE is as high as $60 \text{ Wm}^{-1}\text{K}^{-1}$ with amorphous contribution 25% [9]. Similar conclusion was drawn for oriented amorphous polythiophene [10]. On the other hand, Ronca and Rastogi measured thermal conductivity of 220 times stretched PE to be around $50 \text{ Wm}^{-1}\text{K}^{-1}$, but with substantial contribution from crystalline domain 94%.

Mechanism of the damping of the low energy excitations in amorphous silicon (aSi) is another topic under debate for more than 20 years due to unusual properties compared to other glasses. In most glasses, earlier works have shown that the thermal vibrational mean free path (MFP), an average travel distance before the scattering, is of order of nanometers due to the lack of long-range order. Due to the similar-

ity in the bulk properties of the glassy substances, corresponding mechanism of the damping of the vibration was considered to be universal. However, the experimental observations in aSi indicate that the aSi is an unusual glass due to the following reasons: First, some experiments have measured the thermal conductivity of aSi as high as $4 \text{ Wm}^{-1}\text{K}^{-1}$, which is anomalously high compared to the values in typical glassy substances. Second, recent experiments reported an evidence that heat-carrying acoustic excitations in aSi can propagate micron-length distances [11]. Third, there is some experimental evidence that the excess heat capacity at low temperature, a characteristic of the glassy materials, is not present in amorphous silicon [12]. A classification of the vibrations was formulated to explain the damping of vibrations: propagons, diffusons, and locons [13, 14]. Various numerical approaches have demonstrated diverse arguments under this classification, but the predictions have yielded discrepancies with the experimental results. For instance, measured MFP of 100 GHz acoustic excitation in aSi is of order of $10 \mu\text{m}$ [15], an order of magnitude higher than the numerical prediction [16].

Prior experiments have strived to identify damping mechanisms of acoustic excitations as an origin of the bulk thermal properties. Experimentally resolving the damping of the acoustic vibrations is of significant challenging due to the lack of experimental probes. To be specific, amorphous silicon and semi-crystalline polymers are typically fabricated as a thin-film, therefore difficult to be studied by in-elastic neutron scattering and in-elastic x-ray scattering. Although a considerable amount of the volumes of the samples would be provided, the instrumental resolution of in-elastic x-ray scattering is not sufficient to probe excitations with low frequencies. More precisely, kinematic constraints complicate the measurement of the dispersion and broadening of low energy excitations. Overall, these experimental challenges highlight a need for an experimental probe that can probe the dynamics of the low energy excitations.

Traditional approach to infer mean free path

Traditionally, the transport properties of the low energy excitations were estimated based on thermal transport measurements. The theory of the heat conduction is based on phonons as the dominant microscopic heat carriers, collective vibrational excitations arisen by periodic arrangements of consisting atoms. The thermal conductivity of a bulk material is well-described by the kinetic theory, given by

$$\kappa(T) = \int_s C_s(\omega) v_s(\omega) \Lambda_s(\omega, T) d\omega \quad (1.1)$$

where κ is the thermal conductivity of a solid, index s is the polarization, ω is frequency, C is the heat capacity, v is the group velocity, and Λ is the mean free path (MFP). The kinetic theory (Eq. 1.1) provides two important insights. First, the higher speed of the phonons as well as the longer travel distance results in the higher thermal conductivity. Second, the microscopic properties have a spectrum, therefore the information on the spectrum is a key to understanding corresponding bulk properties.

Earlier studies have used the above relation to infer the MFP. First approach is known as gray approximation which does not consider frequency dependence given in Eq. 1.1. According to this approximation, in SiO₂ for example, the mean free path of the phonons are an order of ~ 50 nm (~ 1 nm) for crystal (amorphous) at room temperature. [17, 18]. Similarly, dominant phonon approximation was employed to analyze the thermal conductivity data. In this approximation, it was assumed that heat at a temperature is predominantly carried by a single phonon mode with a frequency [19]

$$f_{dom} = 4.25 \frac{k_B T}{\hbar} \quad (1.2)$$

where k_B is the Boltzmann constant. Corresponding average phonon mean free path for an isotropic material was estimated to be

$$\Lambda(f = f_{dom}) = \kappa \left[\frac{1}{3} C_v v \right]^{-1} \quad (1.3)$$

where κ is the thermal conductivity of a solid, C_v is the specific heat, and v is the sound velocity. The approximation was primarily used to explain the transport of low frequency excitation in amorphous materials such as vitreous silica, vitreous germanium, and glycerol, as well as amorphous polymers such as polystyrene and polymethylmethacrylate (PMMA) [18–20].

However, as is often discussed in many prior literature, the above estimations are known to typically underestimate the MFP, yielding discrepancies with actual values [21, 22]. In fact, the vibrations of the solids are dispersive; the group velocity decreases as the frequency increases, meaning that the velocity that is used for the above estimation is generally overestimated. Therefore corresponding predictions for C_v and v get underestimated. Second, the lifetimes for the atomic vibrations in solids are highly frequency dependent; high frequency vibrations are typically scattered stronger than low frequency vibrations, which is not accurately captured in the description above. Therefore, the use of the approximations above had been

only limited for analyzing low temperature thermal conductivity data to characterize the damping of the acoustic vibrations.

Another approach to estimate the MFP was from the reduced thermal conductivity in tailored structures. According to prior literature [22, 23], the thermal conductivity of a thin-film with a thickness d is

$$\kappa \sim \kappa_b \left(1 - \frac{3\Lambda}{8d}\right) \quad (1.4)$$

where κ_b , and κ represent thermal conductivity of bulk, thin-film, respectively. This phenomenon is known to be classical size effects of diffuse transport of the phonon at the boundary of the thin-film. Phonon heat conduction based on the observation of the classical size effects was discussed in various literature. As an example, an earlier work changed the thickness of the crystalline silicon down to ~ 100 nm, and reported the presence of phonons with MFP as high as 300 nm, far exceeding the gray approximation [24]. While the approach mentioned above can provide a useful insight on the MFP distribution, direct measurements regarding frequency dependence were challenging, therefore details on microscopic transport were missing.

Experimental methods to obtain mean free path

Conventionally, inelastic x-ray scattering (IXS) and inelastic neutron scattering (INS) has been used for studying acoustic dispersion, as demonstrated in many prior studies [25–27]. Furthermore, INS and IXS showed their potential to probe transport property of the vibrations. More precisely, the technique measures the broadening from dynamic structure factor as a function of the frequency, therefore suggesting an avenue for a better understanding of the microscopic phenomena, [28, 29]. For instance, the INS experiments were applied to a single-crystalline PbTe, an exceptionally low thermal conductivity material with its physical origin previously unknown. The experiments have observed anharmonic coupling among LA, TO, and LO, leading to a strong damping behavior as an origin of such low thermal conductivity [29]. However, as earlier mentioned, the instrumental energy resolution as well as kinematic constraints have impeded the application of IXS and INS toward studying low energy excitations in glassy substances.

Therefore as an alternative, mean free path spectroscopy has emerged as a tool to understand the mean free spectrum in solids [25]. This technique is based on the observation of the ballistic transport of the heat-carrying acoustic vibrations.

A key to this approach is tunable length scale of a temperature gradient that is comparable to the MFPs. If the thermal length scale is far longer than many of the MFPs in the material, the observed thermal conductivity is close to the bulk value. As the thermal length approaches a value close to the MFP, corresponding thermal conductivity becomes suppressed, and deviates from the heat diffusion theory, indicating ballistic transport of the heat-carrying phonons. The physical mechanism for this is ballistic travel of the phonons external to the thermal gradient, therefore resulting in the actual scattering being less likely to occur within the thermal gradient. Corresponding heat flux from a source becomes less than the diffusion theory, resulting in the reduction of the thermal conductivity that depends on the length scale of the heat source [30].

The observation of the ballistic transport improved the understanding of the phonon mean free path spectrum. Earlier experimental studies have varied the thermal length scale in different ways. For example, Koh and Cahill have reported that optical modulation frequency changes the thermal diffusion length across the cross plane, and that the contribution of phonons with MFP longer than the diffusion length to the thermal conductivity is less than predicted [31]. Another approach was reducing the in-plane thermal gradient length. Minnich and Chen varied the diameter of the laser spot size and measured the accumulated thermal conductivity versus the mean free path distribution in crystalline silicon [32].

The heat-source size dependent thermal conductivity further advanced to develop a technique to probe the MFP of the heat-carrying vibrations. As a result of this effort, thermal transient grating spectroscopy (TG) has provided a new insight into understanding the MFPs of the heat carrying phonons in crystals. First measurements of the evidence of the ballistic transport using TG was reported in early 2010's [33]. Johnson and Nelson have measured the MFPs in 400 nm thick silicon membranes [33], and found an evidence of micron length scale MFP in crystalline silicon. Corresponding quantitative analysis based on TG measurements was further provided [34]. In brief, thermal conductivity at a given grating period L_i can be expressed as,

$$\kappa_i = \int_s S(q_i, \Lambda_s) C_s(\omega) v_s(\omega) \Lambda_s(\omega, T) d\omega$$

where index $q_i = 2\pi/L_i$ is the grating wave vector inversely proportional to the thermal length, index s is polarization for phonons, and $S(q, \Lambda)$ is the phonon thermal suppression function accounting for the thermal conductivity reduction

due to the ballistic transport, first introduced by Ref. [34]. Using Eq. 1, Maznev and Nelson have shown that Akhiezer scattering mechanism of the phonons is the dominant process for heat conduction in crystalline silicon [34].

The TG technique was further applied to discover other microscopic heat properties: accumulated thermal conductivity and phonon specularly parameter. Minnich proposed a method to reconstruct accumulated thermal conductivity over mean free path without prior knowledge of the microscopic properties [35]. Minnich in Ref. [35] has shown that Eq. 1 can be re-written as

$$\kappa_i = q_i \int K(x_i) F(\Lambda_\omega) d\Lambda_\omega$$

where $x = (2\pi\Lambda_\omega)/L_i$, $K = -dS/dx$, and $F(\Lambda_\omega) = \int_0^{\Lambda_\omega} f(\Lambda'_\omega) d\Lambda'_\omega$ is the accumulated thermal conductivity. As a method to experimentally reconstruct $F(\Lambda_\omega)$ using Eq. 1, convex optimization was used, and showed an excellent agreement with computational predictions [35]. Other recent work reported that the application of the TG along with the Bayesian statistics can reveal frequency-resolved phonon specularly parameters [36].

Despite a short history of TG, the TG technique showed potential to probe heat-carrying acoustic vibrations in partially oriented semicrystalline polymers [37], suggesting its potential to allow us to study low energy excitations.

In this thesis, we exploit TG's capability as an experimental probe to address challenges for characterizing semi-crystalline and amorphous materials, therefore provide a comprehensive picture of the thermal transport in them.

Outline and scope of the thesis

As discussed, a main challenge for bulk thermal properties in semi-crystalline and amorphous materials is the lack of the experimental probe that enables to access the transport of the low energy excitations. The purpose of this thesis is a better understanding of the damping of the acoustic vibrations using an experimental probe with an appropriate length and time scales required for accessing the dynamics of the excitations. The approach presented in this thesis will provide key insights into revealing the origin of the damping in glassy substances, therefore substantially advance the field of the thermal science.

In chapter 2, we introduce the thermal transient grating (TG). We start from discussing working principles and requirements of TG. We then describe the typical

arrangements of TG and associated advantages in TG. Finally, we apply the TG to measure thermal properties of crystalline silicon thin-film.

In chapter 3, we present measurements of bulk vibrational properties of crystal thin-film. For this purpose, we describe our development of the ultrafast TG spectroscopy to enable to simultaneously measure bulk elastic and thermal properties of crystals. The adaptiveness of the TG to enable ultrafast temporal resolution for detection will be discussed. We then demonstrate measurements of in-plane bulk elastic and thermal properties of MoS₂ using ultrafast TG. First, we begin with our sound velocity measurements, which agrees with ab-initio calculations of longitudinal acoustic phonon group velocity along Γ to K Brillouine zone. The sound velocity will be further compared with prior INS data to demonstrate the frequency range that TG can measure. Next, we report measurements of the thermal conductivity of MoS₂ thin film in which we do not observe grating period dependence. The reason will be further examined based on most recent ab-initio calculation and other experimental results.

In chapter 4, we expand the experimental capability of TG to establish the microscopic picture of the heat transport in highly oriented semi-crystalline polyethylene (PE). We first present results of the bulk thermal conductivity measurements and infer the associated microscopic heat transport properties of partially oriented PE. Next, we move to study highly oriented PE to measure mean free path of heat-carrying vibrations. We demonstrate the evidence of the micron-length scale mean free path using our measurements along with a rigorous analysis using a Bayesian inference. Further, we provide an evidence of one-dimensional propagation of the heat-carrying vibrations using a low-energy anisotropic Debye model. Physical origin of our observation will be discussed under a careful consideration of structure-transport relationships in highly oriented PE.

In chapter 5, we report first measurements of the damping of the heat-carrying acoustic excitation in amorphous silicon (aSi) using picosecond acoustics (PSA) and TG. In this chapter, we seek to elucidate the primary damping mechanism of the acoustic excitation, therefore resolving the discrepancy between prior experimental implications and numerical predictions in aSi. For this, we describe the measurements of the MFP of 100 GHz acoustic excitations. Then, we apply a novel approach to obtain a frequency resolved MFP for frequency 0.1 – 3 THz in aSi using TG. Finally, we discuss the presence and the origin of the weak damping in aSi, which is in contradiction with the prior numerical predictions. The results in this chapter

provide a clear picture for understanding atomic vibrations in glasses quantitatively, a long standing challenge for bulk amorphous materials.

Finally, in chapter 6, we summarize the results of this thesis and discuss an outlook for future works.

Chapter 2

INTRODUCTION TO TRANSIENT GRATING SPECTROSCOPY

In the following discussion, we introduce a thermal characterization tool, transient grating (TG) spectroscopy. The transient grating is based on optical holography and was originally employed in other fields, for example for the study of ultrasonic waves, among others [38]. Concerning the thermal transport, the TG was applied to measure the bulk thermal diffusivity of polyamide thin-film [39]. The improvements in the spatial and temporal resolution further expanded its capability toward MFP spectroscopy [33, 37]. We start from the theoretical background and the principles.

2.1 Fundamentals

Thermal grating formation

Typically in TG, two different laser sources are employed: pulsed laser as a pump and continuous wave laser as a probe, respectively. We start by describing pump induced material response.

Figure 2.1 shows a schematic of the TG experiment. At phase mask, pump diffracts from the sample, and a pair of first order diffracted beams are created. Following Bragg's law of the diffraction, the separation between two beams are given by

$$\sin \theta_1 = \frac{\lambda}{d_{PM}} \quad (2.1)$$

where $2\theta_1$ is the angle between two beams, λ is the optical wavelength, and d_{PM} is the phase mask period.

The first order diffracted pump beams from the phase mask are focused on the sample, which can be expressed as

$$\mathbf{E}_{pu,\pm 1} = \eta_{PM} E_{pu,laser} \exp(i\mathbf{k}_{\pm 1} \cdot \mathbf{r} - i\omega t) \quad (2.2)$$

$$\mathbf{k}_{\pm 1} = \mp k_x \hat{x} + k_z \hat{z} \quad (2.3)$$

$$|\mathbf{k}_{\pm 1}|^2 = k_x^2 + k_z^2 \quad (2.4)$$

where $\mathbf{E}_{pu,\pm 1}$ is the electric field of the pump beams, η_{PM} is the optical diffraction efficiency of the phase mask (typically 0.8 for wavelength ~ 500 nm), \mathbf{k} is the wave

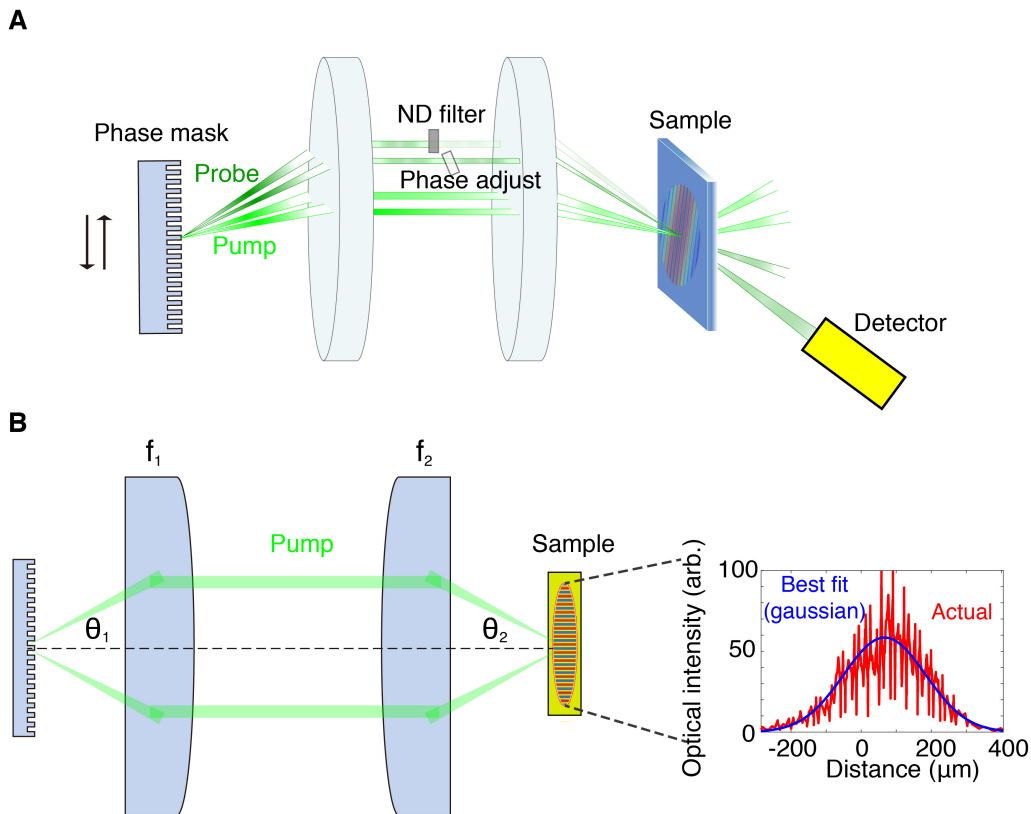


Figure 2.1: Schematic illustration of the TG. (A) Pump and probe beams diffract from the phase mask from which first order diffracted beams are created. The diffracted pump beams pass through telescope lenses and are focused on the sample. Since two beams are coherent, they interfere on the sample. The interference on the sample is impulsively absorbed in the sample and create a spatially periodic thermal gradient. One of the diffracted probe (signal beam) is optically phase adjusted and diffracts from the grating profile on the sample; the other probe (reference beam) is attenuated by ND filter and transmitted from the sample. Finally, first order diffracted signal and the transmitted reference beams are fed into the detector, and used for detecting pump-induced thermal response. (B) Detailed beam path for the pump. As an example, measured optical interference of the diffracted pump beams at phase mask period of $\sim 60 \mu\text{m}$ is shown. Corresponding profile is a Gaussian shape with a slow modulation with a period of $15 \mu\text{m}$.

vector of the light, and ω is the optical frequency. The interference of the pump beams create an optical grating profile with an intensity (I):

$$I_{pu} = |\mathbf{E}_{pu,+1} + \mathbf{E}_{pu,-1}|^2 = 2(\eta_{PM}|E_{pu,laser}|)^2[1 + \cos(2k_x)] \quad (2.5)$$

As an example, the actual intensity of the optical interference at a phase mask period $60 \mu\text{m}$ is given in the inset of Fig. 2.1. The interference pattern was taken

using CCD camera beam profiler (BC106N-VIS, Thorlabs inc.). As in the inset of Fig. 2.1, the profile is a slowly varying Gaussian profile as well as the modulation due to $|E_{pu,laser}|^2$ in Eq. 2.5 [40].

The absorption of the optical interference generates the thermal transient grating on the sample (ΔT)

$$\Delta T = \alpha I_{pu} \propto [1 + \cos(qx)] = \left[1 + \cos\left(\frac{2\pi}{L}x\right) \right] \quad (2.6)$$

where α is the absorption coefficient, $q(= 2k_x)$ is the grating wave vector of the sample, and L is the grating period on the sample defined by $L = 2\pi/q$.

We can relate phase mask period (d_{PM}) to L using the geometry of the telescope shown in Fig. 2.1. Consider the telescope lenses with arbitrary focal lengths being f_1 and f_2 ($f_1 > f_2$). Considering the same numerical aperture of diffracted pump beams entering the lenses, the distance of the pump beam from the optical axis can be expressed as:

$$f_1 \tan \theta_1 = f_2 \tan \theta_2 \quad (2.7)$$

where θ_2 is the laser incidence angle to the sample. Using Eq. 2.1, Eq. 2.6, and Eq. 2.7, we can derive an expression for L

$$L = (\lambda/2) \left[\sin \left(\tan^{-1} \left(\left(\frac{f_1}{f_2} \right) \tan \left(\sin^{-1} \left(\frac{\lambda}{d_{PM}} \right) \right) \right) \right) \right]^{-1} \quad (2.8)$$

In the limit of $\lambda \ll d_{PM}$, or θ_1 , the expression above is simplified to

$$L \approx \frac{f_2}{2f_1} d_{PM} \quad (2.9)$$

The grating period on the sample (L) can be confirmed using several methods. First, the spacing of the burnt grating profile on a metal or dielectric film can be measured. Second, oscillation frequency (f) of the acoustic signal from the opaque sample can be measured. Given the acoustic sound velocity (v), the actual grating period on the sample can be obtained $L = v/f$. Third, CCD imaging of the optical interference can be used; this method is limited by camera pixel resolution, therefore less accurate than the other two methods especially at lower grating periods.

An example of the grating period confirmation on the de-ionized (DI) water is illustrated in Fig. 2.2. The optical wavelength of the pump and probe used is 530

nm and 514 nm, respectively. To increase the absorption, a commercial food dye with a red color was dissolved in DI water. The phase mask period was varied from 4 μm to 43 μm . As shown in Fig. 2.2, the frequency of oscillation on the order of a few hundred MHz was observed, which decreases as the grating period increases. Figure 2.2B shows measured frequency of the oscillation versus the grating period on the sample, which agrees with the calculation from Eq. 2.8.

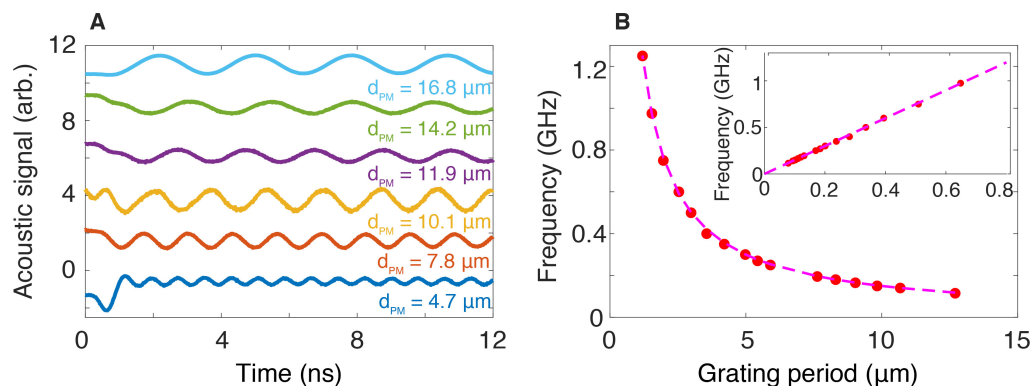


Figure 2.2: Grating period confirmation in TG. The data was taken from the Astrella laser setup built in the Minnich lab at Caltech. (A) Representative signal traces of the Acoustic wave obtained from deionized water with food color at several phase mask periods. Both the sinusoidal curve fitting and the Fourier transform were performed to obtain the frequency of the oscillation which decreases as the phase mask period increases. (B) The oscillation frequency versus the grating period on sample. The frequency was given at (A) whereas the grating period is calculated from Eq. 2.8. For comparison, the expected acoustic frequency of water using $f = v/L$ is shown as a dashed line. Excellent agreement was observed. Inset shows the corresponding dispersion of the water given by the acoustic wave frequency versus the inverse grating period.

2.2 Signal monitoring via heterodyne detection

In the preceding discussion, we described the formation of the transient grating from interference of the pump beams. In TG, corresponding responses can be detected using a phase sensitive detection [41]. This process is known to be the heterodyne detection which allows to amplify the signal magnitude as well as to suppress the unwanted noise components.

More precisely, two phase-controlled probe beams are used for detection, which are generated from the phase mask. A phase adjustable glass window is placed at one of the probe path (signal beam), while neutral density (ND) filter placed at the other probe path (reference beam). Both beams are focused on the sample with Bragg

angle; from the sample, the signal beam diffracts and the reference beam transmits under thin grating condition. The first order diffracted signal beam can be expressed as

$$\mathbf{E}_{sig} = \eta_{PM} E_{pr} \exp(i\mathbf{k}_B \cdot \mathbf{r} - i\omega t + \phi_{sig}) \quad (2.10)$$

$$\mathbf{k}_B = \mp k_B x \hat{x} + k_B z \hat{z} \quad (2.11)$$

where \mathbf{E}_{sig} and $n(T, t)$ is the complex optical transfer function, ϕ_{sig} is the optical phase of the signal, t is ratio of the complex optical transfer function, and the \mathbf{k}_B is the wave vector at the Bragg angle of incidence. The thermal grating induces the spatial modulation of the complex refractive index such that [40]

$$\tilde{n} = n + \Delta\tilde{n} \cos(qs) \quad (2.12)$$

$$\Delta\tilde{n} = \Delta n(T, t) + i\Delta k(T, t) \quad (2.13)$$

where Δn and Δk are changes in the real and imaginary parts of the refractive index, respectively. The spatially modulated refractive index leads to a transfer function under thin transmission grating condition [40, 42]

$$t = t_0 [1 + (\Delta k(T, t) + i\Delta n(T, t))] \cos(qx) \quad (2.14)$$

where t_0 is the intrinsic sample transmission without the thermal grating. Multiplying Eq. 2.14 with Eq. 2.10, we obtain the expression for the first order diffracted signal beam from the sample

$$\mathbf{E}_{sig} = t_0 (\Delta k(T, t) + i\Delta n(T, t)) \eta_{PM} E_{pr} \exp(i\mathbf{k}_{Bs} \cdot \mathbf{r} - i\omega t + i\phi_s) \quad (2.15)$$

$$\mathbf{k}_{Bs} = k_B x \hat{x} + k_B z \hat{z} \quad (2.16)$$

where ϕ_s accounts for the optical phase introduced both by tilting of the glass window and the diffraction from the sample. Similarly, the transmitted reference beam from the sample can be expressed as follows

$$\mathbf{E}_{ref} = t_0 t_r \eta_{PM} E_{pr} \exp(i\mathbf{k}_{Br} \cdot \mathbf{r} - i\omega t + i\phi_r) \quad (2.17)$$

$$\mathbf{k}_{Br} = -k_B x \hat{x} + k_B z \hat{z} \quad (2.18)$$

where t_r is the attenuation factor introduced by ND filter, and ϕ_r is the optical phase introduced by ND filter and the transmission from the sample. Note that the attenuation factor is determined by the optical density (OD) of the ND filter. We examine the intensities of the beams at a fixed temperature. The intensity of the static reference beam is given by

$$\mathbf{I}_{ref} = |t_r|^2 |t_0|^2 |\eta_{PM}|^2 |E_{pr}|^2 \quad (2.19)$$

Similarly, the intensity of the diffracted signal in the absence of the reference beam is given by,

$$\mathbf{I}_{sig}^{non} = |t_0|^2 |\eta_{PM}|^2 |E_{pr}|^2 [\Delta k(t)^2 + \Delta n(t)^2] \quad (2.20)$$

The intensity indicated by Eq. 2.20 is called non-heterodyned signal which contains both real and imaginary parts of the pump induced refractive index changes. Since, impulsive pump excitation relaxes due to the thermal diffusion, the \mathbf{I}_{sig}^{non} eventually approaches zero. As indicated by Eq. 2.17 and Eq. 2.15, the first order diffracted signal beam and the transmitted reference beam are collinear. Corresponding interference can be expressed as the superposition of the electric field given in Eq. 2.17 and Eq. 2.15.

$$\mathbf{I}_{sig} = |t_0|^2 |\eta_{PM}|^2 |E_{pr}|^2 [\Delta n(t)^2 + \Delta k(t)^2 + t_r^2 + 2t_r [\Delta k \cos \phi + \Delta n \sin \phi]] \quad (2.21)$$

where $\phi = \phi_s - \phi_r$ is the phase difference between signal and the reference.

By removing original static reference intensity (homodyne contribution Eq. 2.19, see Ref. [43]) as well as the original signal part in Eq. 2.21, one can obtain the heterodyne part of the superposition

$$\mathbf{I}_{sig}^{hd} = |t_0|^2 |\eta_{PM}|^2 |E_{pr}|^2 2t_r [\Delta k \cos \phi + \Delta n \sin \phi] \quad (2.22)$$

While both the heterodyne signal (Eq. 2.22) and the non-heterodyne signal (Eq. 2.20) contain time-varying index of refraction changes, heterodyne signal can provide pure real and imaginary parts of the refractive index by adjusting the optical phase. For heterodyne signal, if $\phi = \phi_s - \phi_r$ becomes the integer multiples of π ($\pi/2$), one can measure the response directly proportional to $\Delta k(t)$ ($\Delta n(t)$); amplitude grating (phase grating). The phase grating is known to be contributed by temperature grating and thermally induced stress whereas the amplitude grating contains the response

from the temperature grating only [33, 40, 44]. In prior TG experiments, the pure phase grating was generally observed in dye-incorporated opaque sample including water, m-xylene, and polyethylene. The pure amplitude grating signal was observed in crystalline silicon. Another benefit of the heterodyne signal is the presence of the attenuation factor (t_r) in heterodyne signal. The attenuation factor substantially increases the signal-to-noise ratio while not saturating the detector.

2.3 Thermal signal traces and fitting

In the preceding sections, we have discussed formation of the transient grating and its detection using heterodyne scheme. In this section, we examine decaying dynamics of the thermal signal. According to the Fourier's law of heat diffusion, the heat flux can be expressed as

$$\mathbf{J} = -\kappa \nabla T \quad (2.23)$$

Considering the arbitrary heat source (J_{gen}), the energy transfer over a constant volume can be related to the internal energy using the first law of the thermodynamics [22]

$$\int_V [\nabla \cdot (\kappa \nabla T) + J_{gen}] dV = \int_V \rho C \frac{\partial T}{\partial t} dV \quad (2.24)$$

$$\rho C \frac{\partial T}{\partial t} = \nabla \cdot (\kappa \nabla T) + J_{gen} \quad (2.25)$$

where C is the heat capacity, J_{gen} is the rate of the heat generation, and ρ is the density. Since all the experiments presented in this thesis are based on transmission geometry of the TG, we limit our discussion only in x direction. We consider a impulsive spatially periodic thermal gradient as a heat source. Corresponding 1-D heat diffusion can be expressed as

$$\rho C \frac{\partial T}{\partial t} = \kappa \frac{d^2 T}{dx^2} + Q_0 \cos(qx) h(t) \quad (2.26)$$

where Q_0 is the magnitude of the energy given by laser and $h(t)$ is the heat intensity distribution [45]. We solve the problem using a Fourier transform in space and time with a solution given by

$$T = I_0 \exp[i\omega t - ikx] \quad (2.27)$$

$$\rho C \mathcal{F}\left[\frac{\partial T}{\partial t}\right] = \kappa \mathcal{F}\left[\frac{d^2 T}{dx^2}\right] + Q_0 \mathcal{F}[\cos(qx)h(t)] \quad (2.28)$$

Assuming that the temporal width of the laser is sufficiently small compared to the time scale of the diffusion, the heat source term in Eq. 2.28 can be simplified to $\sim Q_0$. Considering the space and time dependent term only, Eq. 2.28 can be simplified to

$$\mathcal{F}[T(t, x)] = \frac{Q_0}{i\rho C + \kappa q^2} \quad (2.29)$$

Using thermal diffusivity defined by $\alpha = \kappa/(\rho C)$, the expression for temporally decaying temperature is given by

$$T(t, x) = \frac{\sqrt{2\pi}Q_0}{\rho C} \exp[-\alpha q^2 t] \propto \Delta T \exp[-t/\tau] \quad (2.30)$$

where ΔT is the transient temperature induced by the thermal grating at $t = 0$, and the $\tau = 1/\alpha q^2$ is the thermal decay time constant. From Eq. 2.30, we see features concerning the thermal grating signal. First, the initial signal magnitude is linearly proportional to the optical energy injected, which is related to the transient temperature of the sample. Second, the signal decays with a time constant τ that depends on both the thermal diffusivity of a material and the grating period.

2.4 TG arrangements

Having demonstrated the fundamental working principles, we now discuss appropriate arrangements and requirements of the TG.

Optical setup

The aforementioned description implies several requirements for TG. First, for probing heat-carrying acoustic vibrations, relevant thermal length scale ($\sim L/2\pi$) should be offered on the order of hundred nanometer, which will be changed depending on the frequency of the vibration. Second, typical one-dimensional thermal decaying dynamics, represented by Eq. 2.30, occurs at a nanosecond to microsecond scale, meaning that corresponding frequency ranges for detection are on the order of sub-GHz. Third, the heterodyne detection scheme requires to adopt a phase sensitive optics. These requirements, albeit stringent, lead to designing the TG as follows.

Figure 2.3 describes the arrangements of the TG setup as a schematic. The optical power is adjusted using the half-wave plate and the polarizing beam splitter. For the impulsive heating process, it is desirable having the same optical polarization for both pump and probe [39], therefore vertical polarized lights for both beam paths were used in this setup. A great advantage of the TG is the employment of the phase mask. This makes the first order diffracted beams coherent, resulting in interference. The resulting period of the interference on the sample position can be variably tuned by a simple translation of the phase mask. The corresponding

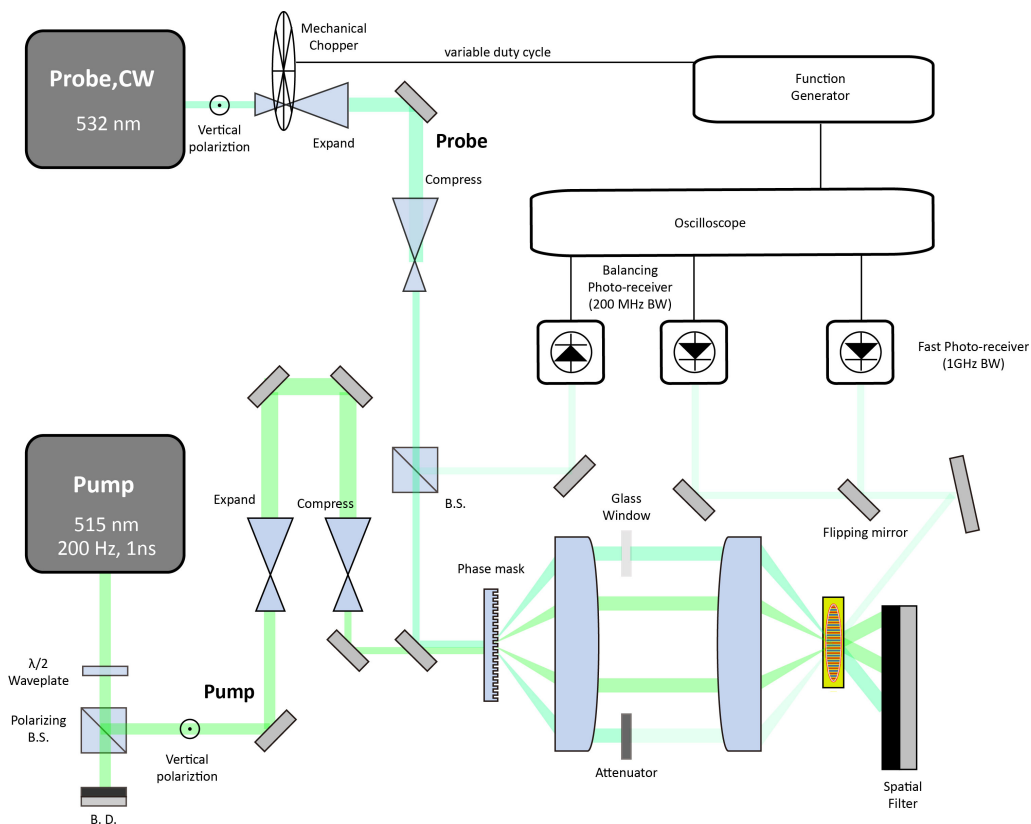


Figure 2.3: Schematic of the typical real-time TG setup. The shown is the schematic of the setup built in the Minnich lab. The setup is identical to what is described in [37]. The pump pulses pass through multiple optics such as the polarizing optics for intensity controller, telescopes for the precise beam controller at the sample position. A CW probe is mechanically chopped to minimize the duty cycle for reducing steady heating of the sample. After the sample, the heterodyne component of the signal is delivered to the oscilloscope via the detector. The temporal resolution can be varied by the choice of the detector depending on the response time. Similarly, spatial length scale for the thermal gradient can be conveniently varied by translating a phase mask.

length scale that can be changed is from > 500 nm nanometer to microns, which are matched with phonon MFPs in many materials.

The second advantage is the employment of the CW laser as a probe and detection via oscilloscope, providing a variable temporal resolution and time window. Typically in conventional pump probe spectroscopy, the time window in which one can monitor the signal is limited by the length of the delay stage. For instance, the maximum time window is order of ≤ 50 ps for ultrafast pump-probe spectroscopy, or on the order of ≤ 13 ns for time-domain thermo-reflectance, a time scale not sufficient for

decaying dynamics corresponding to Eq. 2.30. To overcome this challenge, in TG, an oscilloscope rather than the delay stage is typically used to provide a longer time window than conventional pump probe spectroscopy. In this setting, the temporal resolution is now limited by the rise time of the detector on the order of 1 ns - 5 ns, and further can be reduced to ~ 250 ps by using a fiber-optic detector. Note that the setup presented in Fig. 2.3 was used to perform the measurements in chapters 4 and 5.

Application to crystalline thin-films

In the preceding section, we discussed the optical configurations and associated advantages for probing thermal transport using TG. We now present an application to study the bulk crystalline thin film, a 1 μm -thick crystalline silicon membrane. The silicon membrane was provided by Prof. Clivia Stotomayor Torres' group at ICN2. The membrane was prepared similar to the method described in Ref. [33, 46].

To measure the membrane, we prepared the optical setup as follows. Briefly, a Ti:sapphire laser (wavelength: 800 nm, repetition rate: 1 kHz, pulse-width: 25 fs, Astrella, Coherent inc.) was used as a pump seed laser. The pump was then optical parametric amplified to be converted to 532 nm (power incident on the sample: 5 μJ). A CW laser was chosen as probe laser (wavelength: 514 nm, average power: ~ 5 mW, Genesis MX, Coherent inc.). The CW probe was chopped with $\sim 10\%$ of duty cycle. We varied the grating period from 1.3 μm to 15 μm . The 1 GHz free space photodetector (1 GHz bandwidth, Newfocus 1601, Newport inc.) was used except for $L = 1.3 \mu\text{m}$ at which we used 4 GHz fiber-optic detector (4 GHz bandwidth, Newfocus1591NF, Newport inc.).

Figure 2.4A shows measured signal traces at each heterodyne phase (ϕ). By subtracting the signal at $\phi = -\pi$ from $\phi = \pi$, the resulting thermally induced signals were obtained as shown in Fig. 2.4B. In Fig. 2.4B, we see two different components of the decay. The signal decays with an initial negative magnitude within 1 ns, followed by slower decay with a time constant around 30 ns. It is established that the origin of the faster decay is the ambipolar diffusion of the electron-hole pairs, while the following slower decay is associated with the heat diffusion [33]. Therefore, following Ref. [33], we fit the signal using bi-exponential model from which we determined the thermal decay time constant. The corresponding thermal conductivity was calculated using the calculated heat capacity (quasiharmonic approximation using LDA normconserving pseudopotentials, data provided by Dr. Navaneetha K.

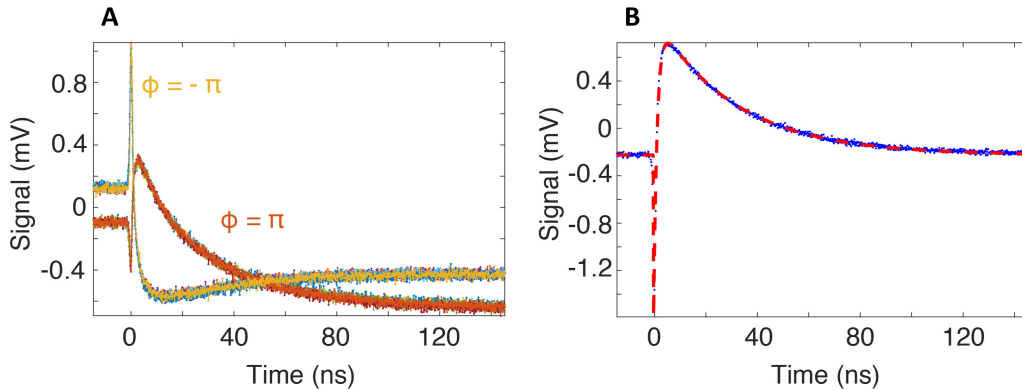


Figure 2.4: Example of the TG for application to crystalline membrane. A representative of TG signal traces for crystalline silicon measured at $L = 8.3 \mu\text{m}$ (A) The signals at each heterodyne phase. (B) Resulting thermal transient grating signal obtained from the subtraction of the signal traces in (A). We see a faster decay with a negative magnitude followed by a slower decay with a positive magnitude. The faster decay is due to the diffusion of the electron and hole pairs, while the slower decay is due to the diffusion of the phonons. Corresponding bi-exponential fitting is indicated as a dashed line.

Ravichandran). The resulting thermal conductivity versus the grating period for the $1 \mu\text{m}$ crystalline silicon membrane is shown in Fig. 2.5A. The measured thermal conductivity is $\sim 100 \text{ Wm}^{-1}\text{K}^{-1}$ above $4 \mu\text{m}$, below which the value decreases.

The corresponding value of the thermal conductivity for a $1 \mu\text{m}$ thick membrane agrees with the literature data given in Fig. 2.5B. The estimated thermal conductivity versus the grating period is presented as a dashed line in Fig. 2.5A. The estimation was performed using $F(\Lambda)$ given in Ref. [35] and the thermal conductivity suppression function [34], and the Fuch-Sondheimer MFP reduction factor in the absence of the specular scattering ($p = 0$) [47]. We see a reasonable agreement between the data and the estimation, but slightly lower than the prediction, which may be due to the thickness slightly lower than $1 \mu\text{m}$.

2.5 Summary

In this chapter, we demonstrated the TG as a tool to study heat conduction in thin films. We have described the theoretical background along with the principles of the TG, including the generation of the grating and corresponding detection. We showed optical setup arrangements that are required for designing.

We have demonstrated an example of its application of TG to measure both bulk thermal conductivity and grating dependent thermal conductivity. We have shown

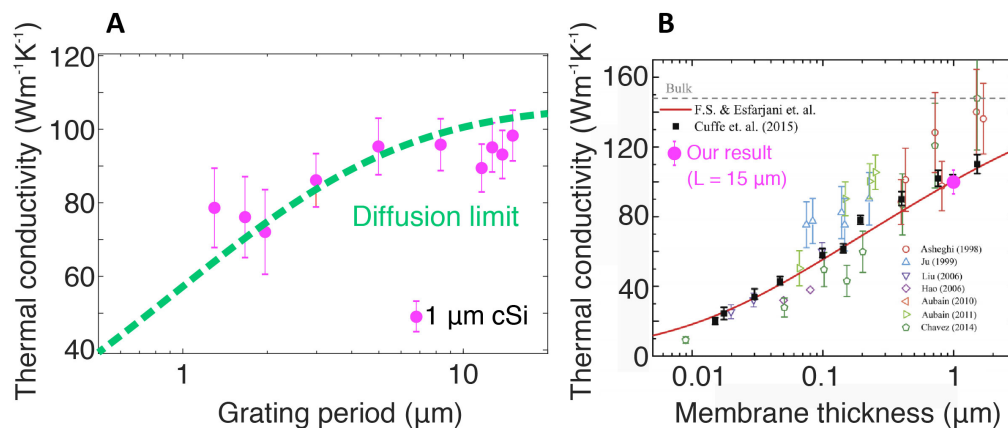


Figure 2.5: (A) Thermal conductivity versus the grating period for $1 \mu\text{m}$ thick silicon membrane (measured: symbol). An estimation using the literature value of the cumulative thermal conductivity versus MFP [35], and phonon suppression function [34] is shown as a dashed line. A reasonable agreement is observed. (B) Literature data of thermal conductivity versus the membrane thickness for crystalline silicon [48]. Our measured thermal conductivity at $L = 15 \mu\text{m}$ is also shown ($\sim 100 \text{Wm}^{-1}\text{K}^{-1}$). Note that this value agrees with prior literature experimental data on the observation of classical size effects and the predictions.

that the bulk value is close to the prior observations.

To conclude this chapter, the TG technique is appropriate for measuring the thermal transport in many materials due to its adaptiveness. In the next chapter, we will present an example of tailored TG to study elastic and thermal properties of a crystalline material simultaneously. We seek to expand its capability of application to semi-crystalline and amorphous materials to study the thermal transport properties in them.

*Chapter 3*IN-PLANE ELASTIC AND THERMAL PROPERTIES OF
MOLYBDENUM DISULFIDE

This chapter has been adapted, in part, from:

Taeyong Kim, Ding Ding, Jong-Hyuck Yim, Young-Dahl Jho, and Austin J. Minnich. Elastic and thermal properties of free-standing molybdenum disulfide membranes measured using ultrafast transient grating spectroscopy. *APL Materials*, 5 (8):086105, 2017. doi: 10.1063/1.4999225. URL <https://doi.org/10.1063/1.4999225>.

T.K. prepared the experimental data, analyzed the results, and participated in the writing of the manuscript.

In this chapter, we present in-plane elastic and thermal measurements by employing TG spectroscopy. We begin by introducing and describing the development of the ultrafast TG experiments. We then demonstrate its capability by applying the TG to characterize the thermal and elastic properties in a bulk crystalline material, MoS₂.

As mentioned earlier, it is important to prepare an experimental probe that has relevant temporal length scale for the transport of the phonons. Concerning a crystal that can support higher speed of sound, corresponding oscillation frequency at a TG wave vector is order of GHz ranges, which is challenging to access using conventional arrangements in TG. Therefore, we develop an ultrafast transient grating (UTG) technique to examine the in-plane bulk thermal and elastic of crystalline solids. This technique is advantageous over the conventional TG in that this time-resolved scheme offers temporal resolution ~ 100 fs, allowing us to simultaneously probe phonon group velocity as well as fast decaying heat diffusion.

3.1 Ultrafast transient grating

The figure 3.1 shows the schematic of the ultrafast time-resolved transient grating spectroscopy. The setup was built at Joint Center for Artificial Photosynthesis (JCAP) building at Caltech. We used a regeneratively amplified Ti:sapphire laser (Libra, Coherent) that generated 100 fs pulses at 10 kHz with an energy of 0.4 mJ. The $1/e^2$ diameter of the laser output is ~ 8 mm. The pulse train, which was

centered at 800 nm, was split into pump and probe beams using a half-wave plate and polarizing beam splitter.

To spectrally separate pump and probe pulses, a two-tint optical filtering scheme was used: an optical filter was placed along the pump path (single-band band pass filter at 786 nm, Semrock Inc.), and along the probe path and before the detector for suppressing undesirable pump scattering into the detector (RazerEdge long pass filter at 808 nm, Semrock Inc.) [49].

The pump beam was mechanically chopped at 2.5 kHz with a chopper wheel and focused onto a translatable optical phase mask to yield two excitation pulses. The excitation pulses were focused onto a spot with a diameter of $550\ \mu\text{m}$; their interference generated a periodic heating profile that resulted in thermoelastic standing LA waves and a spatially periodic thermal gradient. The probe beam was directed to a mechanical delay stage (ACT115DL, Aerotech) with a silver coated retro-reflector. The delay stage was arranged to perform a double-pass reflection, providing approximately 4 m of spatial delay corresponding to around 13 ns in time delay. The probe pulses were then directed to the optical phase mask, yielding signal and reference beams. The signal beam passed through a glass window to provide optical phase adjustment and was focused onto the sample; the reference beam was attenuated by a neutral density filter (ND 3) and focused onto the sample. The diameter of the focused probe beam was $400\ \mu\text{m}$. After transmitting through the sample, the overlap of the transmitted reference and first-order diffracted signal beam were directed to the detector (BPW34, Vishay Inc.). This signal was then balanced by another photodiode measuring a reference beam and the subtracted signal fed into lock-in amplifier (SR 830 of Stanford Research Systems). The relative heterodyned phase difference between the reference beam and the probe beam was controlled by motor controller (DC Stepper Motorized Actuator, Thorlabs).

Setup modification and improvements

Here, we describe our special efforts that were put into this setup. First, the improvement in the setup was made in the power adjustment. As mentioned above, the optical energy from the Libra laser is 0.4 mJ. Such high optical energy can damage the optical elements. In addition, in TG, the optical energy required for obtaining adequate signal magnitude ($\sim 1\ \text{mV}$) is typically less than less than $20\ \mu\text{J}$; we therefore should attenuate the optical energy. One approach is to use the ND filter, and the other approach is to use polarizing optics. The metallic ND filters are widely

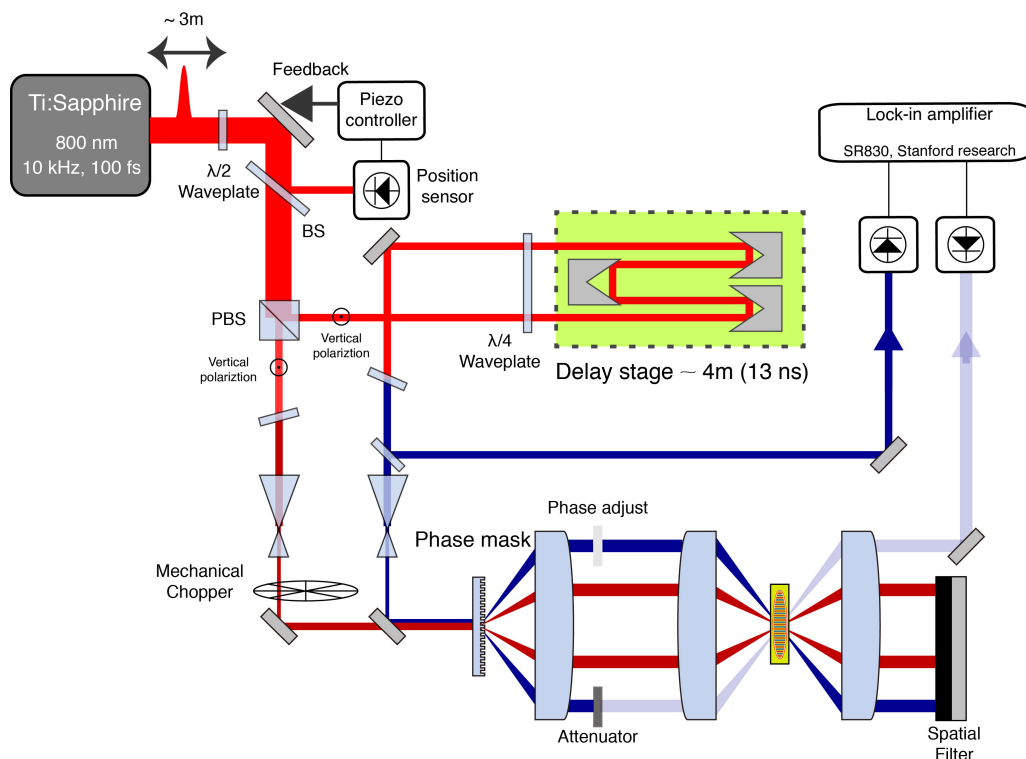


Figure 3.1: Schematic of the ultrafast TG in Joint Center for Artificial Photosynthesis Laboratory at Caltech. The output of the regeneratively amplified Ti:sapphire laser source with a repetition rate of 10 KHz is split into pump and probe using a half-wave plate and polarizing beam splitter. A two-tint optical coloring using optical filters was employed to spectrally separate the pump and probe by around 20 nm in order to suppress pump scattering into the detector. The pump was mechanically chopped at 2.5 KHz and its first order diffracted beams are focused on the phase mask (spot diameter $550 \mu\text{m}$) and interfere on the sample. The interference creates a thermoelastic standing LA waves and a spatially periodic thermal gradient. The probe beam travels an additional $\sim 4 \text{ m}$ corresponding to delay time around 13 ns, and are directed to the sample. The reference beam and the signal beams are separated from phase mask and the relative optical heterodyne phase is controlled using ND filter and glass window. The glass window is tilted using motor controller (DC Stepper Motorized Actuator, Thorlabs). The first order diffracted probe beam and the transmitted reference beams are sent to the fast Si photodiode; the signal is balanced by another photodiode and fed into the lock-in amplifier.

used in laser experiments because optical power can be attenuated using the light reflection without changing laser property such as beam collimation. Originally, the reflective ND filter was used to attenuate the laser beam. Unfortunately, unwanted non-linear phenomena were observed due to the thermal lensing effect. The thermal lensing effect has been reported primarily in continuous-wave laser system [50] or

high power lasers. Briefly, the laser-heating causes the first-order effect (thermal gradient) in addition to the second-order effect (thermally induced mechanical stress) in the medium, eventually changing the refractive index. The first order effect is known to be the primary source of the focusing, while the second order effect is attributed to be the source of the aberration. Figure. 3.2 shows several profiles of the laser beam, propagating after the ND filter. First, We find that the ND filter changes the undesirable collimation property; the filter focused the beam with a focal length of around 5 m. We estimated the focal length from thermal lensing effect in our laser system using

$$f^{-1} = \frac{dn/dT}{2\kappa r} P \quad (3.1)$$

where the dn/dT is the thermo-optic coefficient, κ is the thermal conductivity, r is the beam radius, P is the laser power. Using the property of the N-BK7 glass ($dn/dT = 7.1 \times 10^{-6} \text{ K}^{-1}$, $\kappa = 1.1 \text{ Wm}^{-1} \text{ K}^{-1}$), and the $r = 4.4 \text{ mm}$ and 3.8 W , we obtained the focal length of thermal lens 5 m , which agrees with our observation. Not only the beam focusing, the astigmatism was observed.; initially the beam was elongated to x-direction, eventually to y-direction due to different focal point as in Fig. 3.2A-E. The reason for this is that the focal length of the ND filter caused by the second order effect is different depending on ray bundles in different planes; the meridional rays (along the y-direction) focuses earlier than that along the sagittal (along the x-direction) plane as indicated in Fig. 3.2G. We solved this problem by using half-wave plate and polarizing beam splitter. Furthermore, the pump and probe power was fine-tuned using slight rotation of the two-tint optical filters mentioned in previous section.

Second, we use an open loop beam stabilization system to improve the beam stability. Typically, lasers have spatial fluctuation which are examined as an angular value, or laser pointing stability. The pointing stability is order of micro to milliradian, which can influence the pointing accuracy at a longer distance from the laser. As indicated in Fig. 3.3, is around 3 m ; the measured laser position drift near the half wave plate was around $400 - 800 \mu\text{m}$ with a frequency of a few Hz. We improved the beam stability using open-loop piezo controller system (position sensor: PDP90A, Thorlabs inc.; piezo driver: KPZ 101, Thorlabs inc.; 2 channel piezo adjuster: Polaris-K1PZ2, Thorlabs inc.).

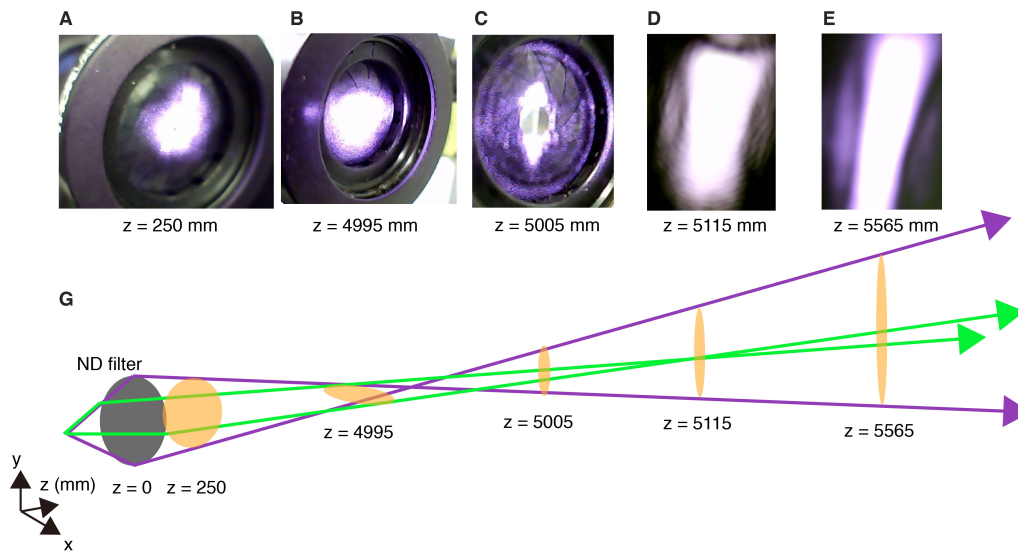


Figure 3.2: Astigmatism caused by the thermal lensing effect. (A - E) The laser beam profiles at several locations after the ND filters are shown. The images were taken by CCD camera. Due to the thermal lensing effect laser, the ND filter focuses the beam with a focal point ~ 5 m. Also, due to the astigmatism, the beam is initially elongated to horizontal direction near $z=4995$ mm after which is elongated to the vertical position. Note that the Fig. 3.2A is the profile at 2 inch iris, Fig. 3.2B,C the profiles at 1 inch iris, and the Fig. 3.2C,D are the profiles at CCD aperture without lens. (F) A schematic describing the thermal lensing effect. Due to the secondary effect of the thermal lensing, the different amount of the refractive index changes are induced depending on the optical axis, therefore making uneven projection of the light on xy plane.

Lens configuration to control the beam size

Not only adjusting the optical energy as discussed in Sec.3.1, but also controlling the beam size are significantly important. Unnecessarily high optical energy in unit area (energy density) would make corresponding thermal response significantly deviate from the operating temperature, or eventually damage the sample. On the other hand, a certain amount of the energy density should be provided in order to obtain adequate signal magnitude without a self-heating of the sample. As shown in Fig. 3.1, we have used beam compressor to make the beam diameter on the sample $550 \mu\text{m}$ ($400 \mu\text{m}$) for pump (probe). Since we use the TG telescope lenses with $f_1 = 150$ mm, $f_2 = 75$ mm, the spot diameter at the phase mask position corresponds to $1100 \mu\text{m}$ ($800 \mu\text{m}$) for pump (probe). In our designing of the beam compressor, we considered the following requirements. First, Galilean telescope rather than the

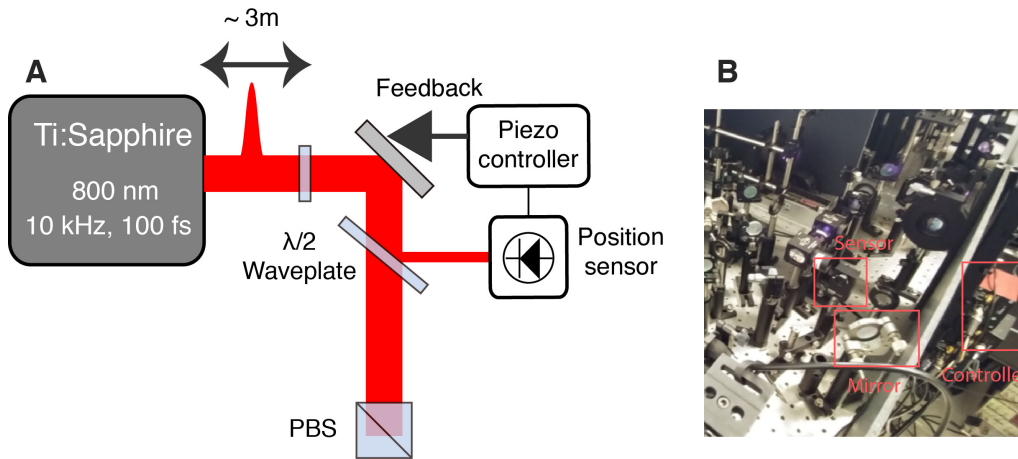


Figure 3.3: (A) Schematic illustration of the open-loop beam stabilization system. The beam stability was improved using beam position sensor, piezoelectric controller, and the piezoelectric mirror. (B) Actual picture of the beam stabilization system. The corresponding components are labeled.

Newtonian telescope was considered to avoid non-linear optical effect at the focal point past the first lens. Second, addition of third lens with a larger depth of focus was considered. According to Gaussian beam optics, the larger depth of focus provides longer Rayleigh length, thus corresponding beam sizes are less likely to diverge at longer distance. Also, the loose-focusing by the third lens significantly reduces the risk of the non-linear optical effect compared to the tight-focusing. The 3.4 shows our our calculated Gaussian beam propagation. The calculation was performed using Matlab, considering lens maker's formula and the Gaussian beam optics. Calculated beam diameter at phase mask position is around $\sim 1100 \mu\text{m}$, ~ 800 , for pump and probe, respectively. Finally, actual beam size at sample position was characterized by knife-edge measurement as shown in Fig. 3.5. The knife-edge measurements confirm $1/e^2$ diameter to be $\sim 550 \mu\text{m}$, $\sim 400 \mu\text{m}$ for pump, and probe, respectively.

Grating period calibration using TG

Despite a special care that may be taken, the actual projected grating on the sample can be slightly off from the Eq. 2.8. This can be caused by the fact that the lens have finite thickness, thus the back focal length and the quoted focal length is different. Another factor is the difference between the lens thickness at the center and at the edge; the beam overlap position can be different from the nominal focal point, causing actually projected grating spacing on the sample deviate from Eq. 2.8.

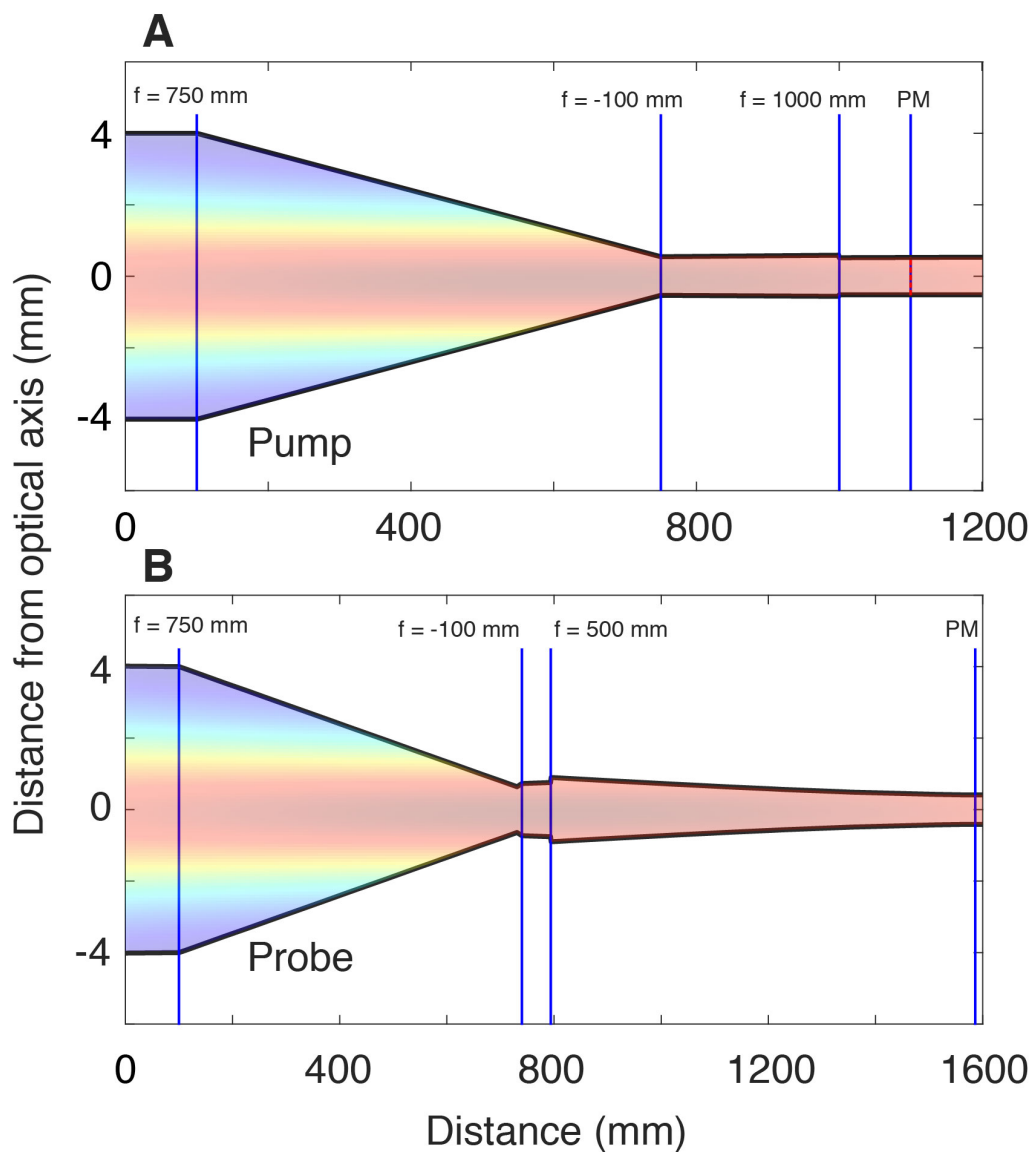


Figure 3.4: Calculated Gaussian beam profile of (A) pump (B) probe. The blue solid lines indicate the location of the optics in which f is the focal length of the lenses, and PM is the phase mask location. For pump, the phase mask was designed to be at the beam waist position, indicated by red dashed line in (A).

Therefore, the grating period was calibrated by verifying the acoustic velocity of sound waves in water. Since the water is transparent, we prepare a green dye (weight ≤ 0.4 mg, Epolight 2735, Epolin inc.) The dye was dissolved into ~ 100 mL of DI water. To increase the optical absorption, the solution was diluted by 24 times. Figure 3.6A shows the surface acoustic waves from water at several phase mask period. The optical power that was used is 24 mW (30 mW) for pump (probe). The signal was obtained by ~ 20 averages. The frequency of the oscillation was

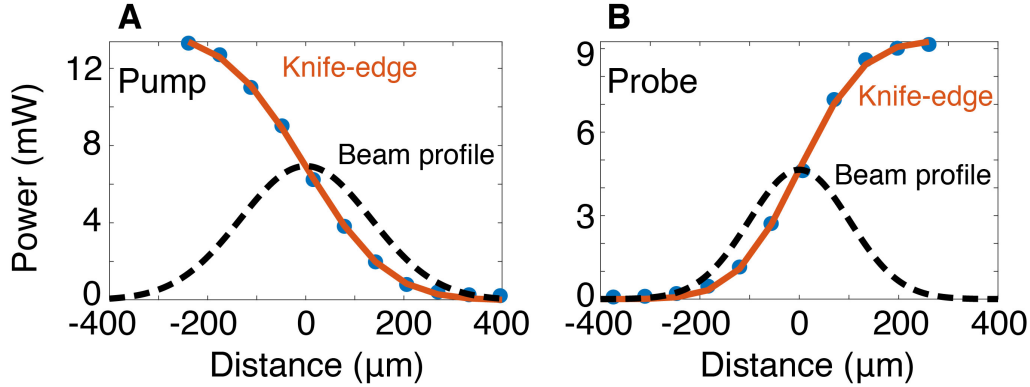


Figure 3.5: Beam size characterization at sample position for (A) pump (B) probe. Symbols represent our measured values. The solid line is corresponding erfc fitting, from which we reconstruct beam profiles shown as dashed lines. Corresponding $1/e^2$ diameter is $\sim 550 \mu\text{m}$, $\sim 400 \mu\text{m}$ for pump, and probe, respectively.

obtained by performing the Fourier transform; the frequency was further confirmed by sinusoidal curve fitting. The resulting acoustic frequency versus grating period at sample position is shown in Fig. 3.6B. Given the oscillation frequency (f), the dashed line indicates the expected grating period using $f = v_w/L$ where v_w is sound velocity in water ($\sim 1500 \text{ m s}^{-1}$ [51]). Compared to the expected grating period using 2.8 (calculation in Fig. 3.6A), the actual grating period (calibration in Fig. 3.6B) was observed to be bigger by factor of 30% at all grating period. This is mainly caused by combination effect of the non-idealities in the phase mask and the optics that were used. The quoted phase mask period may be different from the actual period. Also, the lens parameter of the achromatic doublet lens as a TG telescope lenses (AC508-150-B and AC508-075-B, Thorlabs Inc.) could be different from quoted values due to the thickness of the lens (order of 15 mm), yielding additional uncertainties.

3.2 Material: Molybdenum disulfide

Background

We thus far discussed the designing of the thermal characterization system. In this section, we discuss the prior knowledges of the thermal transport in a crystalline material, MoS_2 .

Transition-metal dichalcogenides (TMDCs) are of considerable interest due to their unique layer-thickness-dependent electronic properties and robust thermal stability. [52–56] In particular, molybdenum disulfide (MoS_2), a member of the TMDC fam-

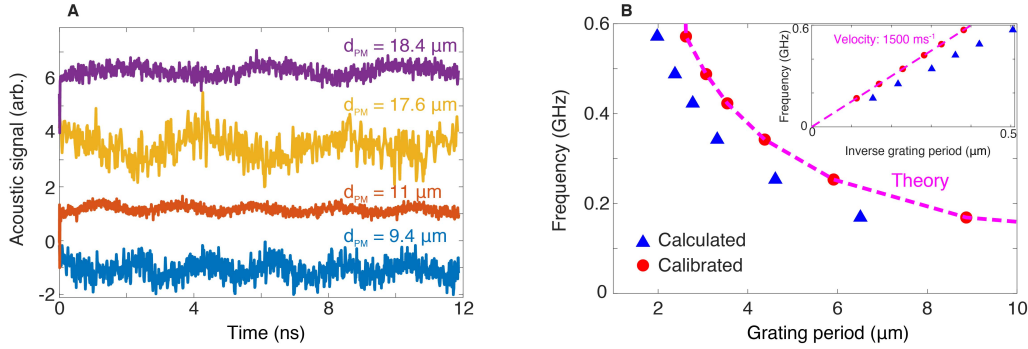


Figure 3.6: Grating period calibration of the ultrafast TG setup. (A) Normalized Acoustic signal obtained from deionized water with dye at several phase mask period. We obtain the frequency of the oscillation by performing both the Fourier transform and sinusoidal curve fitting. (B) The oscillation frequency versus the grating period. The frequency was obtained from (A). The calculated grating period using Eq. 2.8 is represented by blue triangles. The grating period was calibrated (red circles) using sound velocity of DI water ($\sim 1500 \text{ ms}^{-1}$, dashed line). The difference between the calculation and the actual grating period is observed to be 30% due to non-ideality in the optics mentioned in the text. Inset shows the frequency versus the inverse grating period, indicating the acoustic dispersion of the water.

ily, has been extensively investigated due to its potential applications in electronics, photovoltaics, and thermoelectrics. [57–60] In addition to its intriguing electronic properties such as high electron mobility (up to $200 \text{ cm}^2 \text{ V}^{-1} \text{ s}^{-1}$) and indirect-to-direct transition of bandgap with reduced dimensionality [57, 60], MoS_2 has further revealed promising thermoelectric features such as high Seebeck coefficient [61].

Thermal transport in MoS_2 is therefore of intense interest. However, theoretical and experimental studies report a broad range of in-plane thermal conductivity values of MoS_2 . For example, calculations of the in-plane thermal conductivity κ of monolayer MoS_2 vary from ~ 20 to $155 \text{ Wm}^{-1} \text{ K}^{-1}$. [61–69] Various experimental techniques, including Raman spectroscopy, thermal bridge, and time-resolved magneto-optical Kerr effect (TR-MOKE), have been applied to measure the κ of monolayer, few layer, and bulk MoS_2 . The reported values vary widely; from $30.5 - 101 \text{ Wm}^{-1} \text{ K}^{-1}$ for monolayers [70–72], $52 - 102 \text{ Wm}^{-1} \text{ K}^{-1}$ for few layers [70, 73, 74], and $85 - 110 \text{ Wm}^{-1} \text{ K}^{-1}$ for bulk [75].

At the same time, the elastic and acoustic properties of MoS_2 have also been studied, motivated by applications such as flexible electronics. [76–80] In particular, the cross-plane longitudinal sound velocity of MoS_2 has recently been characterized by a transient reflection method. [81] However, although *ab-initio* calculations of

in-plane sound velocity have been reported, to the best of our knowledge the value has not been experimentally confirmed[68, 77]. From the next section, we present our results on the bulk characterization of the MoS₂.

Sample preparation and characterization

All the measurements presented in this chapter were performed on free-standing membrane. The samples were made by our collaborator, Jho research group at Gwangju Institute of Science and Technology (GIST) in South Korea. We prepared suspended MoS₂ membranes by mechanical exfoliation of bulk crystal MoS₂ (2D Semiconductor Inc.). Silicon-on-insulator (SOI) wafers were wet-etched to create rectangular apertures of dimension about 1 - 2 mm at the device side of the wafer. Both SOI wafers and bulk MoS₂ were separately cleaned in an ultrasonic bath of acetone for 5 minutes, then in an ultrasonic bath of methanol for 5 minutes and finally in an ultrasonic bath of deionized (DI) water for 5 minutes. Then, both wafers and bulk MoS₂ were left in a nitrogen gas flow and annealed at 110 °C during 3 minutes to dry the samples. Multilayer MoS₂ flakes were then cleaved from the bulk MoS₂ by repeatedly exfoliating with scotch tape. To fix the MoS₂ flake to the SOI wafer, UV curable epoxy was applied on each corner of the rectangular apertures. The flakes were then placed over the aperture in the substrate and were left under UV illumination for 1 minute to cure the epoxy.

The membranes were characterized using optical microscopy, and energy dispersive x-ray spectroscopy (EDXS) and transmission electron microscope (TEM). Figure 3.8A shows a confocal microscope image of a sample prepared with this method. The image shows that the membrane is intact with some wrinkles over the clear aperture area. The thickness of the membrane was determined by measuring the transmitted optical power through the membrane. For an incident power of 3 mW at 800 nm, 765 μ W was transmitted. Using the Beer-Lambert law and the known dielectric function of MoS₂ [82–84], we estimate the thickness as 5 μ m. The elemental composition along with their spatial distributions were characterized by the Energy dispersive x-ray spectroscopy (EDXS) elemental mapping as in Fig. 3.8B. Spatially uniform distribution of the Molybdenum and the sulfide was observed. We also used high resolution TEM to verify the single-crystalline nature of the sample along with selected area electron diffraction of [001] zone axis to verify the lattice constants, as indicated in Fig. 3.8C. We obtained the magnitude of reciprocal lattice vector as 3.7 nm⁻¹, which agrees well with the hexagonal symmetry with lattice spacing of 0.27 nm along (100) plane as in Fig. 3.8B [85, 86].

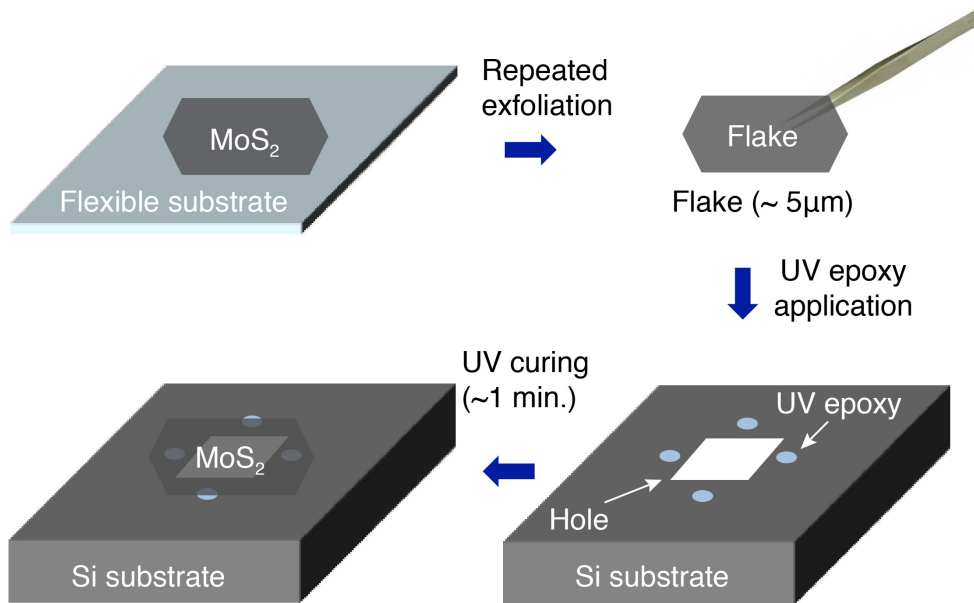


Figure 3.7: Illustration of the preparation of the thin MoS₂ membranes. First, silicon-on-insulator wafers were wet-etched to create rectangular apertures of dimension 1 - 2 mm. Multi-layer MoS₂ flakes were cleaved from the bulk single crystal by repeated mechanical exfoliation using scotch tape. Then UV curable epoxy was applied near the rectangular apertures and the MoS₂ was fixed on top. Finally, the device was left under UV illumination to cure the epoxy. Photo credit: Jho group at GIST

3.3 TG experiments on MoS₂

With the MoS₂ prepared, we performed the TG measurement to obtain in-plane elastic and thermal properties. We conducted measurements with transient grating periods (L) varying from 1.89 μm to 7.15 μm at the sample surface. Following the procedures described in preceding sections, experimental data at distinct phase differences between probe and signal beams $\phi_H = 0$ and $\phi_H = \pi$ are subtracted to isolate the thermally induced heterodyned signal. The pump and probe beam powers were set to 15 mW and 6 mW at the sample, respectively. The corresponding steady-state and transient temperature rises on the sample are around 6 K and 0.6 K, respectively.

Figure 3.9 shows two representative heterodyned signals at different transient grating periods. For each measurement, the signals at $\phi_H = 0$ and $\phi_H = \pi$ are clearly superimposable by flipping the sign of one measurement, as expected. The signals at $\phi_H = 0$ and $\phi_H = \pi$ were then subtracted to yield the final signal. As in Figs. 3.9

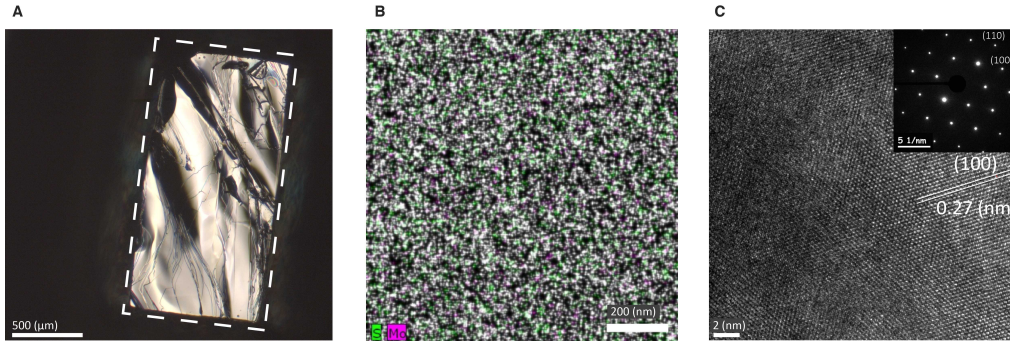


Figure 3.8: (A) Confocal optical microscope images of a MoS_2 membrane suspended over a rectangular hole in an SOI wafer. The dimensions of the free-standing area are about $1 \times 2 \text{ mm}^2$. The dashed line highlights the area where the membrane is suspended. (B) Energy dispersive x-ray spectroscopy (EDXS) elemental mapping of the MoS_2 membrane. The purple and the green indicate the Molybdenum (Mo) and the Sulfide (S), respectively. The EDXS mapping indicates the uniform distribution of M and S in the sample. (C) High resolution transmission electron microscopy (HRTEM) image of MoS_2 indicating single-crystalline structure and revealing the hexagonal lattice. The inset of (C) displays the corresponding selected-area electron diffraction (SAED) pattern along the $[001]$ zone axis. The lattice spacing was identified to be 0.27 nm which is well-matched with the reciprocal lattice distance 3.7 nm^{-1} obtained from SAED.

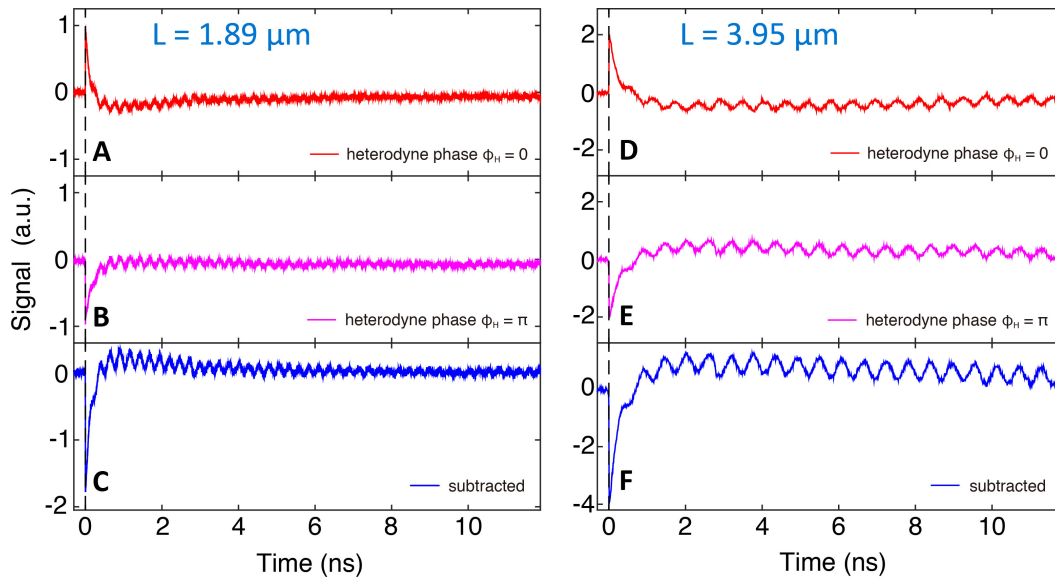


Figure 3.9: Signals measured at grating period of $1.89 \mu\text{m}$ (A, B, C), and $3.95 \mu\text{m}$ (D, E, F). At each grating period, the signals with optical heterodyne phase of $\phi_H = 0$ (A, D) and $\phi_H = \pi$ (B, E) are subtracted to isolate thermally induced signal (C, F).

C and F, we observe an initial rise at 0 ns that quickly relaxes away within 2 ns followed by another slower decay with the opposite amplitude sign. We attribute the first relaxation to ambipolar diffusion of photo-generated electrons and holes and the second decay to the thermal and acoustic response of the sample. The thermal decay becomes slower as the grating period increases, as expected. Considering the acoustic response, we added additional decay term to fit these experimental data using the formula:

$$f(t) = Ae^{-\frac{t}{\tau_T}} + Be^{-\frac{t}{\tau_S}} \cos(2\pi\nu t + \phi) \quad (3.2)$$

where the first (second) term represents the thermal (acoustic) signal with amplitude A (B), τ_T and τ_S are the decay time constants for the thermal and acoustic signals, ν is the frequency of the oscillations, and ϕ is the phase of the oscillation [87]. The frequency of the oscillations ν was first extracted using a Fourier transform (inset of Figs. 3.10A and B and substituted into Eq. 3.2. The fitting is performed after the electronic relaxation ends, corresponding to a thermalization time of around 2 ns but which increases with the grating period [87]. We obtain the other fitting parameters using least square fitting with Levenberg-Marquardt algorithm.

The results of the fitting for two grating periods are shown in Figs. 3.10A and B. We

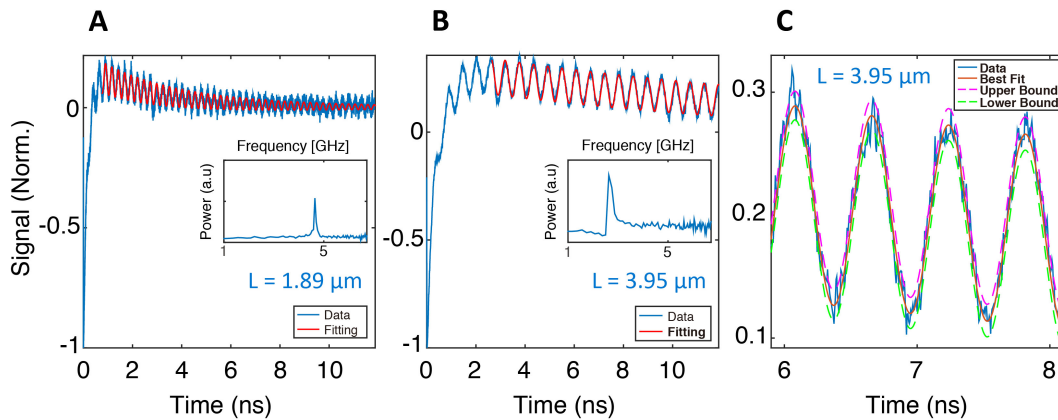


Figure 3.10: Signal obtained by the subtraction of heterodyne phase at $\phi_H = 0$ and $\phi_H = \pi$ versus delay time and the model fit at transient grating period $L =$ (A) $1.89 \mu\text{m}$ and (B) $3.95 \mu\text{m}$. Inset: fast Fourier transform of the data showing acoustic oscillation at each grating period. (C) Uncertainty in fitting curve with respect to the variation of thermal decay rate from B. Purple (green) line describes lower (upper) bound used to determine the uncertainties. The uncertainty is identified to be on the order of $\pm 15\%$.

observe good agreement between the model and the data. Figure 3.10C visualizes the sensitivity of the solutions of fitted curves to the fitted thermal decay rate. We obtain error bounds on the thermal decay rate by determining by what percentage it can change while still overlapping the data. We find that the noise in the experimental measurements yields fitting uncertainties on the order of 15%.

Elastic property of MoS₂

The measured frequency of oscillation can be related to the elastic properties of the MoS₂. We examine the measured acoustic frequency versus grating period, as shown in Fig. 3.11A. The acoustic frequency exhibits a linear trend with inverse grating period, as expected. A linear fit of these data yields an in-plane sound velocity of $7000 \pm 40 \text{ m s}^{-1}$ and corresponding elastic constant of 248 GPa. The measured elastic constant agrees well with prior theoretical and experimental reports which range from 211 - 240 GPa [80]. Since the membrane is suspended, the corresponding sound velocity is not expected to approach the speed of Rayleigh mode of the substrate as is the case for a supported membrane. In a free-standing medium, it has been already established that this Lamb wave mode mainly involves intrinsic longitudinal displacements [88]. We note that the Lamb mode originates from thermally induced generation of coherent longitudinal acoustic phonons [33, 44, 88]. Our measurement is reasonably close to prior ab-initio calculations of an in-plane longitudinal acoustic sound velocity of 6500 - 6700 m s^{-1} [68, 77, 89]. To illustrate this, the literature data of the ab-initio calculation of the in-plane phonon dispersion in Ref. [68] is given in Fig. 3.11B. As shown in Fig. 3.11C, the calculated dispersion along $\Gamma - K$ in the Brillouin zone excellently agrees with our obtained data. Figure 3.11D shows the calculated dispersion in Ref. [89] and corresponding INs measurements in which we can see quantitative difference compared to our measurements. The INS can map out the Brillouin zone over the higher frequency range. However, since the scattering intensity substantially decrease at low frequencies [90], it is challenging to obtain the properties of sub-THz vibration such as phonon group velocity near Γ Brillouin zone.

Thermal property of MoS₂

We now examine the thermal properties. Figure 3.12A shows the thermal decay rate versus the square of wave vector. As shown in Eq. 2.30, assuming one-dimensional

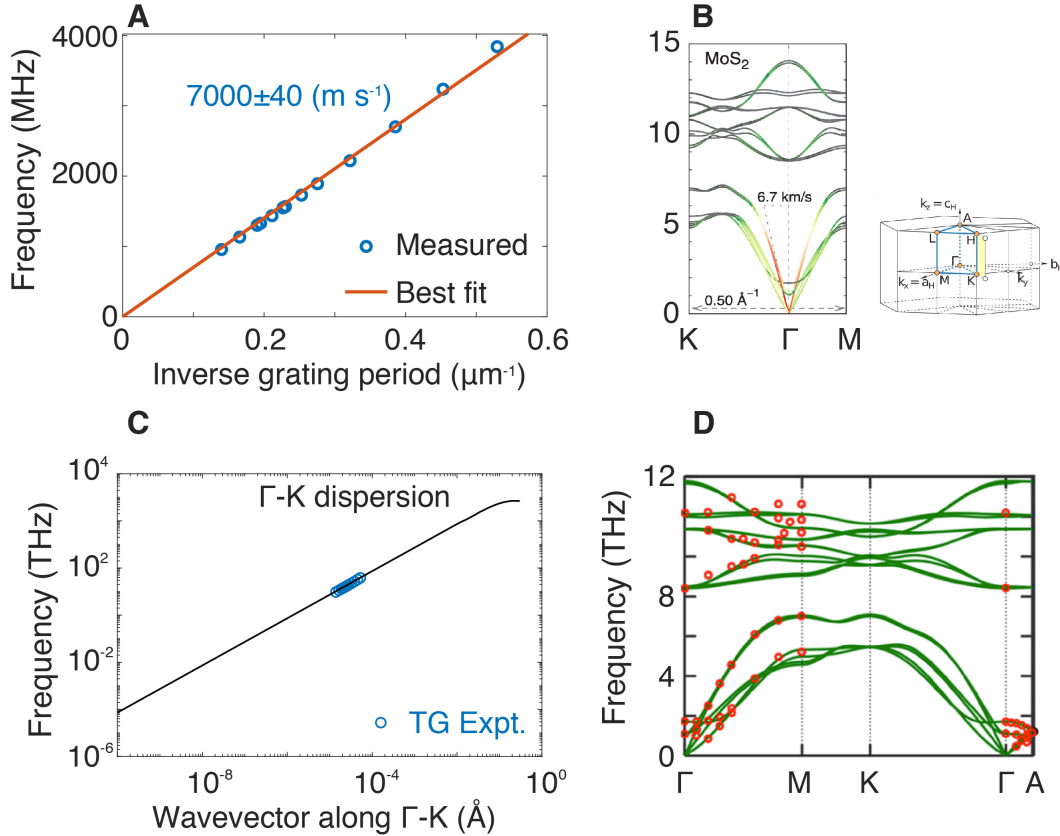


Figure 3.11: (A) Measured acoustic frequency versus inverse grating period. The sound velocity is calculated to be $7000 \pm 40 \text{ m s}^{-1}$, and the corresponding elastic constant is 248 GPa. (B) Literature data of ab-initio calculation of the in-plane phonon dispersion in Ref. [68]. The direction of the wave vector is illustrated as an inset. (C) Calculated phonon dispersion along $\Gamma - K$ in the Brillouin zone in Ref. [68] (black dashed line) and our measured acoustic frequency (symbols). a good agreement is observed. (D) Prior experimental observation of the phonon dispersion in MoS₂ using INS in Ref. [90] (symbols) along with ab-initio calculation in Ref. [89]. The INS successfully map out the dispersion above 1 THz. However, scattering intensity decrease at low frequencies limits to study the dispersion at low frequencies using INS, therefore prevent from deducing the sound velocity as discussed in Ref. [90].

heat diffusion, this trend should be linear following the relation:

$$\frac{1}{\tau} = \alpha \left(\frac{2\pi}{L} \right)^2 = \alpha q^2 \quad (3.3)$$

where τ is the average thermal decay time, α is the in-plane thermal diffusivity, and L is the transient grating period. This is a reasonable assumption since the optical penetration depth of MoS₂ at 800 nm ($12.5 \mu\text{m}$) is longer than the thickness of the sample ($5 \mu\text{m}$) [33][82].

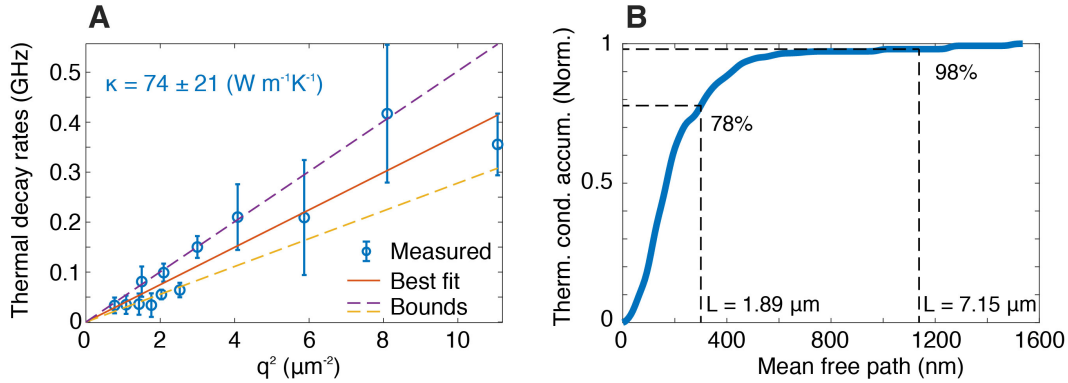


Figure 3.12: (A) Thermal decay rate, or inverse thermal decay time constant, versus wave vector squared. The slope of dashed line yields the thermal diffusivity value from a linear least square fit. Purple (yellow) dashed line denotes the upper (lower) bound of thermal diffusivity. The value of measured thermal conductivity is $74 \pm 21 \text{ Wm}^{-1}\text{K}^{-1}$. (B) Calculation of ab-initio thermal conductivity accumulation versus phonon mean free path of MoS_2 . The phonon mean free path of MoS_2 is spanning from a few nm to $\sim 2 \mu\text{m}$. The black dashed lines indicate thermal length scale corresponding to the minimum and the maximum grating period, respectively. The thermal length scale can be approximated as $L/2\pi$. The relevant thermal length scale is $\sim 0.3 - 1.1 \mu\text{m}$ for our measurements which corresponds to $\sim 78 - 98\%$ of the accumulated thermal conductivity.

In Fig. 3.12A, we show a linear least square fit from which we obtain the thermal diffusivity. Using a heat capacity from Ref. [91], we calculate an in-plane thermal conductivity value of $74 \pm 21 \text{ Wm}^{-1}\text{K}^{-1}$. Our experimental result of thermal conductivity value is slightly lower than recent experimental measurement in Liu et al. [75]; which obtained a value of $85 \pm 6 \text{ Wm}^{-1}\text{K}^{-1}$ using TR-MOKE. The discrepancy may be due to the differences in sample quality; TG probes a larger thermal length scale than does TR-MOKE and thus is sensitive to defects. Additionally, defects may have been introduced in our sample preparation procedure. Nevertheless, our value is in reasonable agreement with this prior report [75]. We also tentatively conclude that phonon mean free paths are smaller than the grating periods considered here as the linear trend observed in Fig. 3.12A is characteristic of phonon diffusion [66, 75].

Our tentative conclusion can be examined by ab-initio calculation of the bulk thermal transport in MoS_2 . The Figure 3.12B shows ab-initio predicted thermal conductivity versus the phonon mean free path in MoS_2 . Briefly, the calculation was performed using interatomic force constants from density functional theory as well as solving the Boltzmann transport equation. The detailed description of the method can be found in Ref. [92]. As shown in Fig. 3.12B, we see that the the mean free path (MFP)

are spanning from a few nm scale to $\sim 2 \mu\text{m}$ scale. Based on the calculation, we can quantitatively estimate the expected accumulated thermal conductivity. Roughly, we estimate the relevant thermal length scale that are comparable to MFP is $\sim L/2\pi$, which corresponds to the MFP $\sim 0.3 - 1.1 \mu\text{m}$. From the calculation of the thermal conductivity accumulation, we find that our value of measured thermal conductivity is 98% at $L = 7.15 \mu\text{m}$, which should decrease to 78 % at $L = 1.89 \mu\text{m}$. However, as mentioned above, the diffuse boundary scattering of the phonons with MFP can suppress the their contribution to the thermal conductivity, thus reducing their total contribution of the thermal conductivity. Our discussion should be re-examined with measurements of smaller uncertainty than those presented here. Nevertheless, our experimental observations are well supported by some of previous theoretical predictions on the thermal conductivity of bulk MoS_2 ($83 \text{ Wm}^{-1}\text{K}^{-1}$) using first-principles calculations [68].

Finally, we note that the error bounds on the thermal conductivity obtained here, on the order of $\pm 15\%$, are larger than typically obtained from TG. We attribute this uncertainty to several factors. First, the laser employed for this work exhibited substantial intensity noise that affected the signal to noise ratio despite the use of balanced detection. Second, wrinkles in the sample may have scattered light and prevented it from reaching the detector. Third, the finite length of delay stage means that data can only be collected to time delays of 13 ns, leading to reduced sensitivity to heat diffusion in the observed signal, particularly for longer grating periods. These effects can be mitigated in the future by improving sample preparation procedures or using chemical vapor deposition for sample fabrication, using a more stable laser source, and performing the real-time TG experiment that employs a continuous-wave (CW) probe and a fast oscilloscope rather than a lock-in amplifier. These improvements will be the subject of future work and will lead to substantially reduced uncertainty.

3.4 Summary

To conclude this chapter, we introduced a tailored TG to study the elastic and thermal properties of the crystalline TMDC thin films. Before this work, the TG application was limited mostly to characterize the thermal transport in crystalline silicon, which we expanded the range of the scope.

Concerning the modification, we have built time-resolved TG to provide a temporal resolution $\sim 100 \text{ fs}$ to simultaneously measure phonon group velocities and the in-

plane thermal conductivity. Careful designing of the optics was discussed including the choice of the polarizing optics as a optical energy controller, piezo-controlled beam stabilizer, and the design of the telescope for beam size controller.

We have applied the TG to MoS₂ to study the elastic and thermal properties in it. More precisely, we obtain a in-plane v_{LA} of $7000 \pm 40 \text{ m s}^{-1}$ and a corresponding c_{11} elastic constant of 248 GPa, which was not experimentally reported until our discovery. We have reported measured in-plane thermal conductivity of $74 \pm 21 \text{ Wm}^{-1}\text{K}^{-1}$. Finally, our thermal conductivity results and associated microscopic heat carrying properties were examined by comparing with more recent ab-initio calculation and experiments.

We expect that these findings provide insight into in-plane thermal and elastic transport in MoS₂ and set the stage for further studies of other crystalline thin films such as TMDCs using TG. In the next chapter, we further expand the range of TG applications to semi-crystalline materials.

*Chapter 4***HEAT-CARRYING PHONONS WITH MICRON-SCALE MEAN FREE PATHS IN HIGHLY ORIENTED POLYETHYLENE**

This chapter has been adapted, in part, from:

Taeyong Kim, Andrew B. Robbins, Stavros X. Drakopoulos, Ignacio Martin-Fabiani, Sara Ronca, and Austin J. Minnich. Heat-carrying phonons with micron-scale mean free paths in highly oriented polyethylene (in preparation).

T.K. participated in the conception of the project, prepared the experimental data, analyzed the results, and participated in the writing of the manuscript, 2020.

Stavros X. Drakopoulos, Georgios C. Psarras, Aurora Nogales, Tiberio A. Ezquerro, Taeyong Kim, Andrew B Robbins, Austin J. Minnich, Georgia C. Manika, Gianfranco Claudio, Ignacio Martin-Fabiani, and Sara Ronca. Gold/ultra high molecular weight polyethylene nanocomposites for electrical energy storage: Enhanced recovery efficiency and thermal conductivity upon uniaxial deformation (in review).

T.K. prepared the thermal characterization data, analyzed the thermal characterization results, and participated in the writing of the manuscript, 2020.

In the preceding chapter, we discussed TG's ability to measure bulk thermal properties of the lattice, beyond conventional applications. As earlier mentioned, there were a few reports concerning the measurements of the bulk thermal properties of polymers. In this chapter, we apply the TG spectroscopy to study microscopic heat-carrying properties in highly oriented semi-crystalline polyethylene (PE) films. First, we will present our measurements of partially oriented PEs; a qualitative analysis on the microscopic property based on the combination of the bulk thermal and structural characterization will follow. Next, we resolve the MFPs of heat-carrying acoustic phonons in highly oriented PE to reveal the origin of the thermally conductive polymers.

4.1 Background

Thermally conductive polymers are of interest both for fundamental materials science as well as applications such as thermal management [4, 93]. Despite the low thermal conductivity $\sim 0.1 - 0.6 \text{ W m}^{-1} \text{ K}^{-1}$ of unoriented polymers [4], early works

reported orders of magnitude increase in uniaxial thermal conductivity along the alignment direction of oriented samples, including for polyethylene (PE) [8, 94], polyacetylene [5], and polypropylene [6]. In particular, the reported thermal conductivity of oriented polyethylene ranged from $\sim 14 \text{ Wm}^{-1}\text{K}^{-1}$ [95] for draw ratio $DR = 25$ up to $\sim 40 \text{ Wm}^{-1}\text{K}^{-1}$ for solution processed PE with a DR of 350 [96]. The enhancement was attributed to increased chain alignment along the drawing direction [94], phonon focusing in the elastically anisotropic crystalline phase [97], and increased crystallinity [98, 99]. Recently, reported thermal conductivities have increased further, with values of $\sim 50 - 100 \text{ Wm}^{-1}\text{K}^{-1}$ reported in nanocrystalline fibers. [100, 101] Advances in synthesis have led to the fabrication of disentangled ultra-high molecular weight PE (UHMWPE) [102] with reported thermal conductivities up to $60 \text{ Wm}^{-1}\text{K}^{-1}$ in bulk films [9, 103]. Recent works have also reported high thermal conductivity up to $20 - 30 \text{ Wm}^{-1}\text{K}^{-1}$ in a diverse set of polymers besides PE, including polybenzobisoxazole, [104] polyethylene oxide [105], and amorphous polythiophene [10].

Diverse methods have been employed to understand the origin of the increased thermal conductivity in aligned polymers. Numerical studies have provided insights into the properties of heat-carrying phonons in perfect polymer crystals, including with empirical [106] and ab-initio [107–109] interatomic potentials, but oriented polymer samples exhibit a structure far more complex than that of a perfect crystal. As a result, many studies have focused on understanding the structural changes that occur during drawing. The accepted picture is that an initial crystalline fraction on the order of $\sim 60 - 70\%$ exists in nascent polyethylene [96, 110–112]. On initial drawing, the crystallites begin to align and a periodic lamellar structure, consisting of alternating crystalline and amorphous domains, develops [113, 114]. Small angle X-ray Scattering (SAXS) has been used to measure the period of the lamellae as around ~ 8 to 40 nm , and that corresponding size of the crystalline domain consisting of the lamellae is around $10 - 20 \text{ nm}$ [115, 116]. For $DR < 20$, the crystallinity also increases under drawing as measured using wide angle X-ray scattering (WAXS) up to $\sim 80 - 90\%$ [111, 117].

Below DR100, although the thermal conductivity increased with drawing, the degree of the crystallinity and crystallite size did not exhibit as strong a trend with DR. The crystallinity was reported to increase only by 10% , despite substantial change in the DR from 20 to 100. [111, 118] While some prior studies reported increase in the crystallite size from $\sim 30 \text{ nm}$ to $\sim 70 \text{ nm}$, nearly three-fold increase, with

drawing from [119], others reported the opposite trend [115, 120]. Furthermore, the scattered intensity with SAXS was observed to decrease with increasing DR [121–123], indicating the transformation from the periodically alternating lamellar structure to a different one such as inter-crystalline bridges [95, 115] or continuously extended rigid crystal structure [115, 120].

The presence of such an extended crystal was identified by measurements in highly oriented PE using solid-state NMR [124] along with SAXS [120]. In particular, Litvinov et al. have measured the dimension of crystalline domain along the chain direction around 100 - 250 nm, far exceeding the lamella period length (40 nm) measured from SAXS in the same structure. [120]. Since the upper limit of the detectable size from NMR is around 200 nm, the actual dimension of such crystal was thought to be greater than the measured value [120]. The elongated crystals in highly oriented PE thin films were observed to have length as long as several microns yet with diameter in the range of 9 - 20 nm (Transmission electron microscope [125, 126]), 14 - \sim 20 nm (SAXS and WAXS [119, 120, 127]), and 10 nm (solid-state NMR, [124]).

Various models have been proposed to understand the evolution of the uniaxial thermal conductivity under drawing. Two-phase effective medium models with series thermal resistances for each phase have been considered, including the Helix-coil model [98, 128], a modified Maxwell model [129], and the Takayanagi model [130]. Choy et al. have shown that the thermally isotropic Maxwell model best describes the thermal conductivity in low DR ($DR \leq 5$) [129]. The Takayanagi model considers an additional thermal conduction channel along the inter-crystalline bridge [130]; this model better explained the measured thermal conductivity for $DR > 5$, possibly due to the presence of such structures in higher DR samples. Xu et al. used the isotropic helix-coil model and concluded that the thermal conductivity of the amorphous phase (κ_a) must be as high as $16 \text{ Wm}^{-1}\text{K}^{-1}$ to explain their thermal conductivity measurements [9]. Ronca et al. have used the same model, but reported that the high thermal conductivity originates from the increased thermal conductivity in the crystalline domain (κ_c) as high as $47 \text{ Wm}^{-1}\text{K}^{-1}$ [103]. The reason for the discrepancy is that the theory requires the characteristic length of the repeated periodic structure that may not exist in actual ultra-drawn samples. Also, the bulk properties that are free parameters in the theory (κ_c, κ_a) are challenging to individually measure, hitherto yielding significant differences in measured κ_a s [9, 103]. In addition, the theory does not account for possibility of phonons transmitting across

domain boundaries, in which case the effective medium treatment is no longer valid. Evidence of such processes has been reported even in partially oriented PE samples with low DR ~ 7.5 using transient grating spectroscopy [131]. As a result, the microscopic properties of heat-carrying phonons and the origin of the high thermal conductivity of highly oriented polyethylene remain a topic of debate.

In this chapter, we report that the dominant heat-carrying phonons in highly oriented polyethylene exhibit mean free paths on micron length scales using transient grating spectroscopy. The mean free paths exceed those in samples of lesser draw ratio by an order of magnitude, indicating that the high thermal conductivity of the present samples primarily arises from decreased structural scattering in the crystalline phase. The decreased structural scattering in turn could arise from larger crystalline domains as well as higher transmissivity across crystalline-amorphous boundaries in the highly aligned samples. Our work provides insight into the microscopic transport properties of heat-carrying phonons in highly oriented polyethylene that will support efforts to create PE samples with higher thermal conductivity.

4.2 Bulk thermal property of PE

Sample: polyethylene

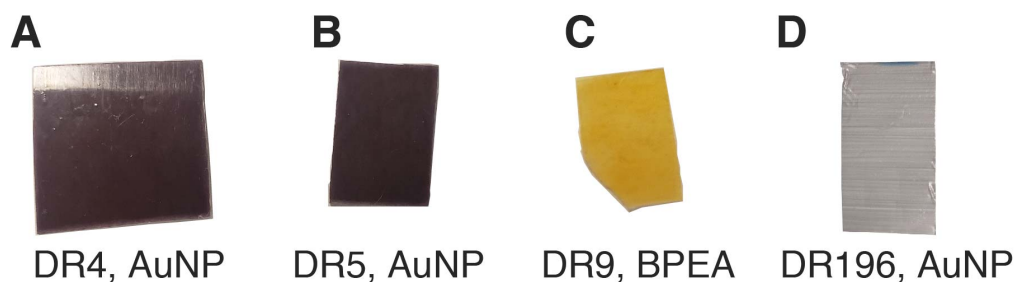


Figure 4.1: Samples that were presented in this thesis. The dye was included to increase the absorption of the visible wavelength. (A) DR4 with AuNP, (B) DR5 with AuNP, (C) DR9 with BPEA, (D) DR196 with AuNP. The concentration of dye is only 1% to minimize the filler effect on the thermal conductivity, while ensuring sufficient absorption of the visible light. Note that the diameter of the AuNP is 2-5 nm.

The samples that are presented in this chapter were fabricated by our collaborators at Loughborough University in the UK. Briefly, the samples are disentangled UHMWPE synthesized using the same procedure described in Ref. [37, 102, 103]. The synthesized samples were drawn by the processes with a particular draw ratio (DR) given by the length of the film before and after the drawing processes. Typ-

ically, partially drawn samples are prepared using compression molding process. Similarly, our partially oriented samples (DR4, DR5, and DR9) were compression molded. For the highly oriented sample (DR196), the film was rolled ($\times 7$) and stretched ($\times 28$) to achieve the high draw ratio. Since PE is transparent to visible light, low concentration of the dye was added to minimize the effect of the filler on the thermal conductivity while enabling the formation of a thermal grating on the sample. Specifically, 9,10-Bis(phenylethynyl)anthracene (BPEA) 1% was added for DR9. Similarly, the concentration of added gold nanoparticle (AuNP, diameter of 2-5 nm) for other samples is only 1% [132, 133].

Since the purpose of the drawing is to make the fiber oriented along a certain direction, we characterized the fiber alignment using scanning electron microscope (SEM) and helium-ion microscope (HIM). For comparison, an SEM image of partially oriented sample (DR7.5 with ZnO nanoparticles) is shown in Fig.4.2 in which we do not see obvious alignment of the fibers. On the other hand, our DR196 samples demonstrated clear aligned fibers that are extended over tens of micron scales as shown in Fig. 4.2.

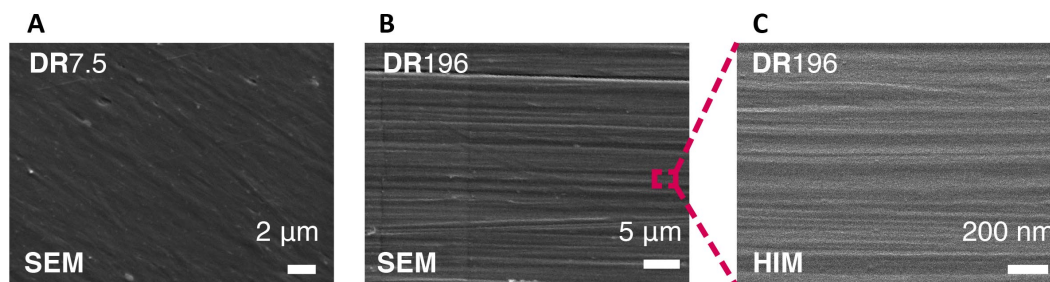


Figure 4.2: High resolution microscopic images of the oriented PE. (A) Literature data of DR7.5 [134]. The chain alignment is not evidently visible. (B) SEM (C) HIM image of the highly oriented PE. The evidence of the extended chain over a micron distance is clearly visible.

As mentioned in the previous chapter, it is important to avoid surface instability for the application of the TG to the thin films. For PE, experimental challenge is related to the following factors especially for highly drawn samples. First, the striations present in the entire sample of DR196, as evidenced in Fig. 4.1D can inhibit the formations of the thermal grating profile over micron scale distances. Second, surface inhomogeneity introduced during the drawing process can scatter the visible light over the length scale comparable to the optical wavelength, which can substantially decrease the signal-to-noise ratio (SNR). Therefore, we imaged the

optical topography as shown in Fig.4.3. The AFM crosscut perpendicular to fiber alignment direction (dashed line in Fig.4.3. A) is shown in Fig.4.3. B. Calculated RMS roughness is ~ 70 nm, and the maximum peak-to-valley difference is ~ 360 nm. The height difference indicates the surface inhomogeneity over length scales comparable to the optical wavelength (515 nm) used.

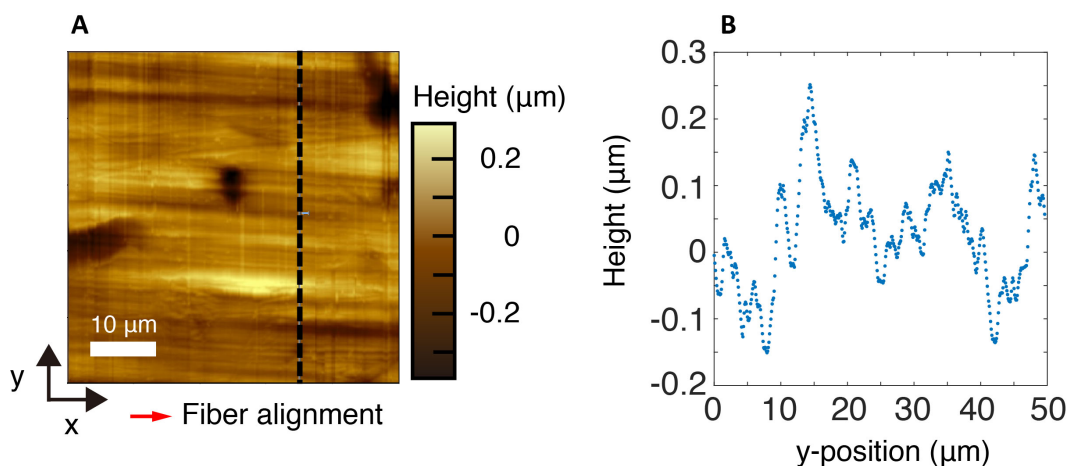


Figure 4.3: AFM characterization of the PE surface. (A) AFM topographic image of the sample. The x and y direction indicates parallel to, perpendicular to the fiber alignment, respectively. (B) AFM crosscut along the dashed line in (A). RMS roughness is calculated to be ~ 70 nm, and the maximum peak-to-valley difference is ~ 360 nm.

4.3 TG application on highly oriented PE

Description of the TG system

We measured the in-plane thermal conductivity of several semi-crystalline polyethylene (PE) films including highly oriented PE using transient grating spectroscopy. The transient grating setup is identical to that described in Ref. [131]. Briefly, a pair of pump pulses (wavelength 515 nm, spot diameter $530 \mu\text{m}$, pulse duration ~ 1 ns, pulse energy $13 \mu\text{J}$, repetition rate 200 Hz) is focused onto the sample to impulsively create a spatially sinusoidal temperature rise of period L and wave vector $q = 2\pi/L$. The grating relaxes by heat conduction, and its decay is monitored by the diffraction of a pair of continuous wave laser beams (wavelength 532 nm, spot diameter $470 \mu\text{m}$, average power $900 \mu\text{W}$, chopped at 3.2 % duty cycle to reduce steady heating on the sample).

Bulk thermal conductivity characterization

First, we examined bulk thermal conductivity. More precisely, uni-directional thermal conductivity and the role of the drawing to the thermal anisotropy were characterized. For this purpose, the TG experiments on several PE films with different draw ratio were performed. Figure 4.4 shows representative signal traces for samples with different draw ratios. The sample was placed parallel to the TG axis.

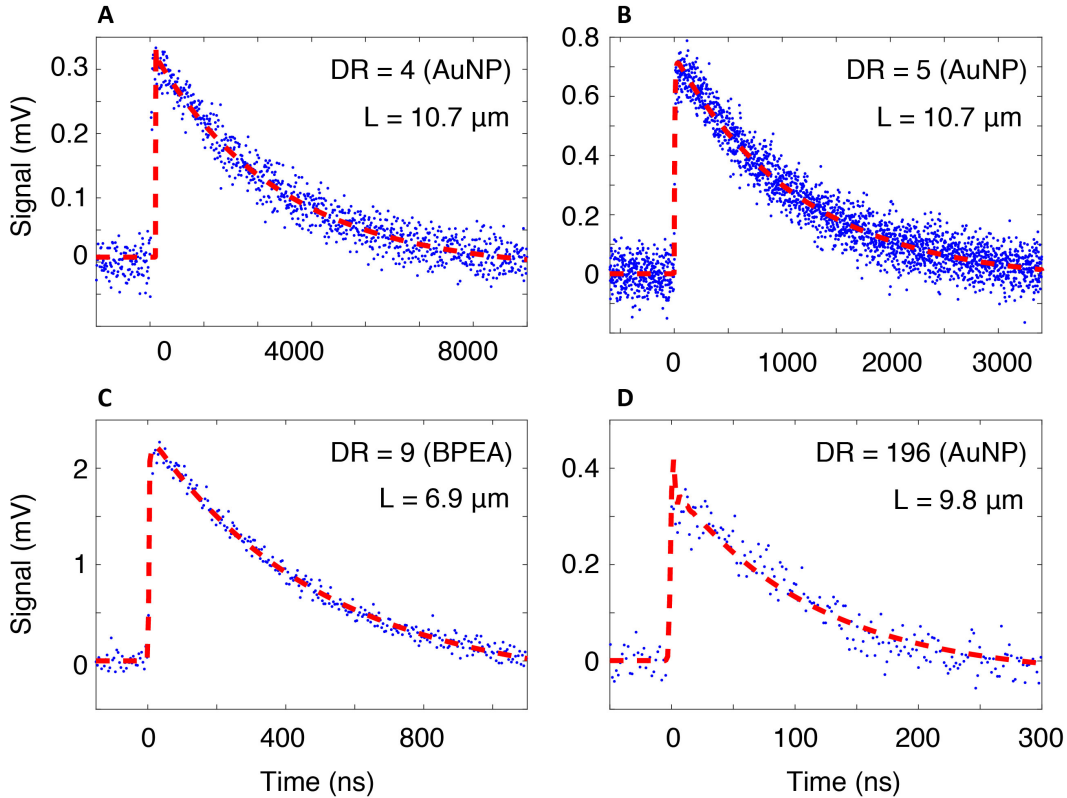


Figure 4.4: Signal magnitude versus the time for several PE films along the transient grating setup. (A) DR4 with AuNP, (B) DR5 with AuNP, (C) DR9 with BPEA, (D) DR196 with AuNP. The symbols indicate that the signal is an average of 3×10^4 repetitions. The dashed line is an exponential fitting with an equation given in Eq. 4.1.

As discussed in Ref. [134], there are various non-thermal decay components with different magnitude and time constants in TG measurements on PE. Therefore, we fit the signal following Ref. [134]

$$f(t) = c_1 + u(t) \left[c_2 + \sum_{m=1}^3 A_m \exp[-t/\tau_m] \right] \quad (4.1)$$

where $u(t)$ is Heaviside unit step function, $c_{1,2}$ is the background before and after $t = 0$, A is the initial magnitude of the decay, and τ is the decay time constant. In

Eq. 4.1, the index $m = 1$ indicates the thermal signal component as a dominant decay component for the signal in Fig. 4.4. The index $m = 2$ ($m = 3$) corresponds to the electronic response (long-term relaxation) with a time-constant on the order of ps ($10 - 30 \mu\text{s}$); detailed description on the physical origin of each non-thermal source can be found in [134]. The dashed lines in Fig. 4.4 show corresponding fits from Eq. 4.1, which well-describe the measured data. We note that the signal magnitude as well as the corresponding SNR in Fig. 4.4D is noticeably small compared to Figs. 4.4A-C due to the surface instability in DR196. As a comparison with prior TG experiments, the SNRs of the DR196 are generally less than 20, which is about a third of that from $DR = 7.5$ reported in Ref. [131].

Next, we measured angle-resolved thermal conductivity for the samples mentioned above. As mentioned in many prior literatures including Ref. [134], the thermal conductivity of semi-crystalline PE depends on the angle, with a substantial decrease at the perpendicular direction due to the thermal anisotropy. We systemically varied the angle by rotating the sample with respect to the principle TG axis. Examples of resulting angle-resolved thermal conductivities are shown in Fig. 4.5, in which 0 (90) degree indicates the heat-flow direction along (perpendicular to) the chain orientation. Following Ref. [134], we fit the thermal conductivity versus the angle given in Fig. 4.5, using an expression given by

$$\kappa = \kappa_{\parallel} \cos^2 \theta + \kappa_{\perp} \sin^2 \theta \quad (4.2)$$

where κ_{\parallel} (κ_{\perp}) is the thermal conductivity at 0 degree (90 degree). The above expression is a geometric model considering that the heat flow into each direction independently contributes to the heat transfer, similar to the assumption in prior effective medium models used for polymers [98, 128, 130]. The dashed lines in Fig. 4.5 show that the geometric model can well describe the data.

By comparing the value κ_{\parallel} , we can estimate the ratio of heat flow anisotropy. The anisotropy is defined by $\kappa_{\parallel}/\kappa_{\perp}$. We see that the maximum thermal conductivity at DR4 is $\kappa_{\parallel} = 4.2 \pm 0.4 \text{ Wm}^{-1}\text{K}^{-1}$, which decreases to $\sim 1 \text{ Wm}^{-1}\text{K}^{-1}$ with an anisotropy ~ 4.2 . On the other hand, for DR 196, the κ_{\parallel} is $42 \pm 3 \text{ Wm}^{-1}\text{K}^{-1}$, and κ_{\perp} is $\sim 0.4 \text{ Wm}^{-1}\text{K}^{-1}$, resulting in an anisotropy ~ 105 . The draw ratio dependence of κ_{\parallel} , κ_{\perp} for DR3 to 196 is shown in Fig.4.6A. The value of κ_{\parallel} is $\sim 3 \text{ Wm}^{-1}\text{K}^{-1}$ for DR3, which is around 5 times larger than κ_{\perp} . The κ_{\parallel} increases as the DR increases up to DR66, above which the observed value saturates to $\sim 40 \text{ Wm}^{-1}\text{K}^{-1}$. The opposite trend is observed for κ_{\perp} , which approaches to $0.4 \text{ Wm}^{-1}\text{K}^{-1}$. Note that

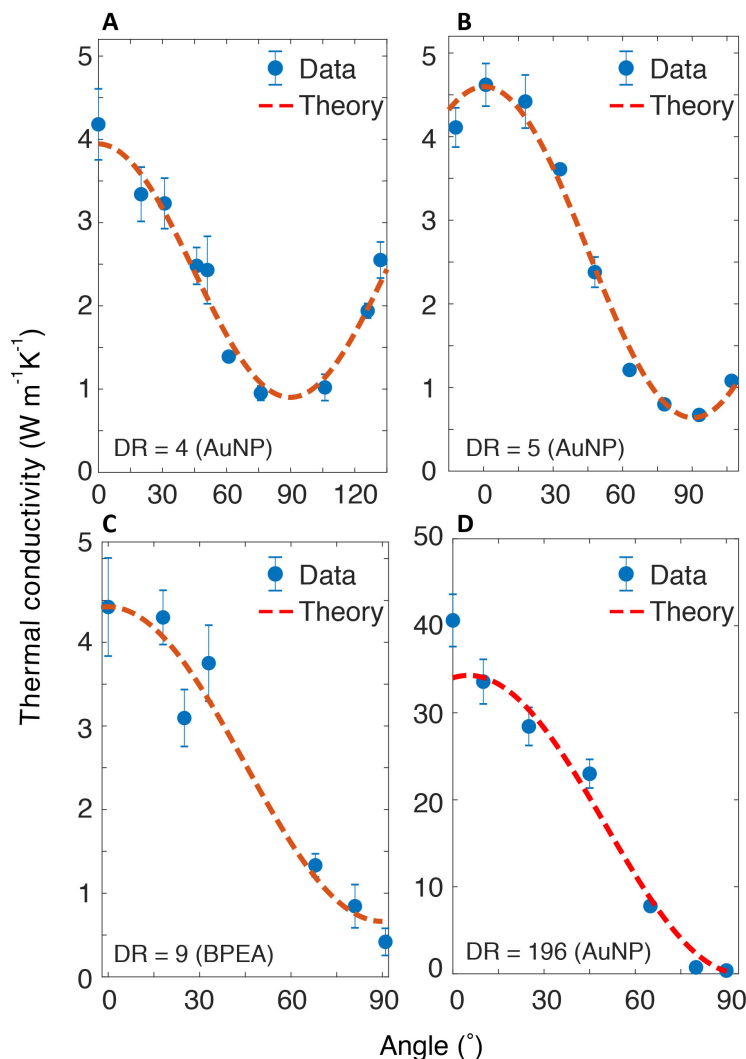


Figure 4.5: Thermal conductivity versus angle between draw direction and thermal gradient defined by a grating period. (A) AuNP4 at $L = 10.7 \mu\text{m}$ with $\kappa_{\parallel} = 4.2 \pm 0.4 \text{ Wm}^{-1}\text{K}^{-1}$), (B) AuNP5 at $L = 10.7 \mu\text{m}$ with $\kappa_{\parallel} = 4.6 \pm 0.3 \text{ Wm}^{-1}\text{K}^{-1}$), (C) BPEA9 at $L = 6.9 \mu\text{m}$ with $\kappa_{\parallel} = 4.4 \pm 0.6 \text{ Wm}^{-1}\text{K}^{-1}$), (D) AuNP196 $L = 10.7 \mu\text{m}$ with $\kappa_{\parallel} = 42 \pm 3 \text{ Wm}^{-1}\text{K}^{-1}$). The 0 (90) degree indicates heat flow direction parallel to (perpendicular to) the draw direction. The maximum value of the thermal conductivity occurs along the chain, while the perpendicular value is comparable to that in bulk PE. Dashed lines indicate fits using the Eq. 4.2

the value of $\kappa_{\perp} \sim 0.4 \text{ Wm}^{-1}\text{K}^{-1}$ is close to the value in unoriented PE, which is attributed to the heat conduction by interchain van der Waals interactions as in the bulk PE [129]. Corresponding ratio of the thermal conductivity ($\kappa_{\parallel}/\kappa_{\perp}$) is shown in Fig. 4.6B. Above DR66, the measured anisotropy was observed to be $\sim 100 - 150$.

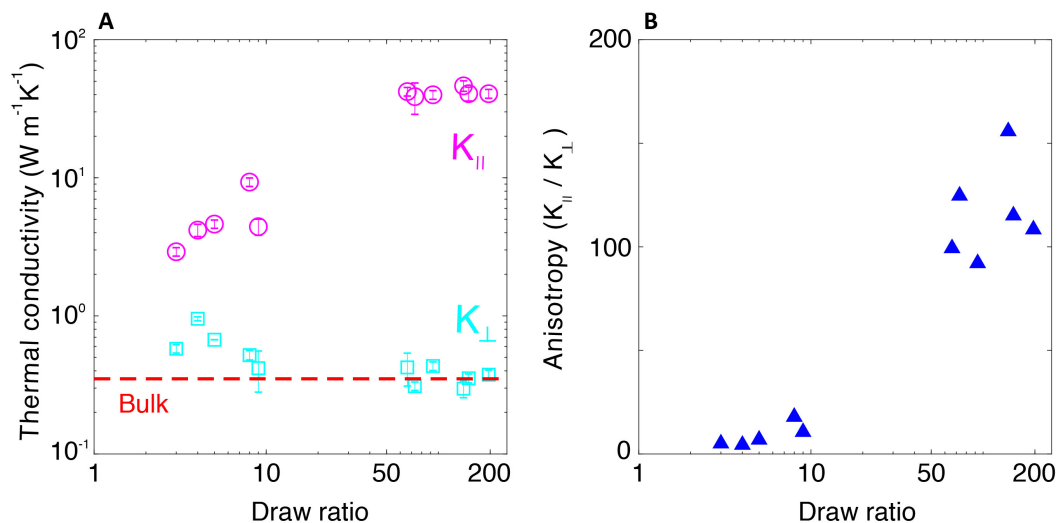


Figure 4.6: (A) κ_{\parallel} and κ_{\perp} versus the draw ratio. The draw ratio is from 3 to 196. With draw ratio, the κ_{\parallel} increases from $\sim 3 \text{ W m}^{-1} \text{ K}^{-1}$ to $\sim 40 \text{ W m}^{-1} \text{ K}^{-1}$ up to DR 66, above which the value saturates. The κ_{\perp} decreases and approaches to the bulk value as the draw ratio increases, which is attributed to the heat conduction by interchain van der Waals interactions as in the bulk [129]. (B) The anisotropy ($\kappa_{\parallel} / \kappa_{\perp}$) versus the draw ratio. We see that the anisotropy increases as the draw ratio increases up to $\sim 100 - 150$ above DR66.

Thermal conductivity versus the temperature

Having characterized the effect of the DR on the thermal anisotropy, we now seek for inferring the microscopic thermal transport properties. In semi-crystalline PE with low DRs, the structural properties are known to limit the heat-carrying process [37], we can qualitatively extract the microscopic heat transport by relating temperature dependent thermal conductivity to the structural property.

First, the thermal conductivity versus the temperature for two samples with similar DRs is shown in Fig. 4.7AB. Due to the low DRs, thermal conductivity exhibits an increase with temperature indicating substantial structural scattering, in agreement with a prior study [37]. The feature $\sim 200 \text{ K}$ is attributed to the glass transition [37].

The results from DR196 at $L = 9.8 \mu\text{m}$ is shown in Fig. 4.8. The bulk thermal diffusivity along the chain direction versus the temperature is plotted in Fig. 4.8A. A linearly increasing trend with decreasing temperature is observed. The corresponding bulk κ_{\parallel} versus temperature is shown in Fig. 4.8B. The thermal conductivity remains constant within the measurement uncertainty from room temperature to $\sim 220 \text{ K}$, below which the thermal conductivity decreases. The trend of the thermal conductivity below 220 K is characteristic of structural scattering.

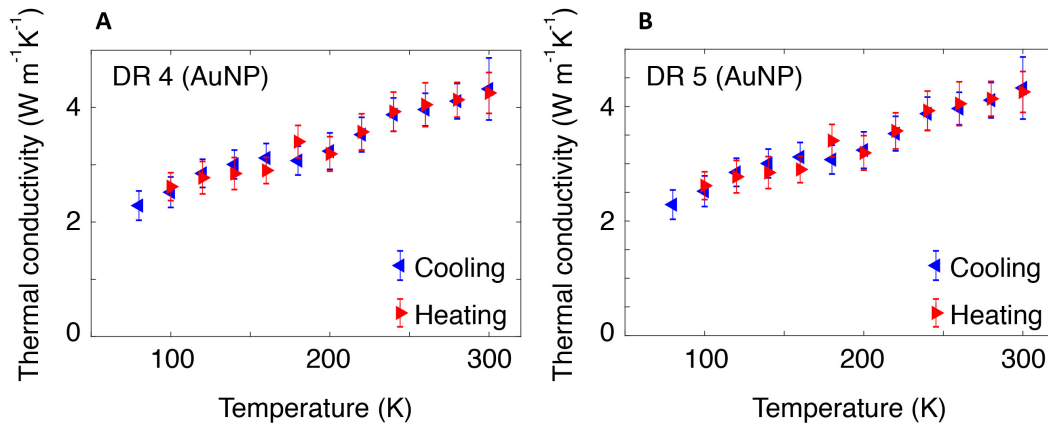


Figure 4.7: Thermal conductivity versus temperature at $L = 10.7 \mu\text{m}$ for (A) DR4 with AuNP, and (B) DR5 with AuNP. With temperature, the thermal conductivity exhibits a monotonic increase, characteristic of the phonon-domain boundary scattering. A hump near 200 K is associated with the glass transition temperature of the PE.

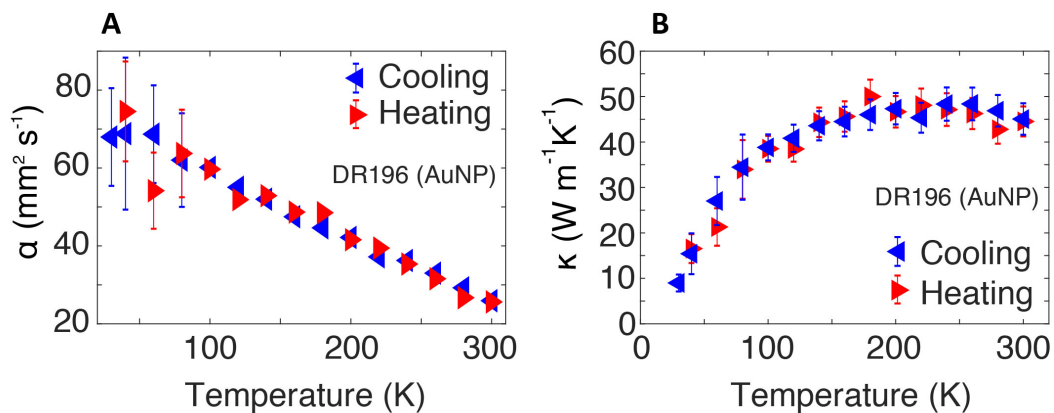


Figure 4.8: Temperature dependent bulk thermal properties of DR196 with AuNP. (A) Thermal diffusivity along the chain axis versus the temperature at a grating period $L = 9.8 \mu\text{m}$. With decreasing temperature, linear increase in the thermal diffusivity is clearly observed. (B) Thermal conductivity along the chain versus the temperature at a grating period $L = 9.8 \mu\text{m}$. The thermal conductivity was calculated using reported heat capacities for linear PE in Ref. [135] The thermal conductivity is approximately constant from 300– ~ 220 K, below which the thermal conductivity decreases.

The above thermal conductivity versus the temperature can be used to infer the microscopic heat transfer properties. For example, comparing Fig. 4.7AB, while we can find an evidence of structural scattering, there is not an obvious difference between them, implying that micro-structures in both samples would be similar. A direct

evidence for structural scattering is shown in Fig. 4.7C. Figure 4.9 shows structural characterization of the PE with AuNP using WAXS and SAXS. The measurements were performed by our collaborator [133]. The measurements demonstrate that the crystallinity of $\sim 74\%$ and an average lamella spacing around 8 - 22 nm [132, 133], and that the micro-structural properties in both DR4 and DR5 are similar. From the results in Fig. 4.9, we can tentatively conclude that the phonons may propagate a distance order of 10 nm.

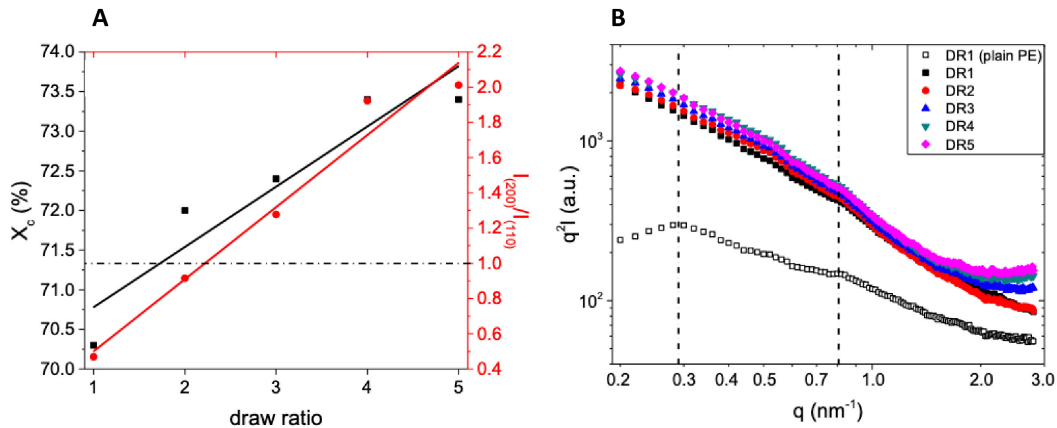


Figure 4.9: SAXS and WAXS characterization in PE with AuNPs. The data were taken from Ref. [133]. (A) Left axis: Crystallinity of PE with AuNP. For DR4 and 5, the crystallinity was measured to be 73.5%. Right Axis: The ratio of WAXS intensity peak over a narrow q range near (200) reflection to the (110) reflection from which the crystallinity was extracted. (B) Thickness-normalized Lorentz corrected SAXS intensity profiles measured from PE with AuNP. The dashed lines indicate the wave vector of the intensity bump around $q = 0.29 \text{ nm}^{-1}$ and $q = 0.8 \text{ nm}^{-1}$, respectively. Corresponding lamella long-period of the crystalline lamella ($d = 2\pi/q$) is around 8 - 22 nm.

However, the above qualitative approach is not applicable for highly oriented samples, since corresponding domain sizes are inaccessible using SAXS and WAXS [124]. According to the prior reports, the SAXS intensity disappears for $\text{DR} \geq 80$, mainly attributed to the marginal fraction of the amorphous fraction or the presence of the extended crystals [9, 124]. Furthermore, the measurements of temperature-dependent thermal conductivity alone cannot rigorously examine other microstructural properties such as distribution of the phonon MFPs and corresponding transmission and reflection of phonons at the domain boundary.

4.4 Grating period dependent thermal conductivity

In the preceding section, we have demonstrated the capability of the TG to measure angle- and temperature-dependent thermal conductivity and that enables to infer qualitative information of the microscopic heat-transport properties. In this section, we systematically vary the relevant thermal length scale comparable to the mean free path, therefore provide a basis for understanding microscopic transport properties.

We measured the thermal conductivity along the parallel direction versus the grating period at temperatures of 300 K, 220 K, 100 K, and 30 K. The raw signal traces are given in Fig. 4.10.

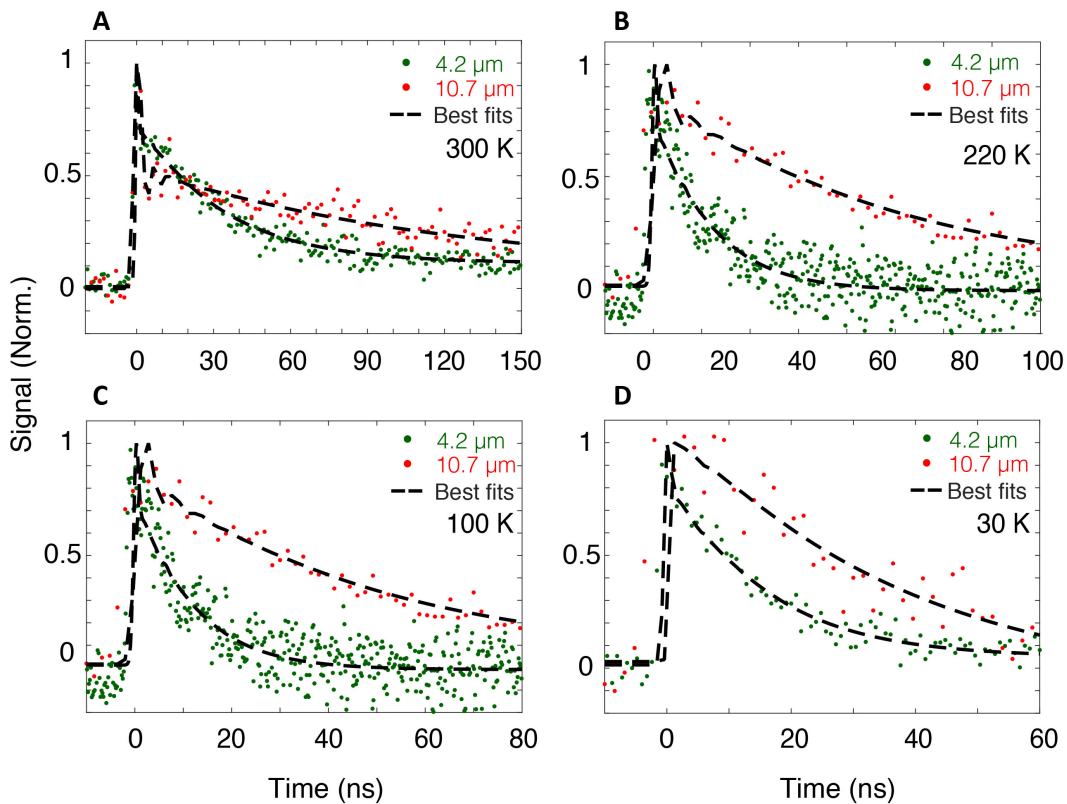


Figure 4.10: Measured TG signal versus time (symbols) at several grating periods for DR196 at (A) 300 K, (B) 220 K, (C) 100 K, (D) 30 K. The signal shown are normalized by its initial magnitude at $t = 0$. The dashed lines are fit using Eq. 4.1. Error bars indicate 95 % confidence intervals obtained using an identical procedure as that in Ref. [131].

If heat-carrying phonons propagate ballistically over the grating period, the thermal decay is slower than that predicted from the bulk thermal conductivity [33, 35]. Representative TG signal for a grating period of $L = 1.5 \mu\text{m}$ at 300 K is shown in Fig. 4.11 A. The decay is clearly slower than expected based on the bulk thermal

conductivity value, indicating the presence of ballistic phonons on the length scale of the grating period. Measurements of the decay rate versus q^2 for all the grating periods at 300 K are given in Fig. 4.11. The measured decay rate is close to that predicted by the bulk thermal conductivity at $q^2 \leq 0.3 \mu\text{m}^{-2}$, above which the decay rate is slower by up to a factor of 5 at the smallest grating period.

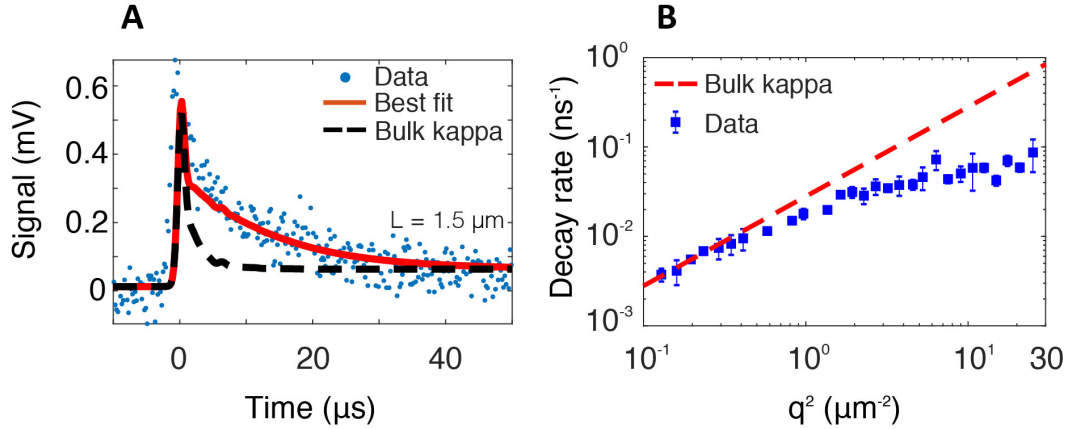


Figure 4.11: (A) Measured TG signal versus time (symbols) for grating period $L = 1.5 \mu\text{m}$, corresponding to $q^2 \sim 17.5 \mu\text{m}^{-2}$, along with the best fit (solid red line) and expected decay using the bulk thermal conductivity (dashed black line). The signal is an average of 5×10^4 shots measured at a single location. The signal clearly decays slower than predicted from bulk thermal conductivity, evidence of the departure from the diffusive thermal transport. (B) Decay rate versus q^2 . The measured decay rates for $q^2 \gtrsim 0.3 \mu\text{m}^{-2}$ deviate from that predicted from bulk thermal conductivity, indicating that the heat-carrying phonons transport ballistically.

Corresponding measured thermal conductivity versus grating period at 300 K - 300 K, is shown in Fig. 4.12 A - D. The thermal conductivity is nearly constant at large grating period ($L \geq 10 \mu\text{m}$), below which a grating period dependence is observed. Note that the grating period dependence in DR 196 is much stronger than that reported in partially oriented PE [131], indicating the presence of heat-carrying phonons with longer MFPs in the present highly oriented samples. A similar grating period dependence was also observed at all the temperatures. Noting that the apparent thermal conductivity at $L = 6 \mu\text{m}$ is around half of the bulk value, the measurements imply that heat-carrying phonons with MFPs above $\sim L/2\pi \sim 1 \mu\text{m}$ carry half the heat over 30 - 300 K.

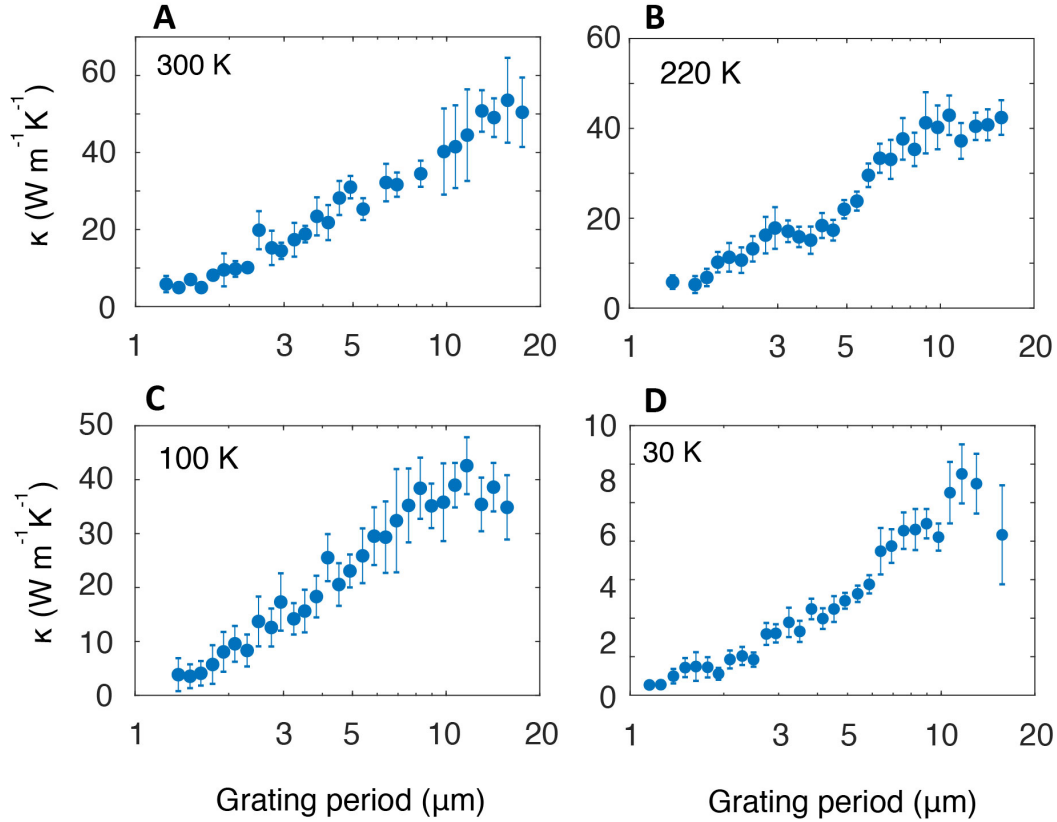


Figure 4.12: Thermal conductivity versus grating period at (A) 300 K, (B) 220 K, (C) 100 K, (D) 30 K. The thermal conductivity clearly depends on the grating period at both temperatures. With decreasing grating period, the measured thermal conductivity levels off to a constant value at $L \sim 10 \mu\text{m}$, below which the value substantially decreases. Particularly at all the temperatures, the value is reduced nearly 50% from its bulk value at $L \sim 5 - 6 \mu\text{m}$, which corresponds to thermal length $d \sim L/2\pi \sim 1 \mu\text{m}$. Error bars indicate 95 % confidence intervals obtained using an identical procedure as that in Ref. [131].

4.5 Ballistic transport of the heat-carrying phonons in DR196

Regarding the grating dependent thermal conductivity, the evidence of the ballistic transport of heat-carrying phonons can be used to characterize the spectrum of MFPs of phonons. In this section, we review the approach to reconstruct the MFP of heat-carrying phonons.

Background

We start from the kinetic theory form of the thermal conductivity. Here, we express the quantity in the MFP domain. For a bulk substance, the accumulated thermal

conductivity at a given MFP (Λ) is defined as

$$\kappa_{bulk} = \int_0^{\infty} f(\Lambda) d\Lambda_{\omega} \quad (4.3)$$

where $f(\Lambda)$ is a differential form of the thermal conductivity at a given MFP in the unit of $Wm^{-2}K^{-1}$. In TG, as the thermal length scale becomes smaller, the contribution of the heat-carrying phonons with longer MFP to the thermal conductivity start to become smaller. Corresponding thermal conductivity is [35]

$$\kappa_{TG} = \int_0^{\infty} f(\Lambda) S(x) d\Lambda_{\omega} \quad (4.4)$$

where $x = q\Lambda = \Lambda(2\pi/L)$ is the ratio of the MFP to the thermal length scale, and $S(x)$ is the phonon thermal conductivity suppression function. The suppression function is known to be

$$S_{iso} = \frac{3}{x^2} \left(1 - \frac{\tan^{-1}(x)}{x} \right) \quad (4.5)$$

$$S_{arb} = \frac{1}{1+x^2} \quad (4.6)$$

where S_{iso} is the suppression function for the isotropic material such as silicon [34], and S_{arb} is that for the anisotropic material with an arbitrary dispersion [34]. Since the PE is thermally anisotropic, we use $S = S_{arb}$ in the following analysis.

Due to the nature of the cumulative form of the thermal conductivity using an integration by parts, Eq. 4.4 can be expressed as

$$\kappa_{TG} = \int_0^{\infty} qK(x)F(\Lambda_{\omega})d\Lambda_{\omega} \quad (4.7)$$

where $K(x) = -dK/dx$ is the Kernel function. The Eq. 4.7 is known to be ill-posed, therefore cannot be uniquely solved. Nevertheless, Eq. 4.7 is still useful, since the Eq. 4.7 does not require any prior knowledge concerning the microscopic properties such as phonon dispersion and frequency dependent scattering mechanism.

A way to solve the problem (Eq. 4.7) is Bayesian inference used in several recent works [37, 47]. The details are described in [47, 131]. Here, we briefly explain the Bayesian inference that was used in this thesis. Following the procedures in Ref [131], we performed iterative n steps to search for posterior solution $F_{post}(\Lambda)$ based on $F_{prior}(\Lambda)$ given the measurements. The following is the inference procedures for sampling $F_{post}(\Lambda)$ in each steps. First, we assumed a profile of cumulative thermal conductivity versus the mean free path $F_{j-1}(\Lambda)$ for $j = 1, 2 \dots n$. Next,

we sampled posterior profile $F_j(\Lambda)$ based on the Metropolis-Hasting Markov chain Monte Carlo algorithm. We then computed the likelihood of the posterior probability (P_{post}) given the experiment

$$P_{post}(F_j|\kappa_{expt}) \propto P(\kappa_{expt}|F_j)P_{prior}(F_j) \quad (4.8)$$

$$P_{prior}(F_j) \propto \exp\left(\frac{1}{-2\gamma^2} \int \frac{d^2 F_j}{d\Omega^2} d\Omega\right) \quad (4.9)$$

$$P(\kappa|F_j) \propto \exp\left(-\sum_i \frac{\kappa_i - \kappa_{calc,i}(F_j)}{2\sigma_i^2}\right) \quad (4.10)$$

where γ is a standard deviation for second drivative, κ_i (σ_i) is the measurements (experimental error bound), and $\Omega = \log 10(\Lambda)$, Finally, we accepted the posterior profile with an acceptance probability α given by

$$\alpha(F_j, F_{j-1}) = \min\left[1, \frac{P(F_j)}{P(F_{j-1})}\right] \quad (4.11)$$

Otherwise, we update $F_j = F_{j-1}$.

MFP accumulation in DR196 from Bayesian inference

Using the Bayesian inference mentioned in the previous section, the thermal conductivity accumulation ($F(\Lambda)$) versus the phonon mean free path that best explains the experimental observations in DR196 were extracted.

The reconstructed MFP accumulations are given in Fig. 4.13. In Fig. 4.13, the intensity of the shaded region corresponds to the density of the posterior distribution, indicating that the calculated thermal conductivity versus the grating period based on these MFP profile agrees with the measurement. Solid lines (dashed lines) indicate means (95 % credible intervals) of the distribution.

In order to confirm that the predicted $F(\Lambda)$ from the Bayesian inference is accurate, we need to perform the forward calculation using Eq. 4.7 and to compare it with the experiments. The corresponding thermal conductivity versus the grating period from the profiles from the Bayesian inference is shown in Fig. 4.14. In Fig. 4.14, the intensity of the shaded region is the calculation obtained using the MFP profiles, enclosed by 95 % credible intervals (dashed line). The solid lines correspond to the calculation using the mean of the MFP profile. At all the temperature ranges in this work (30 K, 100 K, 220 K, 300 K), we see a good agreement between the calculation and the experiment.

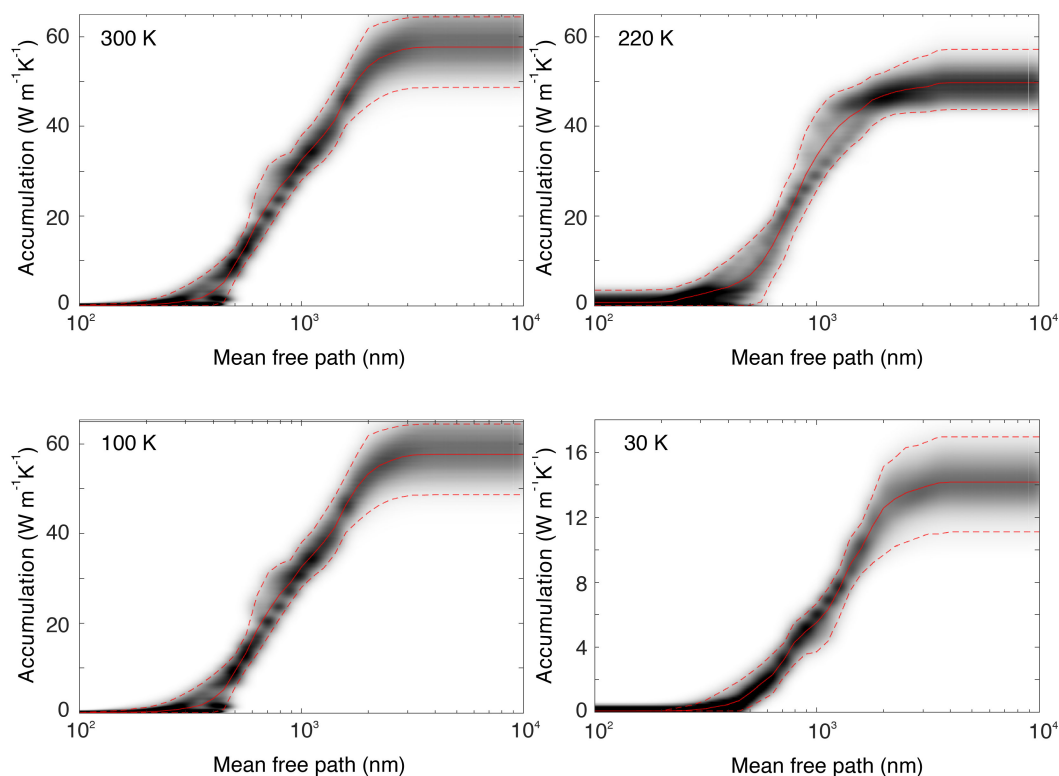


Figure 4.13: Thermal conductivity accumulation versus the mean free path of the thermal phonons in highly oriented PE at (A) 300 K, (B) 220 K, (C) 100 K, and (D) 30 K. The intensity of the shaded region indicates the likelihood of the reconstructed profile. The solid lines (dashed lines) correspond to the mean (95% credible intervals). We observe that the mean free path in this sample is on the order of micron and that the fraction of the heat carried by the mean free path above μm is close to 50% at these temperatures.

We examine the properties of the heat carrying phonon using the obtained MFP distribution in Fig. 4.13. At 300 K, nearly 50% of the heat is carried by phonon with MFP above $1 \mu m$, as expected from the rough estimation described above. The contribution of these phonon to the thermal conductivity does not exhibit strong temperature dependence as in Figs. 4.13B - D. Moreover, the contribution to the thermal conductivity for phonons with MFP below 500 nm is less than 0 - 20%, considering the uncertainties determined from the 95% credible interval. On the other hand, the percentage of the heat carried by MFP below 100 nm is less than 1%. Prior characterization on the MFP has shown that the range of the MFP in partially oriented PE (DR = 7.5%) is in hundreds nanometer range, nearly 200 nm [131]. Our results suggest that the highly oriented PE can support the MFP of the thermal phonon in the range of hundred nanometer to a few micrometer scale as in

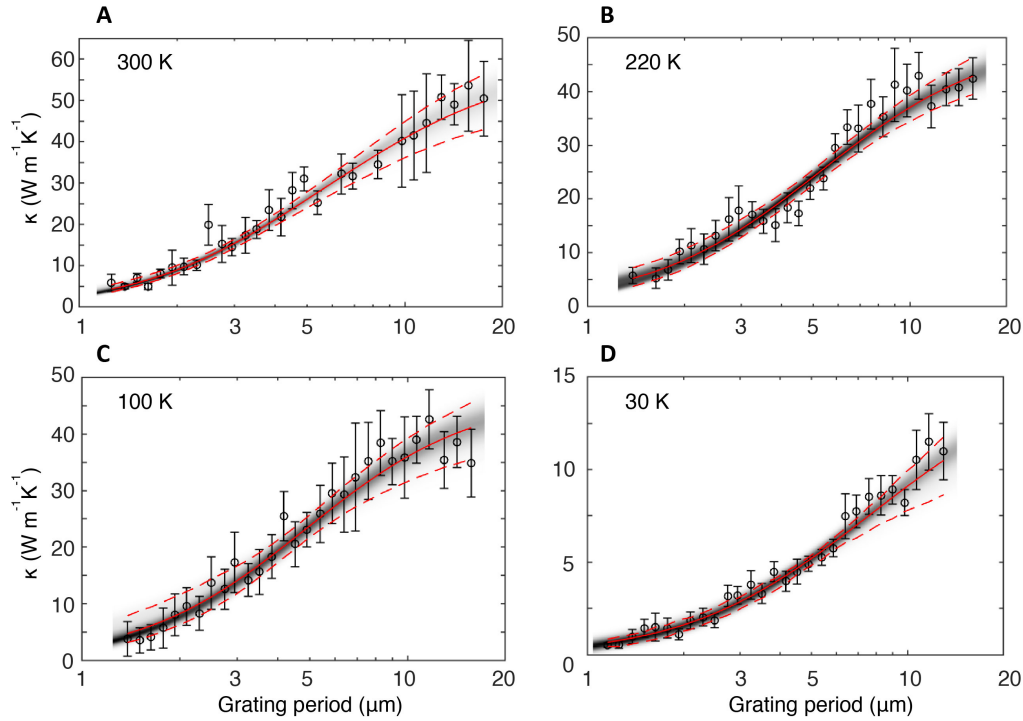


Figure 4.14: The calculation of the apparent thermal conductivity versus the grating period at (A) 300 K, (B) 220 K, (C) 100 K, and (D) 30 K. The intensity of the shaded region is the calculation using the MFP profiles obtained from the Bayesian inference. The dashed (solid) lines corresponds to the calculation using 95 % credible interval (mean) of the MFP distribution described in the main text. The calculation excellently matches with the experiment, indicating that the reconstructed MFP is the most probable solution.

many other covalent crystals that possess high thermal conductivity such as silicon [35]. Furthermore, the fraction of the heat carried by phonons with MFPs < 100 nm is less than 5% at all temperatures, confirming that the phonons are not scattering at the nano crystalline domain size as high as 100 nm. If the phonon-phonon scattering mechanism would dominate, one would expect that corresponding domain of the MFP should significantly increased, which is not the cases here. In other words, for instance, the reduction of thermal conductivity at low temperatures shown in Fig. 4.12 would have occurred at grating periods that are longer than the values presented in Fig. 4.12. Therefore, we tentatively conclude that the phonons are still limited by the domain boundary order of the micron length scale, a scale close to the reported extended crystalline domain size [115, 120].

4.6 Low energy Debye model

As mentioned, the analysis in the MFP domain is beneficial in that the reconstruction does not require prior knowledge of the phonon properties. However, use of an approximate model describing the low energy excitations of PE can help to understand the damping mechanisms. As discussed in prior literature [33, 47], this procedure requires the knowledge of the acoustic dispersion of PE.

4.7 Modeling

For an anisotropic solid, the grating dependent thermal conductivity in Eq.4.7 can be re-written as

$$\kappa_i = \sum_n \int_0^{\omega_m} S_n(x_i) [C_n(\omega)v_n\Lambda_n(\omega)] d\omega \quad (4.12)$$

where n is the index of the polarization, and $\omega_{m,s}$ is the cutoff frequency for phonon that transports heat. The mode-specific heat capacity is expressed as $C_s(\omega) = \hbar\omega D_s(\omega)df_{BE}/dT$ where the $D_s(\omega)$ is the density of states (DOS), and df_{BE}/dT is the temperature derivative of the Bose-Einstein distribution function.

We note from Fig 4.13 that phonons with MFPs on the order of hundreds of nanometers carry the majority of the heat. From the calculations of Ref. [107], the only phonons with such long MFPs are from the LA branch. Therefore, the weakly damped heat-carrying vibrations are likely from this branch. The marked elastic anisotropy of PE can be accounted for to good approximation by assuming that the group velocities all point along the chain axis [108, 136–138]. Therefore, the measured thermal conductivity versus the grating period (k_i) should be simplified as

$$\kappa_{i,LA} = \int_0^{\omega_m} S(x_i) [C(\omega)v\Lambda(\omega)] d\omega \quad (4.13)$$

For our calculation of Eq. 4.13, the ab-initio values of the mode-dependent density of states and dispersive group velocity for LA branch was used. Following Ref. [107], the ab-initio properties were computed using temperature-dependent effective potential (TDEP) with the force constants generated at 300 K [108]. Corresponding DOS and dispersion relation for LA branch is shown in Fig. 4.15. From the dispersion relation, we calculated the dispersive phonon group velocity, which is 17000 m s^{-1} near the Brillouin zone center. Due to finite grid size, extrapolated values of DOS and the group velocity were used in our actual calculation for Eq. 4.13.

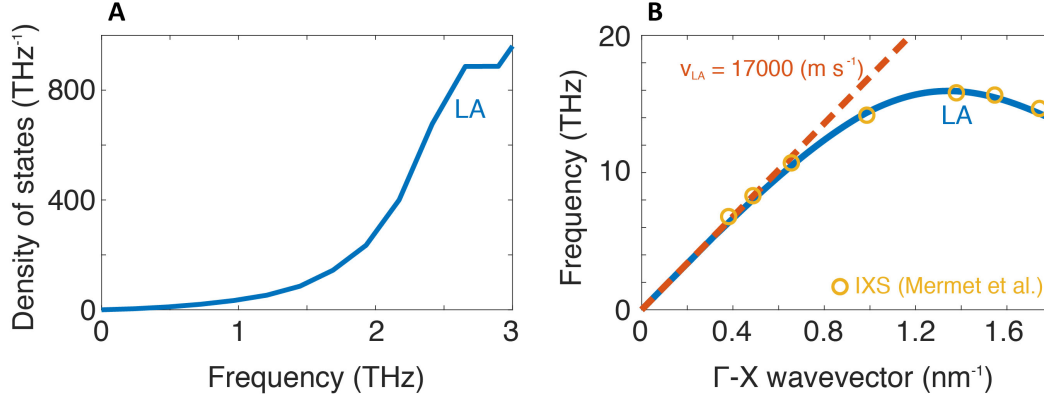


Figure 4.15: Calculated LA phonon properties along the chain obtained using TDEP with force constants generated at 300 K. (A) Density of states. (B) Dispersion relation (solid line). The sound velocity near the Brillouin zone center is around 17000 m s^{-1} (dashed line). The TDEP results agree with prior IXS measurements on PE with DR5.5 (symbols).

We now seek to identify the function $\Lambda(\omega)$ that best explains the temperature dependence and grating dependence of the thermal conductivity. Prior works provide constraints on the values of the MFPs at different frequencies. Inelastic x-ray scattering (IXS) experiments on DR 5.5 have shown that the MFP is around 10 nm at ~ 6 THz. At ~ 1 THz, the dominant LA phonon approximation on prior thermal measurements indicates that the MFPs are ranging from 10 - 50 nm [26, 139–141] as shown in Fig. 4.16. The estimated MFP of LA phonons was obtained using $l_{LA} = \kappa/C_{v,LA}/v_{LA}$ where $C_{v,LA}$ (v_{LA}) was calculated (extrapolated) from the properties shown in Fig. 4.15. First, since the temperature dependent thermal conductivities were measured at relatively low draw ratio compared to our DR196, the corresponding MFP below 1 THz for DR196 should be bigger than order of 10 nm. Second, the cumulative thermal conductivity versus the mean free path lacks of marked temperature dependence as shown in Fig. 4.13, corresponding frequency resolved mean free path should be independent to the temperature. Third, low frequency phonons will experience geometric scattering or boundary scattering due to long-wavelength. Corresponding scattering cross-section forces the lifetime to be constant. Given these constraints, we assumed constant lifetime which yields $\Lambda(\omega) = v_{LA}\tau$.

Based on the constraints, two profiles of $\Lambda(\omega)$ versus the frequency that is compatible with the data (profile 2) was considered as shown in Fig. 4.16. We found that the frequency dependent mean free path, $\Lambda(\omega) = v_{LA}\tau \sim 500 - 600$ nm best explains

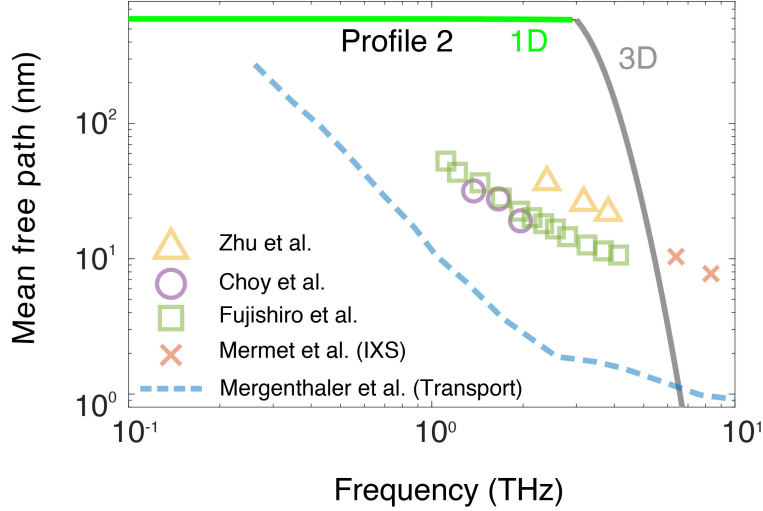


Figure 4.16: Mean free path profile of LA phonons that are compatible with our thermal data along with the literature data. Solid line is mean free path profile 2 discussed in the main text. Profile 2 is with 1D DOS and 3D DOS. For the calculation of low energy Debye model using profile 2, 3D DOS was used above 3 THz, below which 1D DOS was used. Symbols are the literature data from thermal characterizations using dominant LA phonon approximation (upward-pointing triangles, crystallinity 83%, Ref. [141]; circles, crystallinity 73%, Ref. [139]; squares, DR150, Ref. [142]; dashed line, crystallinity 77%, Ref. [140]) and IXS, DR5.5, Ref. [26]. The prior data provided constraints for our modeling.

the thermal conductivity versus the grating period. We first consider the calculation based on $\Lambda(\omega) = v_{LA}\tau \sim 500 - 600$ nm using ab-initio predicted 3D DOS for frequency 0 - 1.5 THz. As shown in Fig. 4.17A, the calculated thermal conductivity versus the temperature at $L = 9.8 \mu\text{m}$ agrees with our measurement up to around 100 K, below which a significant deviation was observed. Corresponding calculated thermal conductivity versus the grating period is shown in Fig. 4.17B-E, with which we found a disagreement at 30 K.

Therefore, we used profile 2 in Fig. 4.16 with 1D DOS ($= 1/\pi v_{LA}\pi r^2$) below ~ 2.9 THz, above which we used ab-initio predicted 3D DOS. The r is the radius of the extended PE crystal, which we assume 10 nm, following Ref. [119, 119, 120, 120, 124–127, 127]. For this calculation, 3D DOS was used for frequency above 3 THz. The calculated thermal conductivity at $9.8 \mu\text{m}$ using profile 2 excellently agrees with our measurements as shown in Fig. 4.17A. Furthermore, corresponding thermal conductivity versus the grating period is compatible with the data as shown in Figs. 4.17B-E.

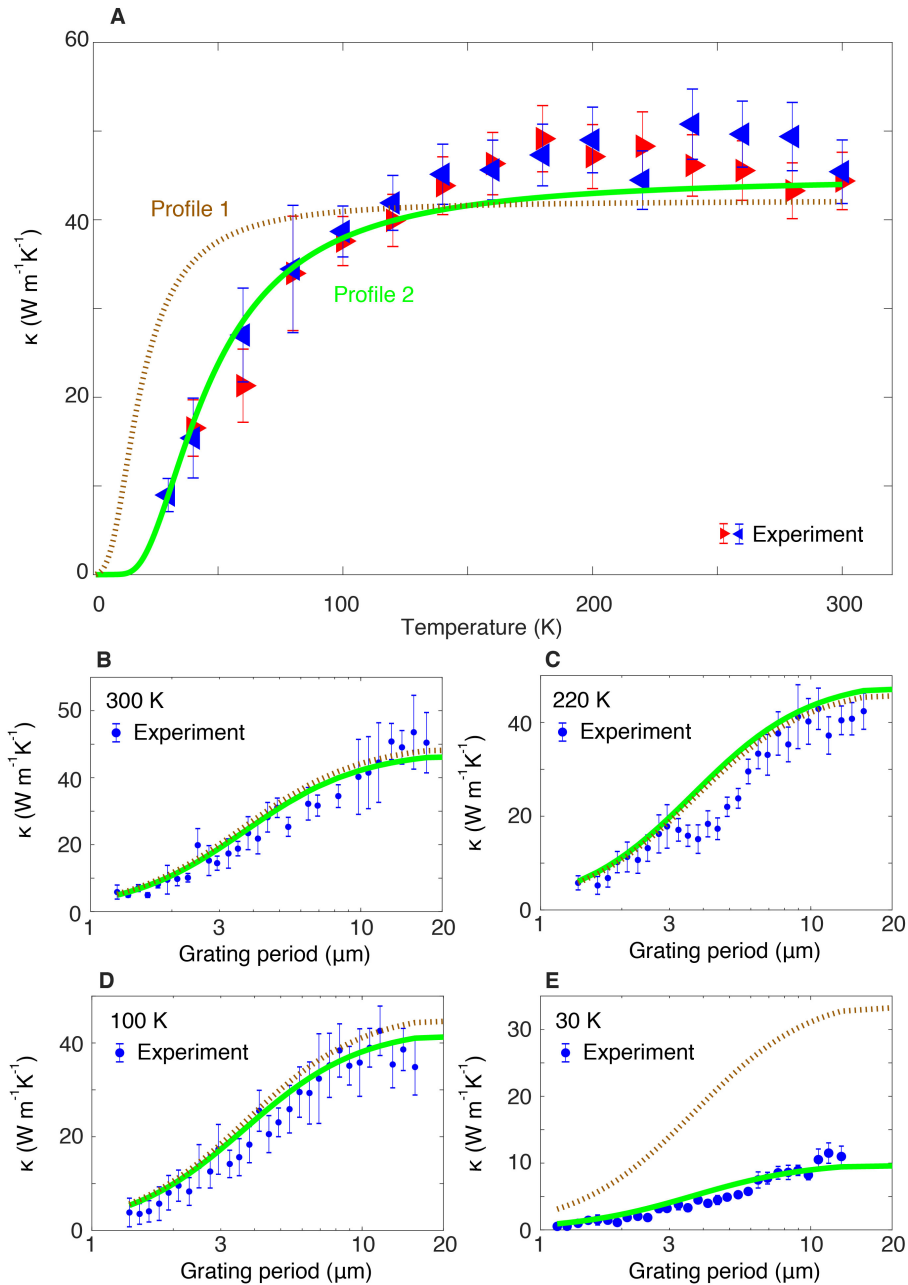


Figure 4.17: Calculation of the thermal conductivity based on profiles 1 and 2. (A) Thermal conductivity versus the temperature $L = 9.8 \mu m$. While the calculation from profile 2 excellently agrees with the data, that from profile 1 deviates from the data below 100 K. Calculated thermal conductivity versus the grating period at (B) 300 K, (C) 220 K, (D) 100 K, and (E) 30 K along with the measurements. The calculated thermal conductivity from profile 1 at 30 K is overestimated at all grating periods.

The above results imply the presence of the 1D transport of the phonons in highly

oriented PE. Based on our observation, we applied similar analysis to prior measurements on partially oriented PE (DR7.5) in Ref. [37]. Under the same constraints, we found that the frequency dependent mean free path, $\Lambda(\omega) = v_{LA}\tau \sim 80$ nm best explains the thermal conductivity versus the grating for DR8. Based on these, we considered profile 1 (3D DOS for 0 - 2 THz), profile 2 (1D DOS for 0 - 3.9 THz, 3D DOS for frequency above 3.9 THz). Figure 4.18B-E shows our calculation. We find that only profile 2 provides a calculation that excellently agrees with the data. By comparing crossover frequency, we find ~ 1 THz difference compared to the results from DR196. In fact, the results in Ref. [131] were obtained considering heat capacity of crystalline phases only. In semi-crystalline polymers, it was reported that the heat capacity of the amorphous fraction for temperatures 100 - 300 K is higher than that of crystalline fraction [143], with a maximum difference by a factor of 1.5 - 2 near 250 K. If the heat capacity was considered for measurements in Ref. [131], corresponding low temperature thermal conductivity would increase, indicating that the transition frequency for 1D to 3D would decrease. Therefore, we believe that the 1D to 3D transition frequency exists near 2-3 THz. Further measurements are underway to provide evidence for this claim.

4.8 Discussion

Concerning the polymers, it is of significant importance to understand the microstructure-transport relationship as highlighted in prior studies. Therefore, the results presented in this chapter can be interpreted as follows.

From the results of the grating dependence and reconstructed cumulative thermal conductivity, the corresponding domain size of the extended crystal is comparable to $1 \mu\text{m}$. Since the thermal conductivity lacks of an obvious temperature dependence, it is obvious that the heat-carrying phonons are scattered at the boundary of the extended crystal. If the phonons would be fully diffused scattered at the boundary, corresponding MFPs would be limited by size of the diameter of on order of 10 nm. Considering the frequency resolved MFPs, however, we observe that the MFPs of the phonons are an order of a few hundred nanometer up to around 3 THz, above which the value of MFP is negligibly small, indicating that the low frequency phonons are scattered specularly rather than diffusively.

The specular scattering of low frequency acoustic phonons as a dominant mechanism can be evidenced by comparing the wavelength of the LA phonons to the fiber diameter dimension. At around 2 THz, the wavelength of the LA phonons is an

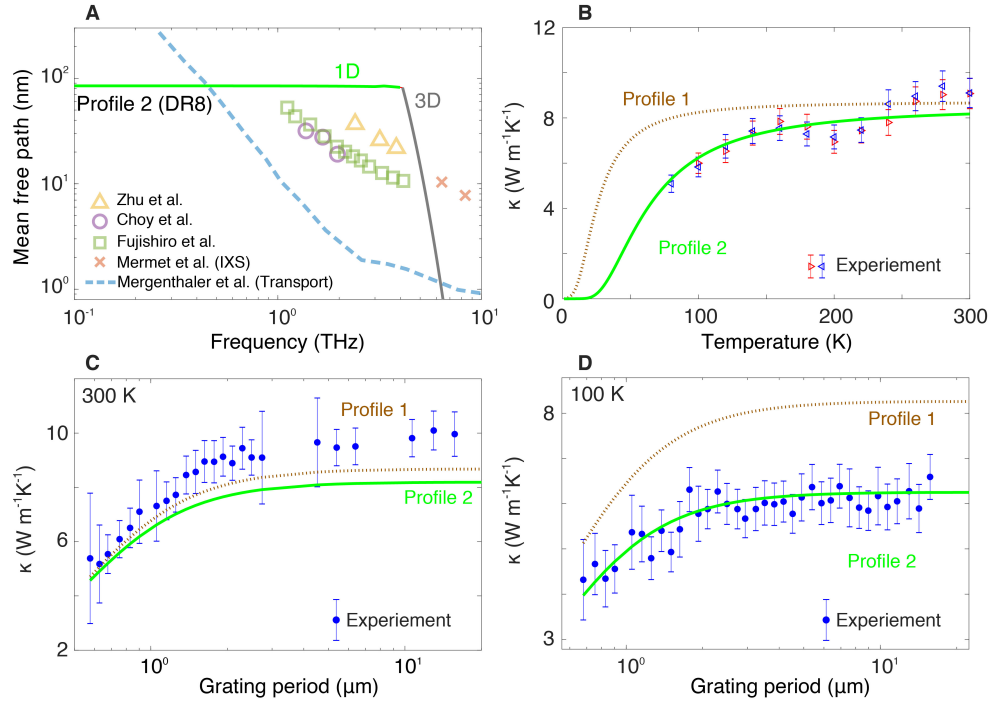


Figure 4.18: Calculation of the phonon transport properties based on literature data of DR7.5 in Ref [37]. (A) Mean free path profile of LA phonons that are compatible with literature thermal data of DR7.5 along with the other literature data of MFPs. Solid line is the profile 2 accounting for 3D and 1D DOS. Symbols are from the literature data mentioned in Fig. 4.16, which provided the constraints. (B) Calculated thermal conductivity at $L = 9.8 \mu\text{m}$. While the calculation from profile 2 excellently agrees with the data, that from profile 1 deviates from the data below 100 K. Calculated thermal conductivity versus the grating period at (C) 300 K, and (D) 100 K along with the experiments is shown. In DR7.5, the calculated thermal conductivity from profile 1 at 100 K is overestimated at all grating periods.

order of 8 nm, which is comparable or greater than the reported radius of the extended fiber (diameter: $\sim 10 \text{ nm}$) from prior studies. According to the theory of the phonon-boundary scattering, it is well-known that the long wavelength phonons are more likely to scatter specularly, resulting in a coherent thermal conduction in PE. More precisely, since the group velocity of the acoustic phonons in PE are as high as 17000 m s^{-1} , the phonons propagate coherently over the micron length scale with its reduced density. Therefore, we attribute our observation to one-dimensional coherent thermal conduction within the extended fibers, as an origin of actual thermally conductive polymers.

However, the presented results here are different from prior predictions on the thermal transport in thermally conductive polymers. First, limited computational

domain size in ab-initio calculation hinders the accurate prediction of the transport of the low frequency phonons that are known to provide a non-negligible contribution to the heat. Second, as mentioned earlier, the understanding of the thermal transport properties in PE has been limited only in a perfect micro-structures (a repeated coil structure), which is far from actual substances. The discrepancy between these predictions and experiments highlights that the understanding correlation between the local domain arrangements and heat-carrying acoustic phonon scattering is important, and that this should be addressed under the consideration of the phonon transport that is subject to the realistic structure.

4.9 Summary

In conclusion, we have applied TG to study the origin of the actual thermally conductive polymers. The mean free paths exceed those in samples of lesser draw ratio by an order of magnitude, indicating that the high thermal conductivity of the present samples primarily arises from decreased structural scattering in the crystalline phase. The decreased structural scattering in turn could arise from larger crystalline domains as well as higher transmissivity across crystalline-amorphous boundaries in the highly aligned samples. We find evidence of one-dimensional density states of phonons with a frequency less than 2THz. The transition frequency is consistent with prior observations in the highly oriented PE; stiff longitudinal branch with LA group velocity $\sim 17000 \text{ ms}^{-1}$ makes LA phonons to have a wavelength of 8 nm, which is comparable to a fiber diameter of 10nm. Therefore, the wavelength of low-frequency heat-carrying acoustic phonons exceed fiber diameter dimensions. These observations improve the understanding of microscopic transport properties of heat-carrying acoustic phonons in highly oriented polyethylenes. Our results, in turn, will improve the understanding of the actual upper-limit of thermally conductive polymers, which will be useful for next-generation low-weight and cost-effective thermal management materials.

ORIGIN OF ACOUSTIC EXCITATIONS IN AMORPHOUS SILICON

This chapter has been adapted, in part, from:

Taeyong Kim, Jaeyun Moon, and Austin J. Minnich. Origin of micron-scale propagation lengths of heat-carrying acoustic excitations in amorphous silicon. July 2020. URL <https://arxiv.org/abs/2007.15777v1>.

T.K. participated in the conception of the project, prepared the experimental data, analyzed the results, and participated in the writing of the manuscript.

So far, we have applied TG to study microscopic thermal transport properties in solids containing crystalline phases. In this chapter, we further expand the application scope of the TG by applying the technique to amorphous silicon.

5.1 Motivation

The collective acoustic excitations of amorphous solids are of fundamental interest due to their anomalous properties compared to those of crystalline solids, including an excess heat capacity at cryogenic temperatures [144, 145] and damping by two-level systems [146–150]. The dispersion and damping of acoustic excitations responsible for heat transport have been extensively explored in many glasses using experimental methods such as inelastic scattering [28, 151–155], tunnel junction spectroscopy [156], Brillouin scattering [157–159], and picosecond acoustics [160, 161], among others. These studies have generally found that excitations with well-defined frequency and wave vectors are supported up to ~ 1 THz. In vitreous silica, a relative of amorphous silicon (aSi), the attenuation exhibits several different regimes, yielding different power-law frequency dependencies. For frequencies below ~ 600 GHz, the damping scales as ω^{-2} corresponding to anharmonic damping and thermally activated two-level system relaxation. Between 600 GHz and 1 THz, a Rayleigh scattering trend of ω^{-4} is observed, followed by a return to ω^{-2} scaling [28]. At still higher frequencies, Kittel proposed that attenuation is independent of frequency if the wavelength is comparable to the interatomic length scale [17]. Considering these different regimes, the general trend of MFP versus frequency of

acoustic excitations in glasses has been presented in Fig. 7 of Ref. [162] and Fig. 3 of Ref. [163], among others [18, 164].

Amorphous silicon is an anomalous glass for several reasons. First, at ultrasonic frequencies, attenuation by two-level systems is observed in vitreous silica but not in aSi, suggesting a low density of these systems in aSi [12, 165]. Second, thermal transport measurements indicate that the thermal conductivity of aSi can be higher than those of most glasses [166–169] and that heat-carrying acoustic excitations travel distances on the order of one micron at room temperature despite the atomic disorder [11, 169, 170]. This value is far larger than a few nanometer value inferred for vitreous silica at room temperature [18, 163].

Experimentally resolving the attenuation coefficients by frequency in the sub-THz frequency band would help to understand the origin of these properties, but probing acoustic excitations in this regime is a long-standing experimental challenge. Amorphous silicon is synthesized in small volumes as a thin film of at most a few microns, precluding the use of high-resolution inelastic neutron scattering. Even if sufficient volumes were available, kinematic constraints complicate the measurement of the dispersion and broadening of low energy excitations. While inelastic x-ray scattering has been successfully applied to study THz excitations in aSi [151], the energy resolution is not sufficient to resolve sub-THz excitations. Picosecond acoustics and Brillouin scattering are generally unable to access frequencies above ~ 100 GHz, while tunnel junction spectroscopy and cryogenic thermal conductivity measurements require films with a thickness of several millimeters.

As a result, studies of the acoustic excitations in aSi have relied on numerical simulations based on normal mode analysis. Feldman and Allen classified the excitations in aSi as propagons, diffusons, and locons according to the qualities of the normal mode eigenvectors [14]. Fabian and Allen computed anharmonic decay rates of the normal modes of aSi, predicting that they should exhibit a clear temperature dependence [16]. Other molecular dynamics simulations based on normal mode analysis have predicted that the MFPs decrease as ω^{-2} with increasing frequency for excitations of a few THz frequency, leading to the conclusion that they are damped by anharmonicity [171, 172]. However, some of these predictions are not supported by experiment. For instance, the predicted temperature dependence of THz excitations in Ref. [16] is not observed experimentally using inelastic x-ray scattering [151]. In the hypersonic frequency band ~ 100 GHz, the measured values of attenuation are lower than those predicted by anharmonic damping [15].

An experimental approach to measure the damping of sub-THz phonons versus frequency and thereby resolve this discrepancy is needed. For solids like aSi with MFPs in the micron range, transient grating (TG) is a tabletop experimental method that is capable of measuring the MFP accumulation function, or the cumulative thermal conductivity distribution versus MFP [36, 37, 173]. The technique relies on observations of non-diffusive thermal transport to constrain this function; knowledge of the acoustic dispersion of the solid then provides the MFP versus frequency. In the case of amorphous silicon, the dispersion is known and isotropic [151, 174], simplifying the analysis further. Combined with picosecond acoustics and inelastic x-ray scattering for the low and high frequency limits of the attenuation coefficient, respectively, TG measurements could constrain the frequency dependence of the damping in the sub-THz frequency band and thus resolve the discrepancy.

5.2 Anomalous thermal properties observed in amorphous materials

As briefly described in 5.1, many amorphous materials possess universal anomalies that are absent in crystals: thermal conductivity, heat capacity, and the acoustic attenuation. In this section, we present experimental observations that were made for such anomalies.

Thermal conductivity of amorphous materials

Figure 5.1A shows the thermal conductivity of SiO₂ both in crystalline and amorphous forms. The thermal conductivity in α -Quartz increases as the temperature decreases above 10 K, below which the value decreases; the temperature dependence is attributed to phonon-phonon scattering followed by characteristic boundary scattering. On the other hand, the thermal conductivity of vitreous silica monotonically decreases with a decreasing temperature with smaller values compared to that in α -Quartz. For instance, the thermal conductivity of vitreous silica at room temperature is $\sim 1.3 \text{ Wm}^{-1}\text{K}^{-1}$, a value lower by factor of ~ 6 compared to that of α -Quartz. The reported thermal conductivities versus the temperature from glassy substances are shown in Fig. 5.1B. Both the thermal conductivity and its trend of the temperature dependencies are similar both qualitatively and quantitatively, which was supported by other earlier works on many glasses [175, 176].

Excess heat capacity

Another unique feature is excess heat capacities at low temperatures in amorphous materials [18, 148, 179, 180]. At low temperatures, according to the Debye theory,

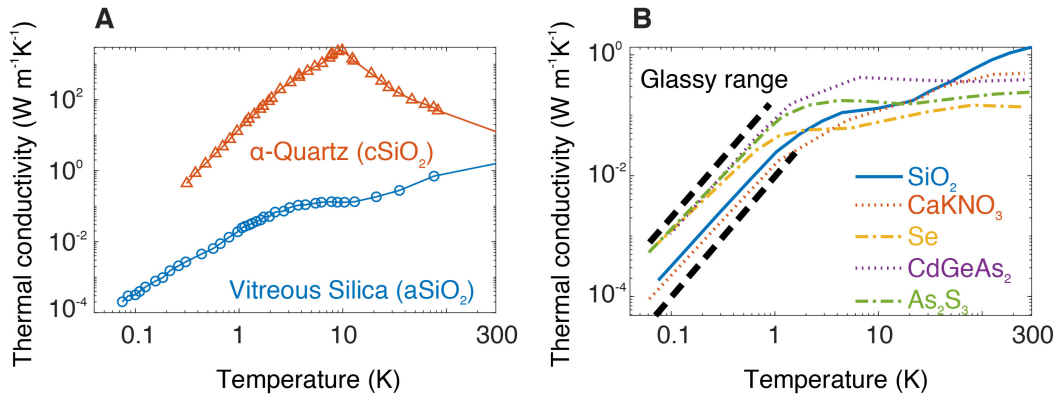


Figure 5.1: (A) The thermal conductivity versus the temperature for α -Quartz (crystalline SiO_2) and for vitreous silica (amorphous SiO_2) in Ref. [18]. The thermal conductivity in α -Quartz increases as the temperature decreases above 10 K, below which the value decreases. With decreasing temperature, the increasing trend is due to reduced phonon-phonon scattering whereas the decreasing trend is due to phonon boundary scattering. In vitreous silica, the thermal conductivity monotonically decreases with decreasing temperature with values smaller typically more than one order of magnitude compared to that in α -Quartz. (B) The thermal conductivity versus the temperature for several amorphous materials in Ref. [177]. All the glassy materials show that the trend of the thermal conductivity monotonically decreases with decreasing temperature. The black dashed line indicates glassy-range below 1 K in Ref. [178], indicating that the reported values below 1K are within this range.

the specific heat would be proportional to T^3 . The theory had been considered to be applicable on any solid, since the wavelength of the dominant heat-carrying vibrations would far exceed the characteristic length of disorder. However, experimental evidences indicate that the heat capacities in amorphous solids at low temperatures deviate from the Debye prediction. Figure 5.2 shows literature data of low temperature heat capacities of some glassy substances. In silica, measured heat capacity far exceeds the Debye calculation of the heat capacity with its linear dependence of the temperature as shown in Fig. 5.2A. The presence of the excess heat capacities with its linear temperature dependence is evidenced in other glassy materials such as Se and Cer-Vit as shown in Fig. 5.2. To explain the linear temperature dependence of the heat capacity, earlier works have proposed a model assuming the existence of two level states with a constant density of states [149].

Damping of acoustic excitations in amorphous materials

Figure 5.3 shows the literature data of MFP versus the frequency for heat-carrying vibrations in vitreous silica in Ref. [163]. As suggested by other earlier works on

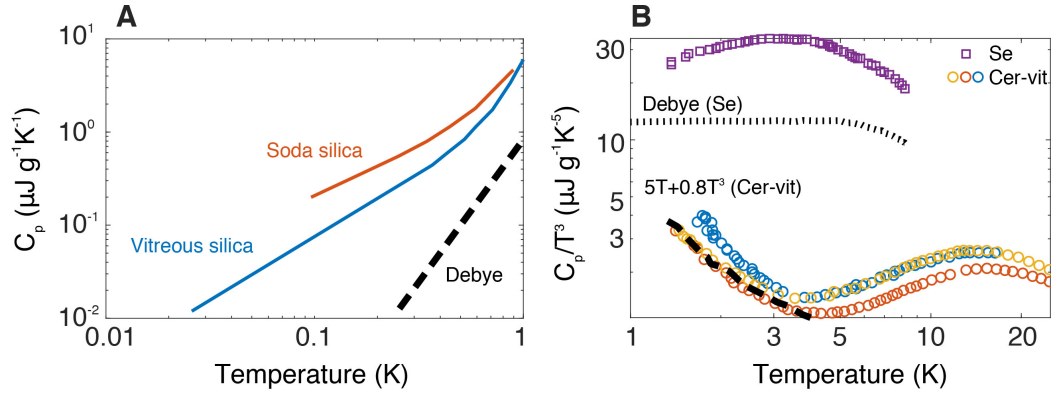


Figure 5.2: Literature data of low temperature heat capacities of several amorphous materials. (A) Heat capacity of SiO_2 versus the temperature below 1 K [148]. Below 1 K, the heat capacity is approximately linearly proportional to the temperature. Observed heat capacity exceeds the Debye specific heat of vitreous silica (dashed line). (B) Scaled heat capacity versus the temperature for Se [179] and Cer-vit [180]. Shown is the heat capacity divided by T^3 . Peak of the heat capacity is observed at ~ 5 K (~ 15 K) for Se (Cer-Vit). The heat capacity of Se exceeds the calculation using the Debye prediction (dotted line). For Cer-Vit, the heat capacity demonstrates a temperature dependence below 4 K with a best fit of $5T + 0.8T^3$ (dashed line), indicating a deviation from the Debye prediction.

amorphous materials [149, 181, 182], it is considered that there are three different frequency dependent regimes in amorphous materials. At the high frequency regime, the MFP is nearly independent of the temperature with a value less than 1 nm, due to the strong scattering by atomic disorder. As the frequency decreases, the MFP exhibits a rapid increase with a frequency dependence $\Lambda \propto \omega^{-4}$, analogous to Rayleigh scattering of the phonons and photons. In this frequency range, prior literature concluded that the wavelength is sufficiently longer than the disorder length scale, yielding a Rayleigh-type trend of the scattering. At very low frequencies, for example $\omega < 0.01\omega_D$ in Fig. 5.3, the frequency dependence becomes weaker with $\Lambda \propto \omega^{-2}$. For these frequencies, it is discussed that the excitations are damped by structural relaxation of two level systems, an asymmetric double-well potential induced by the impurities [146, 183].

Figure 5.4 shows the internal friction of several amorphous materials versus the temperature measured using torsional oscillator [184]. Here the internal friction is proportional to the ratio of the attenuation coefficient to the frequency of kHz acoustic excitations. With a decreasing temperature, the magnitude of the acoustic damping in glassy substances decreases above 100 - 300 K, below which that

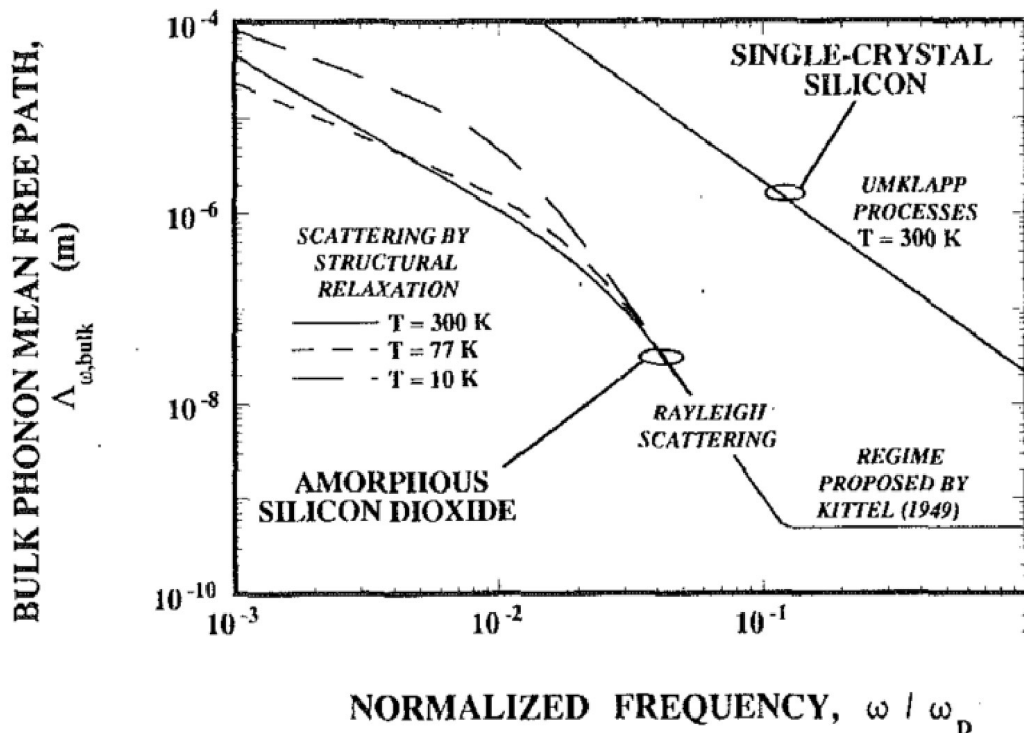


Figure 5.3: The mean free path of vibration (Λ) versus the frequency normalized by ω_D in vitreous silica in Ref. [163]. From high frequency above $0.1\omega_D$, the MFP is order of sub-nm with independence of the frequency due to atomic disorder. Below $0.1\omega_D$, a Rayleigh-type trend of the MFP ($\Lambda \propto \omega^{-4}$) is observed up to $\omega = 0.04\omega_D$, below which Λ is proportional to ω^{-2} , indicating different scattering mechanisms of the acoustic excitation. $\Lambda \propto \omega^{-2}$ is due to the damping via structural relaxation by two-level system.

increases. In this temperature range, the damping of the vibration is highly dependent on the frequency [148] and the chemical composition [184]. As in Fig. 5.4, for instance, the attenuation of ~ 100 kHz vibrations reaches its minimum at ~ 300 K, which increases up to ~ 100 K for sub-kHz vibrations. Below 100 - 300 K, as the temperature decreases, the magnitude of the damping again decreases with lesser apparent temperature dependence compared to the higher temperature range as shown in 5.4. At these temperatures, the damping is known to be independent of the chemical composition; it was reported that the magnitude of the damping falls into similar values, is separated by less than a factor of 20 as indicated by the glassy range as shown in Fig.5.4. The trend of the constant magnitude of the acoustic damping continues up to ~ 1 K, below which the damping again possesses temperature and frequency dependence.

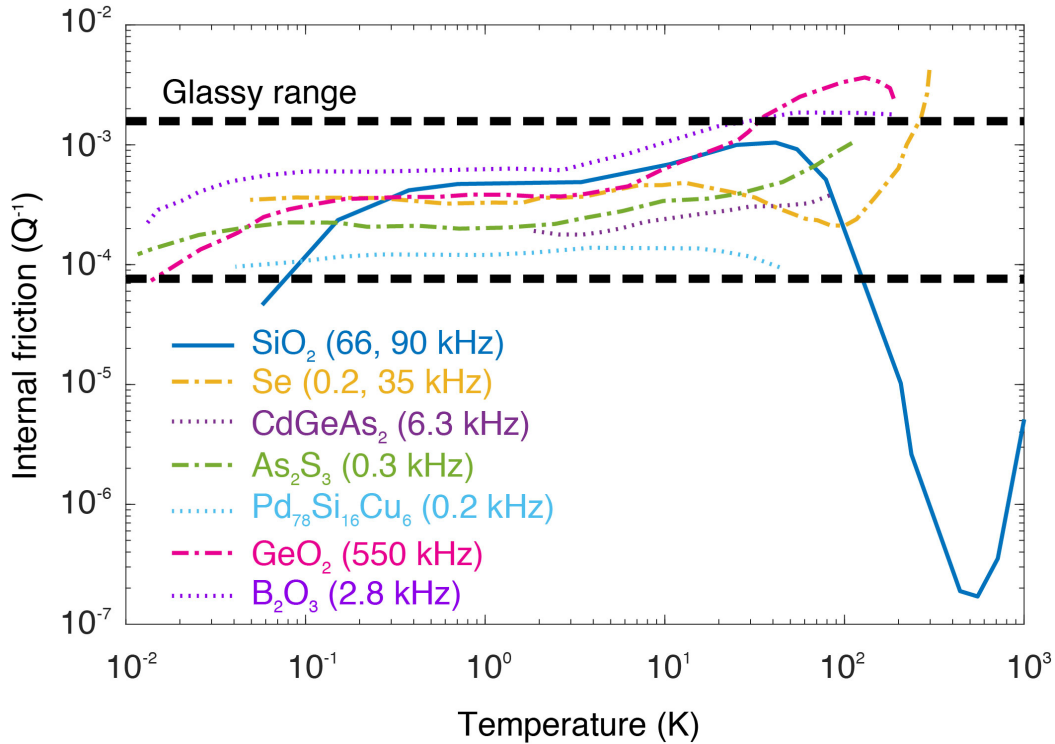


Figure 5.4: The internal friction versus the temperature for several glassy materials in Ref. [184]. The internal friction (Q^{-1}) is defined by $\nu\alpha/\omega$, where ν is the sound velocity, ω is the acoustic frequency, and the α is the attenuation coefficient [178]. At a high temperature up to 100 - 300 K, the internal friction exhibits a clear temperature dependence, which varies depending on the chemical composition. Below 100 - 300 K, as the temperature decreases, hence the internal friction decreases with weaker temperature dependence. The values of the internal friction in this temperature range for amorphous materials are reported to fall into similar values, separated within a factor of 20 as indicated by the glassy range (dashed line) [178]. For temperatures less than 1 K, the temperature dependence of the internal friction again shows marked temperature dependence.

Several empirical models have been proposed to explain the anomalies mentioned above. The minimum thermal conductivity model was employed to explain the thermal transport amorphous materials [185, 186]. The two level system (TLS) was developed to explain both the anomalies of the excess heat capacity and the damping mechanism in amorphous materials [146, 149, 183].

5.3 Prior empirical models

As discussed in 5.1, several empirical models have been proposed to explain the anomalies present in amorphous materials. In this section, we briefly discuss

previous descriptions.

Minimum thermal conductivity

The minimum thermal conductivity is one of the empirical approaches to explain the thermal transport in glassy substances. The proof of concept was proposed by Einstein [187], and the theory was applied to glasses by Cahill [185, 186]. The minimum thermal conductivity assumes the heat transfer process as a random walk of the heat energy. The minimum thermal conductivity assumes that the atomic vibrations oscillate near the equilibrium point and that they have an incoherent phase. Corresponding distance resulting from the random walk is $\Lambda = \pi/\omega$ which gives the expression for the lower limit to the thermal conductivity

$$\kappa_{min} = \left(\frac{\pi}{6}\right)^{1/3} k_B n^{2/3} \sum_i v_i \left(\frac{T}{\theta_i}\right)^2 \int_0^{\theta_i/T} \frac{x^3 e^x}{(e^x - 1)^2} dx \quad (5.1)$$

where θ_i is the Debye temperature, and n is the number density. It was discussed that this theory is not applicable to the crystals, since periodic arrangements of the atoms are known to produce a coherence between the vibrations [186]. On the other hand, Ref. [186] demonstrated that the prediction from the minimum thermal conductivity agrees with experimental observations in amorphous materials.

However, the applicability of this theory should be re-examined. In fact, the minimum thermal conductivity is not favorable for explaining the transport of the low energy excitations. First, analogous to acoustic phonons in crystals, the wavelength of the low energy excitations is relatively long, indicating that the excitations propagate collectively rather than randomly diffuse within disordered length scales. Second, the frequency dependent transport properties are missing in the minimum thermal conductivity theory. Vibrations in solids are dispersive and corresponding transport properties are different depending on the frequency. Therefore, if the mechanism of the damping of the excitations would be different at higher frequencies, the corresponding frequency dependence of the MFP should be different, which the minimum thermal conductivity model cannot precisely capture.

Two-level system (TLS)

Earlier works have described the linear temperature dependence of the heat capacity by the two-level system (TLS) damping of the low energy excitations, initially proposed by Anderson, Halperin, and Varma [149]. According to this model, the damping of the acoustic excitation is due to resonant absorption at very low temperatures (typically less than 5 K), above which is due to thermally activated relaxation

[146, 183]. In the following, we briefly describe the frequency dependence of the MFP induced by resonant absorption.

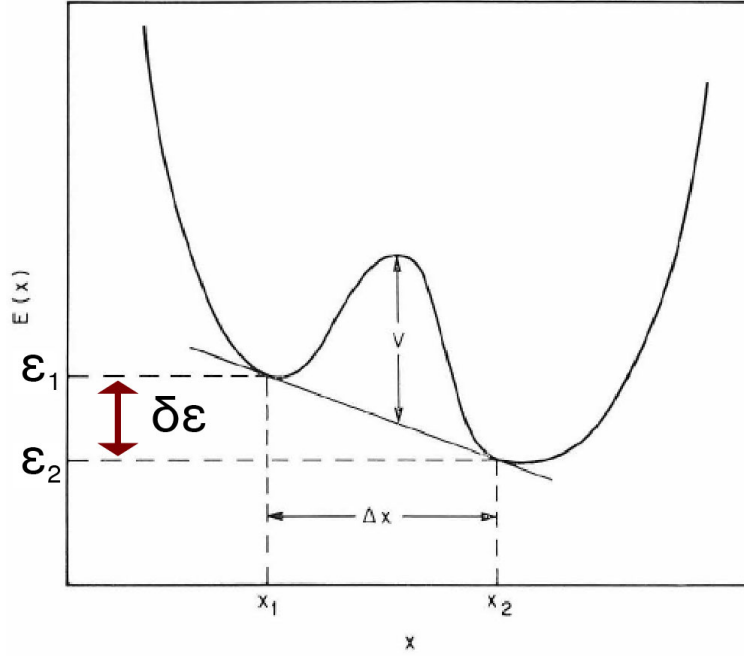


Figure 5.5: Asymmetric potential well versus the position proposed by Anderson, Halperin, and Varma [149]. The figure was taken from Ref. [149], and modified.

Briefly, this theory assumes that the impurities induce an asymmetric double-well potential system with a constant density as follows

$$C_{TLS} \propto \int (\hbar\omega)n(\omega)d\omega \propto \frac{k_B T}{\hbar} \quad (5.2)$$

The theory of the TLS assumes that the elastic waves near TLS deform the double-well potential, which causes the tunneling of acoustic excitation through the potentials. Here, we describe an earlier mathematical framework proposed by Anderson, Halperin, and Varma [149]. The interaction between local TLS and the phonon can be described by the first-order perturbation theory where the Hamiltonian can be described by

$$H = H_0 + H_1 = \frac{1}{2} \begin{pmatrix} \epsilon_1 & \Delta \\ \Delta & \epsilon_2 \end{pmatrix} + \begin{pmatrix} \delta\epsilon & 0 \\ 0 & \delta\epsilon \end{pmatrix} \quad (5.3)$$

where the ϵ_1 (ϵ_2) is the local minima of the asymmetric potential, $\delta\epsilon$ is the deformation potential, and Δ is the zero-point energy due to the overlap of the wavefunction at the local minima. The mean free path of the acoustic excitation for $\hbar\omega > k_B T$

$$\Lambda(\omega) = (\sigma\langle\tau^{-1}\rangle)^{-1} \quad (5.4)$$

where $\sigma = 4\pi v^2 \omega^2$ is the scattering cross section, and $\langle \tau^{-1} \rangle$ is the ensemble averaged transition rate between the eigenstates of the matrix above. Applying a Fermi-golden rule under an approximation of $\hbar\omega = \epsilon_1^2 + \epsilon_2^2$ (resonant absorption), the transition rate is given by

$$\tau^{-1} = \frac{3\pi B^2}{mv^2} \left(\frac{\omega}{\omega_D^3} \right) \frac{\Delta^2}{\hbar} \quad (5.5)$$

$$\langle \tau^{-1} \rangle = \int [p(\epsilon_1 - \epsilon_2; \Delta; B) \tau^{-1}] dB d\Delta d(\epsilon_1 - \epsilon_2) \quad (5.6)$$

where p is the probability distribution over ensemble of levels, and B is the differences in the constants for the deformation potential. Corresponding MFP can be simplified to

$$\Lambda \propto \frac{1}{v^2} \omega^{-1} \quad (5.7)$$

Finally, considering the temperature dependence, an empirical factor was added such that

$$\Lambda_{res} \propto \frac{1}{v^2} \omega^{-1} \coth \left(\frac{\hbar\omega}{2k_B T} \right) \quad (5.8)$$

where Λ_{res} is the MFP due to resonant absorption. For $\omega \ll k_B T / \hbar$, Eq. 5.8 can be simplified to $l \approx \omega^2 / T$ for $\omega \ll k_B T / \hbar$. The theory of the TLS has shown excellent agreement with the low-temperature thermal conductivity as well as the attenuation of the low frequency excitations below a few K [148].

Density fluctuation

The density fluctuation is based on the structural inhomogeneity as a primary mechanism for the scattering of the acoustic excitations [182]. The model considers free excess sub-volumes in an amorphous structure [188]. The re-distribution of the sub-volumes would occur, resulting in the local density deviating from the average density. The local density deviation becomes a scattering cross-section for the excitations, similar to point defect phonon scattering. Here, we briefly describe the frequency dependence shown in Ref. [182].

We consider a sub-volume v with a different density (ρ) in an amorphous structure. The corresponding scattering cross-section for an acoustic excitation is given by

$$\sigma_1 \approx \frac{1}{12\pi} q^4 v^2 \left(\frac{\Delta\rho}{\rho} \right)^2 \quad (qv^{1/3} < 1) \quad (5.9)$$

$$\sigma_2 \approx v^{-1/3} \left(\frac{\Delta\rho}{\rho} \right)^2 \quad (qv^{1/3} > 1) \quad (5.10)$$

where q is the wave vector of the acoustic excitation, and ρ is the density deviation. The above expression is analogous to the scattering cross-section for Rayleigh scattering and geometric scattering, respectively.

First, considering a short wave vector excitations, the corresponding mean free path of the excitation from Eq. 5.9 is

$$\Lambda_1^{-1} = \sum_{\Delta\rho} P(\Delta\rho) \frac{1}{12\pi} q^4 v^2 \left(\frac{\Delta\rho}{\rho}\right)^2 = \frac{1}{12\pi} q^4 v^2 \overline{\frac{\Delta\rho^2}{\rho^2}} \quad (5.11)$$

$$\overline{\frac{\Delta\rho^2}{\rho^2}} = \frac{Vp}{vN(1-p)} \quad (5.12)$$

where P is the probability of the given density fluctuation, $\overline{\Delta\rho^2}$ is the mean square deviation of the density, $\overline{\rho^2}$ is the average density, N is the number of the sub-volumes, and (p) is the probability for density deviation. For the volumes from v to $v + dv$, using Eq. 5.12 and Eq. 5.11, the corresponding MFP of the excitation is given by

$$\Lambda_1^{-1} = \frac{q^4}{12\pi} \frac{p}{1-p} dv \quad (5.13)$$

which yields $\Lambda^{-1} \propto q^4$ for short wave vector limit.

Similarly, for $qa > 1$,

$$\Lambda_2^{-1} = \sum_{\Delta\rho} P(\Delta\rho) \sigma_2 \approx v^{-4/3} \frac{p}{1-p} dv \quad (5.14)$$

The integration over dv gives an expression for the MFP

$$\Lambda^{-1} = \int_v [\Lambda_1^{-1}(v, q) + \Lambda_2^{-1}(v, q)] dv \propto q \quad (5.15)$$

The above expression for the MFP can be re-written as the MFP versus the frequency at different frequency range

$$\Lambda \propto \omega^{-4} \quad (5.16)$$

for high frequency, whereas for low frequency,

$$\Lambda \propto \omega^{-1} \quad (5.17)$$

The density fluctuation theory has shown a good agreement with the thermal conductivity data [18, 182], provided that the information of the density deviation is well-defined. However, the theory may not be applicable to the damping of the excitation below 1 K, since the extremely large length scale of the fluctuation is required for explaining the damping at very low temperatures.

5.4 Picosecond sound acoustics (PSA) on aSi

Having discussed the transport of heat-carrying acoustic excitations in amorphous materials, we now present our novel approach for measuring frequency resolved MFPs of acoustic excitations in amorphous silicon. We first describe the measurements of 100 GHz excitation using the picosecond acoustics. Then we describe a table-top approach to measure the MFP over the frequency range from $\sim 0.1 - 3$ THz.

Background

Here, we present a pump-probe scheme used for measuring the damping of the ~ 100 GHz excitations in aSi. The attenuation coefficient of hypersonic waves in aSi films on sapphire substrates was measured using picosecond acoustics (PSA). The PSA was developed to generate and detect wave packets of the vibration over a wide range of the frequencies and the temperatures [189]. Such an objective led to a development of an experimental setup with sub-ps temporal resolution. Since the details were discussed in many prior works, here we only briefly discuss the PSA [189]. The principle of the PSA is similar to that of time domain thermoreflectance (TDTR), therefore we prepared a PSA optical system that is identical to TDTR. Briefly, a train of the pulses (repetition rate: 76 MHz, wavelength 785 nm) is split into pump ($1/e^2$ diameter: $13.7 \mu\text{m}$, power: ~ 10 mW) and probe ($1/e^2$ diameter: $12.4 \mu\text{m}$, power: ~ 3 mW) using a two-tint color method [49]. Sharp-edge filter (short pass filter, Semrock inc.) was used to spectrally separate the pump and probe at the wavelength near 785 nm. The pump is amplitude-modulated at 9.2 MHz and focused onto the sample. The pump absorption induces a thermal expansion of a transducer, thermoelastically launching a longitudinal strain pulse.

Considerations in the setup

As in TDTR, it is important to control the beam size in PSA. In PSA, the actual signal is the mixture of the thermal background signal and the acoustic echo signal. Since the magnitude of the acoustic echo signal to that of the thermal background

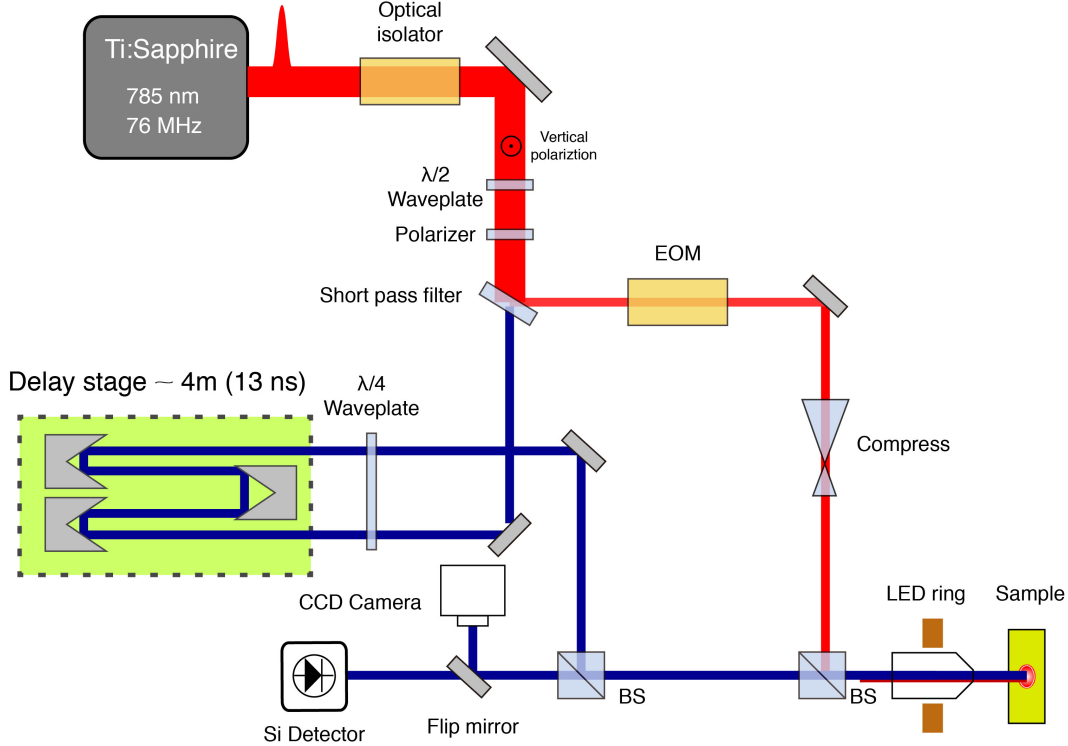


Figure 5.6: Schematic of PSA measurement system in the Minnich lab at Caltech. Pump and probe pulses are spectrally separated at the wavelength near 785 nm, using a sharp-edge short pass filter. Pump pulse train is amplitude-modulated using an electro-optic modulator, and impulsively induces a thermal expansion of a transducer, thermoelastically launching a longitudinal strain wave packet. The probe travels additional 4 m to provide a maximum temporal delay ~ 13 ns with sub-ps temporal resolution. The acoustic strain wave packet is monitored by probe as a transient change of the reflectivity.

is typically less than a few percent, therefore we put our effort to reduce laser spot diameter to be comparable to $10 \mu\text{m}$. The small spot diameter enables to minimize the uncertainties of measurements that may be arisen from the variations in the sample thickness over the laser spot area. For this purposes, we used a 10X objective lens with a working distance of 33.5 mm (10X EO M plan apo, Edmund optics inc.). Next, we discuss the choice of the optimal optical energy and the pump modulation frequency. Considering the measurement system as a linear-time invariant (LTI) system [190], the corresponding thermal transfer function is

$$z(t) = Z(\omega_0) \exp[i\omega_0 t] \quad (5.18)$$

$$Z(\omega_0) \propto Q_{pump} P_{probe} \sum_n H(\omega_0 n) \quad (5.19)$$

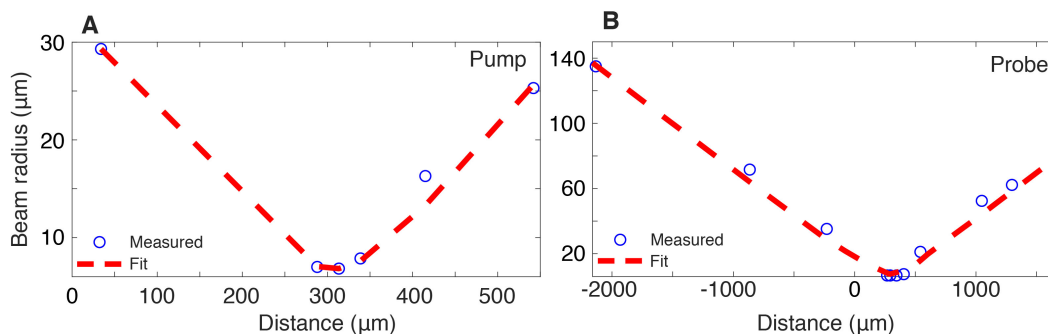


Figure 5.7: Spot radius of (A) pump and (B) probe in PSA setup. The symbols represent the knife-edge measurement and the dashed lines fit. Corresponding spot diameter at the sample position is $13.7 \mu\text{m}$ and $12.4 \mu\text{m}$ for pump and probe, respectively.

where $z(t)$ ($Z(\omega)$) is the thermal response function in the time domain (frequency domain), $\omega_0 = 2\pi f_0$ is the angular modulation frequency, and H is the heat impulse response. From Eq. 5.19, we see important factors which determine the magnitude of the signal. First, the signal is proportional to pump energy and the probe power. Second, since the magnitude of the impulse response becomes smaller as the modulation frequency increases, the corresponding signal magnitude at higher modulation frequency decreases. Therefore, it is necessary to decrease the modulation frequency to increase the signal magnitude. However, it is known that the electronic noise ($1/f$ noise) simultaneously increases as the modulation frequency decreases [190]. Therefore, to maximize both the signal magnitude with ample signal-to-noise ratio (SNR), we systematically change the pump power and the pump modulation frequency. Figure 5.8A and B shows the measured average signal magnitude and corresponding SNR versus pump power from aSi on different substrates. As expected, the signal magnitude increases with increasing pump power, and the corresponding SNR increases up to around 10 mW, above which the value saturates. Figure 5.8C and D shows the signal magnitude and the corresponding SNR versus the pump modulation frequency. We find a substantial increase in SNR at modulation frequency of around 9.2 MHz, while its signal magnitude is relatively smaller than that lower modulation frequency. Considering these observations, a pump power of 10 mW and the modulation frequency of 9.2 MHz were used in our actual experiments.

Lastly, we employed a fast-scanning system with a modification in Lab-view programming. Concerning typical PSA signal traces in aSi, the acoustic echoes that

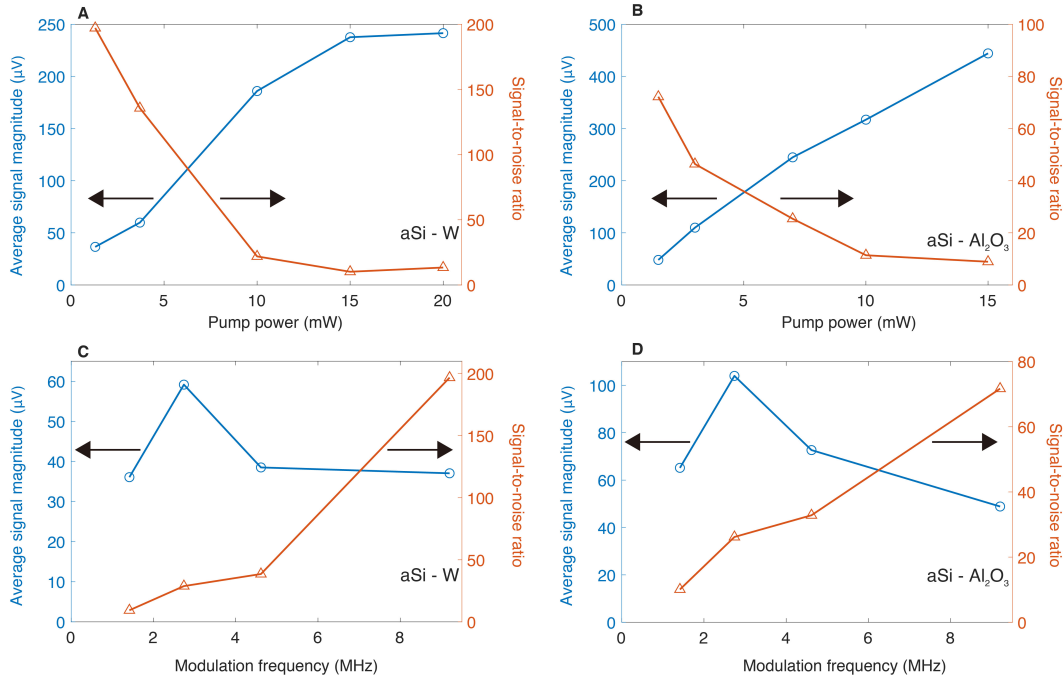


Figure 5.8: Average signal magnitude and corresponding SNR versus the pump power in aSi on (A) Tungsten substrate and (B) Sapphire substrate. While the average signal magnitude increases as the pump power increases, the corresponding value of the SNR saturates at 10 mW. Average signal magnitude and corresponding SNR versus the modulation frequency in aSi on (C) Tungsten substrate and (D) Sapphire substrate. The average signal magnitude decreases at higher modulation frequencies with substantial increase in SNR. The average signal magnitude was obtained from 10 averages. Then the average signal was divided by the subtraction between each signal and the average from which we determined the SNR.

are generated by the strain pulses have a temporal duration less than ~ 40 ps. For a 500 nm thick aSi sample, the temporal separation between each echo is > 100 ps, which increases to ~ 1 ns for a 4 μm thick sample. This means that a huge amount of the data would be unnecessarily acquired for a long time without adjusting the delay step [191]. Therefore, we employed adjustable temporal delay stepping using Labview programming. The adjustable delay stepping is advantageous in that acoustic echoes can be measured with a fine linear time step, while unwanted signal components can be captured using a logarithmic time step. Figure 5.9A shows our Labview designing which enables a sequential linear and logarithmic time stepping. The signal measured using this program is shown in Fig. 5.9B. To describe the signal acquisition shown in Fig. 5.9B, initially, the data were collected with a linear step for time delay ± 20 ps for correcting instrumental phase offset. Acoustic echoes were measured using subsequent linear scans, while other unwanted signal components

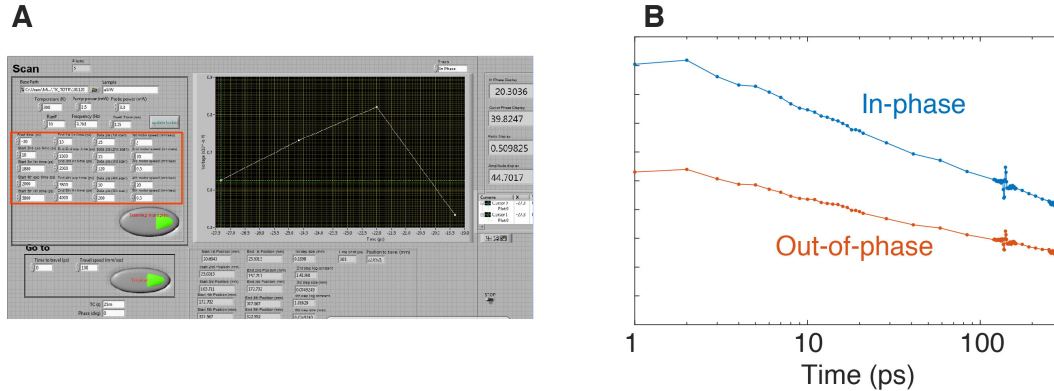


Figure 5.9: (A) Image of PSA data acquisition software (a panel of Labview). The software was programmed to perform linear to logarithmic sequential scanning, therefore enabled to selectively scan acoustic echo signals (highlighted as a red rectangle) (B) Representative signal traces measured in a 500 nm thick aSi sample using the program shown in (A). The data was collected with 1 ps time step for -20 - 20 ps (phase offset part), 125 - 160 ps (1st echo component), 250 - 300 ps (2nd echo component). Unwanted signal components were collected using logarithmic time step with ~ 20 ps spacing.

were collected using logarithmic scans.

PSA sample preparation

To measure the damping of 100 GHz acoustic excitation, we prepared the PSA sample using plasma-enhanced chemical vapor deposition (PECVD) described in Ref. [151]. The aSi film was deposited on a sapphire substrate (University Wafer inc.) and a variable deposition time to prepare three samples with different thicknesses: ~ 500 nm, $\sim 1 \mu\text{m}$, and $\sim 4 \mu\text{m}$. Al with 15 nm was deposited afterwards by electron beam evaporation to serve as a transducer.

PSA measurements and data analysis

The damping of 100 GHz excitation was characterized with the sample prepared with a method in Sec. . A 15 nm Al film was chosen as a transducer to generate an acoustic pulse around $\sim 100 \pm 20$ GHz that propagates through the aSi as in Ref. [15]. The strain pulse experiences multiple reflections between the Al transducer and the sapphire substrate, producing changes in reflectance of the transducer film. Sapphire was chosen as a substrate to enhance the magnitude of the echo signals based on the acoustic mismatch model [15] (for sapphire, $\rho = 3.98 \text{ gcm}^{-3}$, $v_{LA} \sim 11000 \text{ ms}^{-1}$) [192]. The resulting signal is detected using a lock-in amplifier.

The amplitude signal versus the delay time for ~ 500 nm and ~ 4 μm samples are plotted in Figs. 5.10 and 5.11. The resultant magnitude of the signal after one (two) round trip(s) are shown as $\Delta R_1(t)$ ($\Delta R_2(t)$). Following Ref. [15], we analyze the data using Fourier analysis. First, we remove the background signal in $\Delta R_1(t)$ and $\Delta R_2(t)$. Then, $\Delta R_2(t)$ is normalized by the maximum magnitude of $\Delta R_1(t)$. Next, the signals are zero-padded to improve the frequency resolution of the fast Fourier transform (FFT). Finally, the time domain signals are windowed using a Hann window and the FFT is performed.

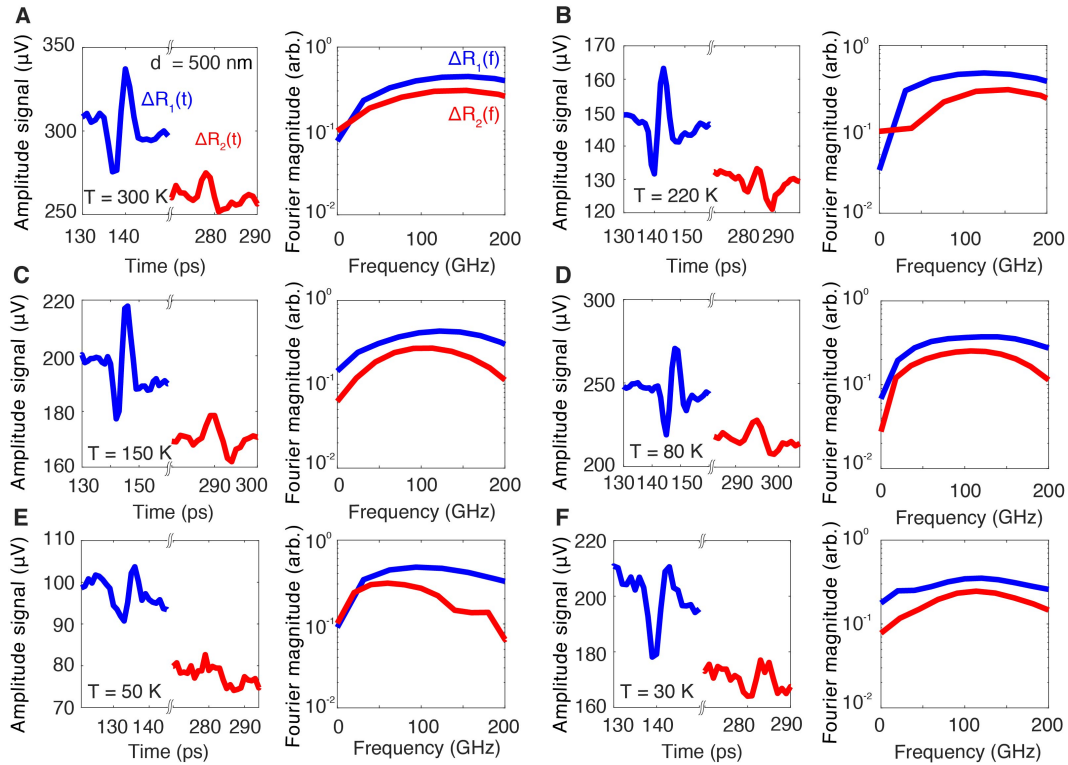


Figure 5.10: (A) (Left) Measured amplitude signal from ~ 500 nm aSi versus delay time using picosecond acoustics at 300 K. The thermal background signals have been removed. Echo 1 occurs at the Al transducer after a round trip between the transducer and the substrate. The echo 2 is the attenuated signal from echo 1 after one more round trip. The thickness of the aSi film was determined from the time difference between the echoes and the known LA sound velocity. (Right) Fast Fourier transform (FFT) magnitude of echo 1 and echo 2 at 300 K. The peak of the FFT for the first echo occurs at ~ 100 GHz, indicating that a 15 nm Al transducer can generate acoustic waves with frequencies ~ 100 GHz as expected. Note that the attenuation for the 500 nm film is due to the reflection or interface loss at the boundary between the aSi and the sapphire. Amplitude signal along with the corresponding magnitude of the Fourier transform measured at (B) 220 K, (C) 150 K, (D) 80 K, (E) 50 K, and (F) 30K.

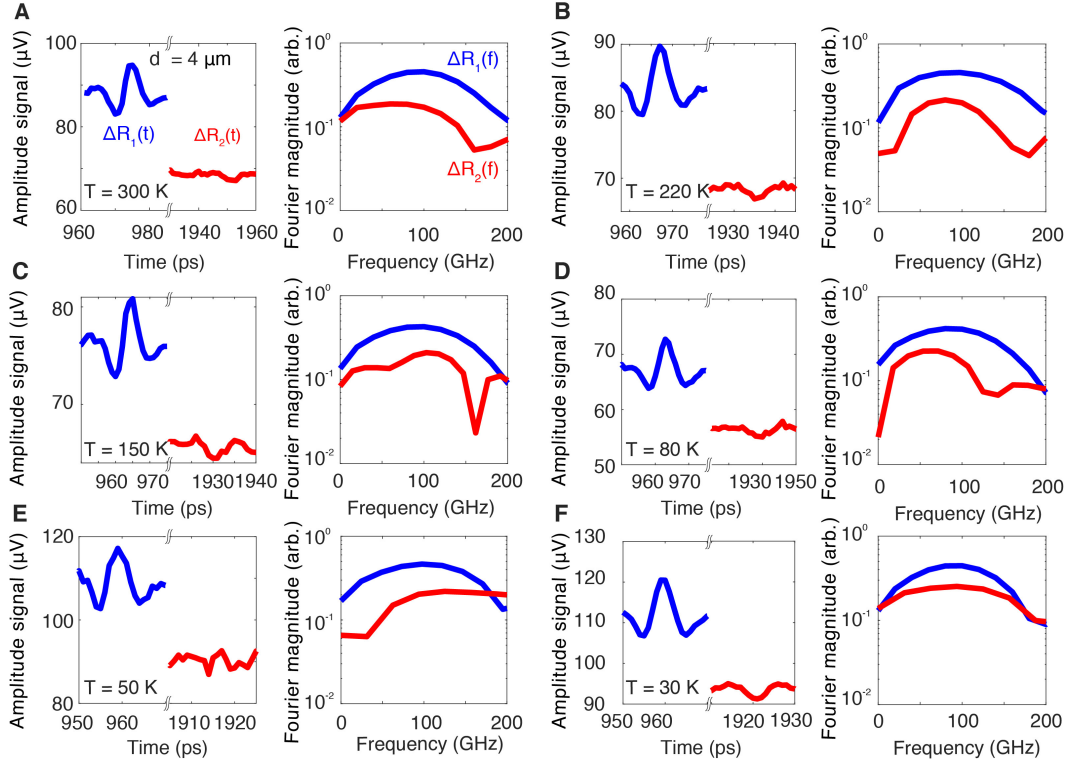


Figure 5.11: (Left) Measured thermorefectance signal from a $4 \mu\text{m}$ sample versus delay time using picosecond acoustics at (A) 300 K, (B) 220 K, (C) 150 K, (D) 80 K, (E) 50 K, and (F) 30 K. The thermal background has been removed. (Right) Magnitude of Fourier transform of echo 1 and echo 2 at the same temperatures.

The resulting Fourier power spectra of each echo is plotted in Figs. 5.10 and 5.11. The peak of the FFT occurs at ~ 100 GHz, indicating that a 15 nm Al transducer can generate acoustic wave with a frequency ~ 100 GHz as expected. As discussed in Ref. [193], the PSA signals consist of wave packets, meaning that the corresponding response is frequency dependent. Therefore, following Ref. [15, 193, 193, 194], rather than treating each Fourier amplitude separately, we compare Fourier amplitude at 100 GHz in Fig. 5.12A. As in Ref. [15], we find that the ratio of the Fourier magnitude at 100 GHz for 500 nm thickness is close to what is predicted by the acoustic mismatch model (AMM) between aSi and the sapphire, $r = (\rho_{\text{sapphire}}v_{\text{sapphire}} - \rho_{\text{aSi}}v_{\text{aSi}})/(\rho_{\text{sapphire}}v_{\text{sapphire}} + \rho_{\text{aSi}}v_{\text{aSi}}) = 0.42 = 2.4^{-1}$, indicating that the loss for 500 nm thickness is dominated by transmission into the sapphire substrate. The attenuation coefficient for 100 GHz vibrations is obtained from

$$\alpha = \frac{1}{d} \ln \left(\frac{r\Delta R_1(\omega)}{\Delta R_2(\omega)} \right) \quad (5.20)$$

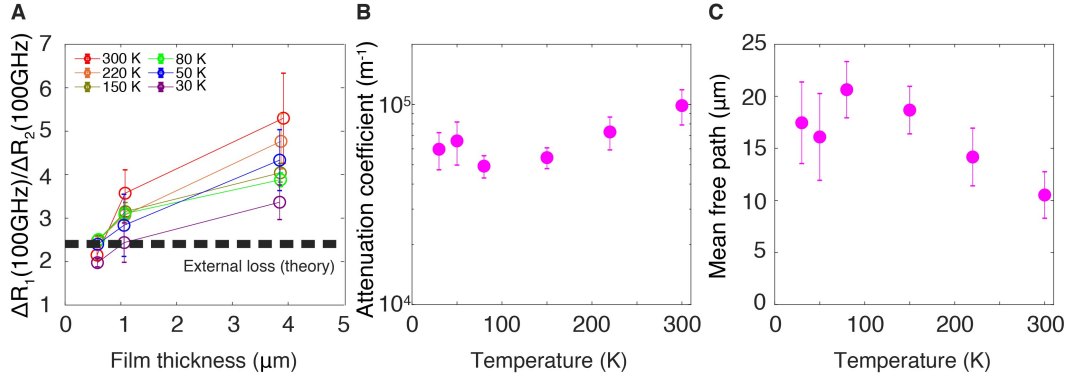


Figure 5.12: (A) Ratio of the Fourier magnitude at 100 GHz measured at temperatures from 30 K to 300 K. The black dashed line indicates the predicted loss at the boundary between aSi and the sapphire from the AMM. Following Ref. [15], external losses were experimentally deduced from the ratio at ~ 500 nm. Internal damping was obtained from the values at $\sim 4 \mu\text{m}$ using Eq. 5.20. The film thicknesses were obtained from the time difference between the echoes. The error bar indicates standard deviation determined from multiple measurements. (B) Attenuation coefficients versus temperature using the 500 nm data for reflection loss and $\sim 4 \mu\text{m}$ data for attenuation. (C) Mean free path versus temperature for the 100 GHz vibrations.

where d is the round trip distance, r is the inverse of the value from 500 nm aSi in Fig. 5.12A, and $\Delta R_1(\omega)/\Delta R_2(\omega)$ is the value from the 4 μm thickness sample in Fig. 5.12A.

The calculated attenuation coefficient is shown in Fig. 5.12B. The measured coefficient is $\sim 10^2 - 10^3 \text{ cm}^{-1}$ with its maximum value at 300 K ($987 \pm 197 \text{ cm}^{-1}$). The measured value at room temperature is close to that reported from PSA in aSi ($780 \pm 160 \text{ cm}^{-1}$) [15], but substantially lower than that of vitreous silica ($\sim 10000 \text{ cm}^{-1}$ at ~ 100 GHz) [195]. Prior studies have reported that fourfold-coordinated covalent bonded material tends to exhibit a weaker damping near 5 kHz which may be the reason for our results. [15, 178]. The mean free path of 100 GHz vibrations versus temperature is shown in Fig. 5.12C. Our measured value is $\sim 10 - 20 \mu\text{m}$ from 30 K ($\sim 17.5 \pm 4 \mu\text{m}$) to 300 K ($\sim 10.5 \pm 2.2 \mu\text{m}$) with a weak temperature dependence.

5.5 Thermal characterization of aSi

In the preceding section, we characterized the damping of the 100 GHz acoustic excitation using PSA. In the following section, we utilize our PSA results to relate it to the thermal transport properties.

Preparation of 500 nm amorphous silicon membrane

We prepared free-standing membrane of aSi using the following method. First, the amorphous silicon was deposited on silicon nitride handle wafer using PECVD with silane gas dilute (5%) in argon gas at a deposition table temperature ~ 473 K [151]. The thickness of the aSi layer was 500 nm. Finally, the handle wafer was dry-etched to create a rectangular aperture with a 1 mm^2 cross-sectional area. A scanning electron microscope image of the sample indicates clean and smooth surface over the membrane area, which is given in Fig. 5.13A.

Self-heating and optical powers

As mentioned in the previous section, care was taken to minimize the steady state and transient temperature rise of the sample while maintaining a signal magnitude of at least 300 - 400 μV . Here, we present an estimation of the steady and transient temperature rises that occurred during the experiment and justify the chosen optical powers.

Estimating the self-heating requires knowledge of the optical absorptance of the sample. We measured temperature-dependent reflectance and transmittance from which we estimated the absorptance of the amorphous silicon film. Table 5.1 shows the measured values at the cryostat temperature (T_c).

T_c (K)	Reflectance (%)	Transmittance (%)	Absorptance (%)
300	39	3	58
210	35	4	62
135	34	5	61
60	32	5	63
40	36	5	59

Table 5.1: Optical properties of aSi measured at various temperatures.

Accounting for optical reflections at various optical elements, the absorptance is around 50 - 55% at the temperatures in this study. For simplicity, we use 60% for the calculations below.

Next, estimate the steady heating due to the pump and probe pulses using a thermal resistor model in cylindrical coordinates. Consider the pump and probe beams as heat sources of radius $r_{pump} \equiv r_1$. The outer radius $r_2 \approx 500 \mu\text{m}$ of the membrane is fixed at the cryostat temperature. The cylindrical conduction resistance is $R = \ln(r_2/r_1)/(2\pi\kappa d)$ where κ is the bulk thermal conductivity of the membrane. The temperature rise is then

$$\Delta T = P_{abs,avg} \frac{\ln(r_2/r_1)}{2\pi\kappa d} \quad (5.21)$$

where $P_{abs,avg}$ is the absorbed average power of the laser beam. The absorbed average power was calculated using $P_{abs,avg} = \alpha P_{inc,avg} = \alpha P_{peak} D$ where $P_{inc,avg}$ is the incident average power on the sample, P_{peak} is the peak power incident on the sample, and D is the duty cycle of the laser beam (1 for pump and 0.032 for probe from a chopper wheel).

Table 5.2 shows the quantities used for steady temperature rise estimation. In Tab. 5.3 T_h is the cryostat temperature, κ is the thermal conductivity used for calculation, and $P_{pu,inc,avg}$ ($E_{pr,inc,avg}$) is the incident average power of the pump (probe) on the sample. The corresponding estimated steady temperature is shown in Tab. 5.3 where ΔT_{pu} (ΔT_{pr}) is the steady temperature rise due to pump (probe), ΔT_{total} is the estimated total steady temperature rise of the sample, and T_{st} is the estimated temperature of the sample.

T_h (K)	κ ($\text{Wm}^{-1}\text{K}^{-1}$)	$P_{pu,inc,avg}$ (μW)	$P_{pr,inc,avg}$ (μW)
300	1.5	41	134
210	1	27	88
135	0.85	48	71
60	0.7	48	61
40	0.55	44	46

Table 5.2: Quantities used for the estimation of the steady heating. The optical powers are actually used values for the measurements.

T_h (K)	ΔT_{pu} (K)	ΔT_{pr} (K)	ΔT_{total} (K)	T_{st} (K)
300	3.4	11.2	14.6	~ 315
210	3.4	11.0	14.4	~ 225
135	7.0	10.5	17.5	~ 150
60	8.5	10.9	19.4	~ 80
40	10.1	10.5	20.6	~ 60

Table 5.3: Estimation of the steady heating of the sample based on the quantities given in Tab.5.2.

Finally, we estimate the impulsive temperature rise induced by the absorbed optical energy. The temperature rise ΔT can be estimated from

$$\Delta T = \frac{E_{abs}}{C_v V} \quad (5.22)$$

where E_{abs} is absorbed laser energy, V is the volume of the sample illuminated by the beam, and C_v is the volumetric heat capacity [196]). The volume $V = \pi r^2 d$ where $d \approx 500$ nm is the estimated thickness of the film, and r is the $1/e^2$ beam radius (pump: $260 \mu\text{m}$, and probe: $235 \mu\text{m}$).

The absorbed laser energy was calculated using $E_{abs} = \alpha E_{inc}$ where α is the measured absorptivity and E_{inc} is the laser energy. The incident laser energy was obtained using $E_{pu}^{inc} = P_{pu}^{inc} / f$ for pump and $E_{pr}^{inc} = P_{pr}^{inc} t_{chop}$ for probe where E_{pu}^{inc} (E_{pr}^{inc}) is the pump (probe) energy incident on the sample, P_{pu}^{inc} (P_{pr}^{inc}) is the incident pump (peak probe) power, f is the repetition rate of the pump (200 Hz), and the t_{chop} is the time duration of the probe (160 μs).

T_{st} (K)	C_v (Jcm^{-3})	E_{pu}^{inc} (μJ)	E_{pr}^{inc} (μJ)	ΔT_{pu} (K)	ΔT_{pr} (K)	ΔT_{total} (K)
315	2.27	0.2	0.7	0.5	2.0	~ 3
225	2	0.1	0.4	0.4	1.5	~ 2
150	1.5	0.2	0.4	0.9	1.6	~ 3
80	0.73	0.2	0.3	1.9	2.9	~ 5
60	0.52	0.2	0.2	2.4	3.1	~ 6

Table 5.4: Estimation of the transient heating of the sample at several temperatures.

Table 5.4 shows the estimated transient temperature rise where T_{st} is the estimated temperature accounting for the steady temperature rise, C_v is the heat capacity at $T = T_{st}$ in Ref. [196], ΔT_{pu} (ΔT_{pr}) is the transient temperature rise due to pump (probe), and ΔT_{total} is the overall transient temperature rise of the sample.

Bulk thermal conductivity of aSi

We conducted TG measurements versus grating period at several temperatures and versus temperature at a fixed grating period of $L = 10.7 \mu\text{m}$. In our experiment, the maximum grating period used is $15.7 \mu\text{m}$. Figure 5.13B shows representative normalized signal traces at ~ 315 K. Shown are average heterodyne signals (10^4 averages) taken at a single location. Note that measured diffusivities in the main text were obtained by measuring multiple locations from which we determined the mean value and error bars. Additional data along with fits are shown in Fig. 5.14. The decay exhibits a single exponential profile with a time constant in the range of tens of nanoseconds to microseconds due to thermal transport. The thermal diffusivity is obtained by extracting the time constant of the single exponential decay; the thermal conductivity is then computed using the measured heat capacity from Ref. [196].

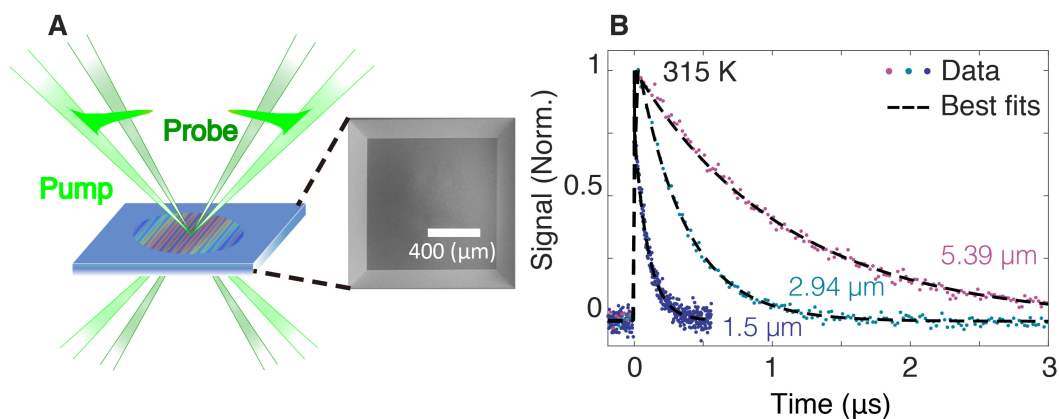


Figure 5.13: (A) Schematic of the TG experiment. Two pump laser pulses are interfered on the sample, impulsively creating a spatially periodic temperature rise. The probe beams diffract from the transient grating, monitoring the thermal relaxation. A scanning electron microscope image of the free-standing amorphous silicon membrane is shown. (B) Representative measured signals versus time and single exponential fits for aSi at 315 K for various grating periods.

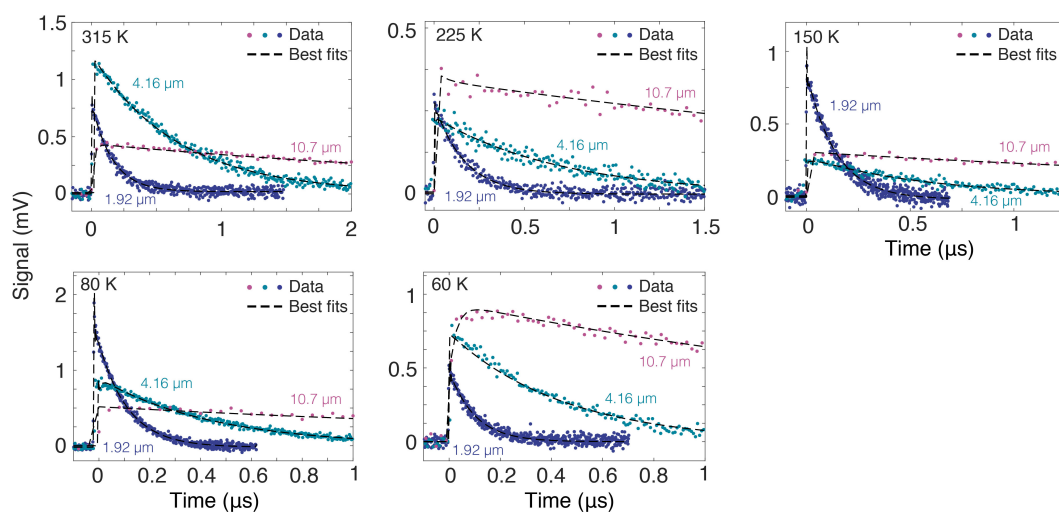


Figure 5.14: Measured TG signal versus time from 60 K to 315 K at several grating periods.

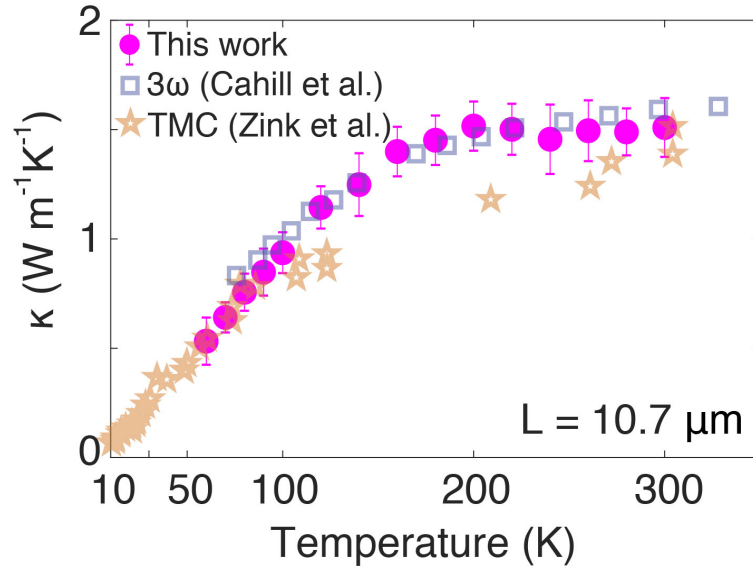


Figure 5.15: Measured thermal conductivity versus temperature for $L = 10.7 \mu\text{m}$. Literature data are 3ω measurements on a 520 nm thick film (open squares, Ref. [197]), and thin film microcalorimetry measurements on a 278 nm thick film (open stars, Ref. [198]).

Within the uncertainty of the measurement, the thermal diffusivity does not vary with a grating period above $10.7 \mu\text{m}$, so we take the value at $10.7 \mu\text{m}$ to be the bulk value. The thermal conductivity versus temperature for $10.7 \mu\text{m}$ is given in Fig. 5.15 along with literature measurements; each point represents the average of $\sim 10^4$ measurements taken at multiple locations on the membrane. Our measured values are generally in good agreement with prior reports.

Ballistic transport of acoustic excitations in aSi

The measured TG signal for a grating period of $L = 754 \text{ nm}$ is shown in Fig. 5.16A. The actual thermal decay is clearly slower than that expected based on the bulk thermal conductivity value, indicating the presence of acoustic excitations with MFPs comparable to the grating period. Measurements of the decay rate versus q^2 for all the grating periods at 80 K are given in Fig. 5.16B. The measured decay rate is close to that predicted by the bulk thermal conductivity up to around $q^2 \sim 4.6 \mu\text{m}^{-2}$ ($L \sim 3 \mu\text{m}$), above which the decay rate becomes smaller. The maximum relative deviation in time constant is on the order of 50% as shown in Fig. 5.16C. Figure 5.16D shows the measured thermal conductivity versus grating period obtained from these time constants at two of the five temperatures considered in this study. As the grating period becomes comparable to some MFPs, the effective thermal

conductivity varies with the grating period.

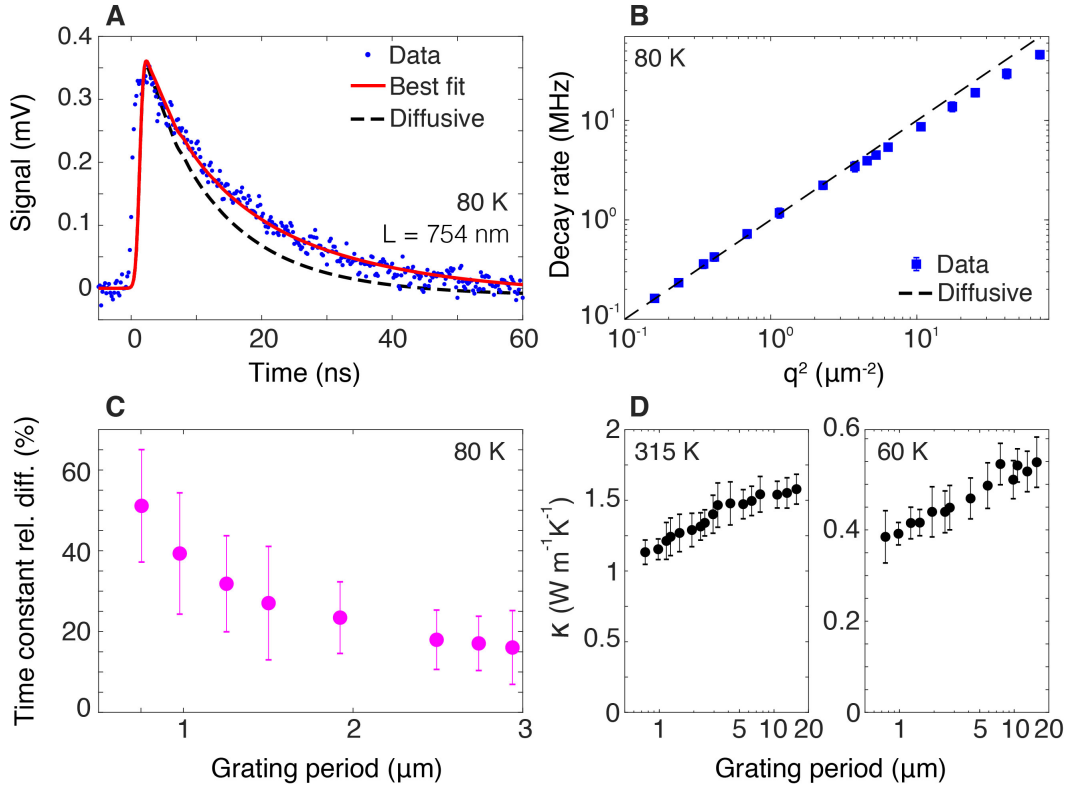


Figure 5.16: (A) Measured TG signal versus time (symbols) for grating period $L = 754$ nm, corresponding to $q^2 \sim 70 \mu\text{m}^{-2}$, along with the best fit (solid red line) and expected decay from the diffusion theory (dashed black line). The actual signal decays slower than predicted, indicating a departure from diffusive thermal transport. (B) Inverse time constant versus q^2 . The measured decay rates follow a linear trend of diffusive thermal transport for $q^2 \lesssim 4.6 \mu\text{m}^{-2}$ ($L \gtrsim 3 \mu\text{m}$), above which a clear deviation is observed. (C) Relative difference $(t_{\text{actual}} - t_{\text{bulk}})/t_{\text{bulk}}$ in the thermal decay time constant versus the grating period. (D) Measured thermal conductivity versus grating period at 315 K and 60 K. The thermal conductivity exhibits a dependence on the grating period, indicating the presence of heat-carrying acoustic excitations with MFPs comparable to the grating period.

The grating period dependence of the thermal conductivity provides constraints on the frequency-dependence of the MFPs of sub-THz excitations. Following Ref. [35], the measured thermal conductivity κ_i can be expressed as

$$\kappa_i = \sum_s \int_0^{\omega_{m,s}} S(x_{i,s}) \left[\frac{1}{3} C_s(\omega) v_s \Lambda_s(\omega) \right] d\omega + \kappa_{IR} \quad (5.23)$$

where s indexes the polarization, $q_i = 2\pi L_i^{-1}$, $x_{i,s} = q_i \Lambda_s(\omega)$, $S(x_{i,s})$ is the isotropic suppression function in Refs. [34, 35], $\omega_{m,s}$ is the cutoff frequency for collective

acoustic excitations, and κ_{IR} is the contribution from excitations above the Ioffe-Regel (IR) cutoff frequency. The Debye heat capacity C_s is calculated from the group velocities v_s which are known, isotropic, and independent of temperature [151, 174]. The first term of Eq. 5.23 is a Debye model for the thermal conductivity of an isotropic solid that includes the effect of non-diffusive thermal transport over a grating period.

The desired quantity is $\Lambda_s(\omega)$, or the MFP versus frequency for LA and TA polarizations. Additional measurements can be used to further constrain $\Lambda_s(\omega)$ before the TG measurements are used. First, the linewidths of LA excitations at frequencies above 3.7 THz are known from IXS measurements and are independent of temperature [151]. As the TA linewidths are not accessible with IXS, we use the values from MD simulations as they quantitatively agreed with the measurements for the LA branch. These values allow the thermal conductivity of collective excitations above ~ 3.7 THz to be obtained from Eq. 5.23; at room temperature this contribution is $\sim 0.5 \text{ Wm}^{-1}\text{K}^{-1}$.

Second, the attenuation lengths at hypersonic frequencies can be obtained from picosecond acoustics. The room temperature value is available from Ref. [15]. As presented in Sec. 5.4, we performed additional measurements of the acoustic attenuation at temperatures from 30 - 300 K. The values are on the order of 10 - 20 μm in this temperature range.

The lack of temperature dependence of the damping at both 100 GHz and ~ 3 THz suggests that the MFPs at intermediate frequencies should also be independent of temperature. This requirement, the PSA and IXS measurements, and the measured thermal conductivity versus grating period at the 5 temperatures in this study impose tight constraints on the frequency-dependence of the damping in the sub-THz frequencies. Figure 5.17A shows two candidate MFP profiles that satisfy these constraints for the LA and TA branches. Power law dependencies $\Lambda \sim \omega^{-n}$ are assumed and combined using Matthiessen's rule. Profile 1 transitions from a constant value to $n = 4$ corresponding to Rayleigh scattering, while profile 2 transitions from constant to $n = 4$ at $\sim 2 - 3$ THz and then to $n = 1$ at $\sim 200 - 300$ GHz.

A representative plot of thermal conductivity versus grating period using Eq. 5.23 at 60 K is given in Fig. 5.17B. In this figure, κ_{IR} has been taken as a parameter to give the best fit for each profile. Profile 1 fails to reproduce the trend with grating period. An alternate profile that increases as $n = 4$ immediately at 3.7 THz yields a thermal conductivity that exceeds the experimental values at all temperatures (not

shown). We find that only profiles consistent with profile 2 are able to explain the magnitude and grating period dependence of the thermal conductivity. Specifically, the MFPs must remain constant as frequency decreases and then increase rapidly as $n = 4$. To agree with the PSA data, the trend must then switch to $n = 1$ or $n = 2$. From the TG data, we are unable to determine this latter trend owing to the influence of boundary scattering in the 500 nm thick membrane. The specular parameter required to produce MFPs on the order of microns with this membrane thickness is $\sim 95\%$, a value that is consistent with prior studies of phonons in crystalline Si in this frequency band [19]. For concreteness, we choose $n = 1$ in the following analysis and neglect the influence of boundary scattering.

Given these constraints, the MFPs are characterized by two parameters: the transition frequencies from $n = 4$ to $n = 1$ for both acoustic polarizations, $\omega_{m,L}$ and $\omega_{m,T}$. The remaining unknown parameter is κ_{IR} , which may depend on temperature. We identify the parameters that best explain the TG data by numerically optimizing $\omega_{m,L}$, $\omega_{m,T}$, and $\kappa_{IR}(T)$ to best fit the experimental data. The resulting thermal conductivity versus grating period predicted by Eq. 5.23 with these parameters at each temperature is shown in Fig. 5.17, demonstrating good agreement at all temperatures.

The choices of $\omega_{m,L}$, $\omega_{m,T}$, and κ_{IR} that are compatible with the data were determined as follows. The calculated relative differences between experiment κ_{expt} and the calculation κ_{calc} at 60 K using different κ_{IR} values $\kappa_{IR} = 0 - 0.2 \text{ Wm}^{-1}\text{K}^{-1}$ are shown in the left of Fig. 5.18. Blue regions in the left of Fig. 5.18 A - E indicate the cutoff frequencies that minimize the relative difference. We find that the optimized frequencies are in the range of 2-3 THz for LA and 1-2 THz for TA for all cases. As shown in the center column of Fig. 5.18 A - E, κ_{calc} at 60 K agrees with κ_{expt} for $\kappa_{IR} \leq 0.2 \text{ Wm}^{-1}\text{K}^{-1}$ above which the trend of κ_{calc} starts to deviate from that of κ_{expt} . The right column of Fig. 5.18 shows optimized κ_{IR} for 80 - 315 K using the optimized frequencies. The cutoff frequencies above were selected to yield the overall best fit of thermal conductivity versus the grating period at all temperatures. Therefore, although different choices for cutoff frequency and κ_{IR} are possible, the frequency-dependence of the MFPs remains unchanged. A steep slope ($n = 4$) in the sub-THz frequencies is necessary to explain the observed grating dependence of thermal conductivity. We find that the trend of MFP with frequency remains the same for all of these parameter sets.

With optimal $\omega_{m,L}$, $\omega_{m,T}$, the optimal value of κ_{IR} , the thermal conductivity above

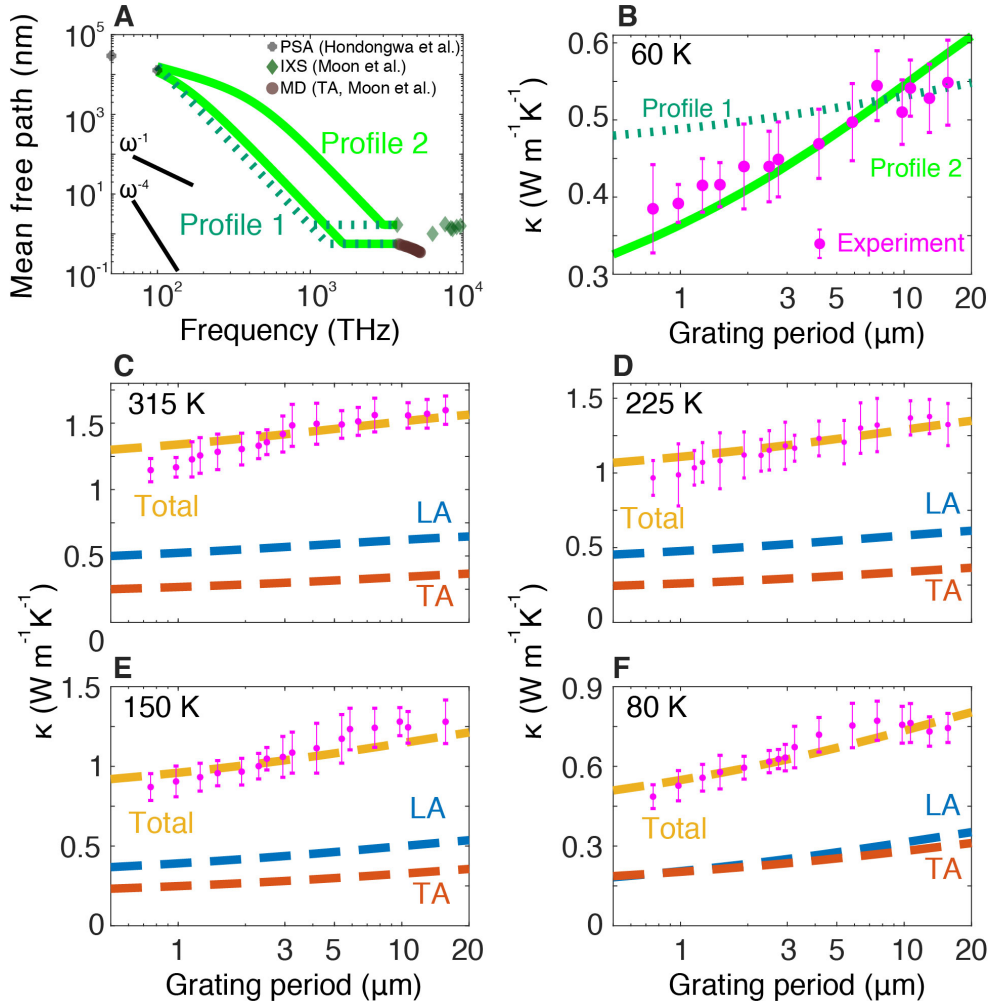


Figure 5.17: (A) Candidate MFP profiles versus frequency: ω^{-4} , constant (profile 1: green dotted lines); ω^{-1}, ω^{-4} , constant (profile 2: green solid lines). Upper and lower curves indicate the LA and TA MFPs, respectively. Literature data are IXS (diamonds, Ref. [151]), PSA at 300 K (asterisks, Ref. [15]), and molecular dynamics (circles, Ref. [174]). (B) Predicted thermal conductivity versus grating period from each candidate profile along with the measured data at 60 K. Only profile 2 reproduces the trend of the measured thermal conductivity with grating period. Measured thermal conductivity versus grating period (symbols) and predicted value from optimized profile 2 (total, dashed yellow line; LA, dashed blue line; TA, dashed red line) for (C) 315 K, (D) 225 K, (E) 150 K, and (F) 80 K. Good agreement is observed at all temperatures with MFPs that are independent of temperature.

the Ioffe-Regel crossover frequency ~ 10 THz for LA and ~ 5 THz for TA [174]) was deduced. Figure 5.19A shows κ_{IR} versus temperature for each profile along with the prediction from Allen-Feldman theory. The theoretical prediction was computed using the expression for mode diffusivity in Ref. [199] and the quantum-

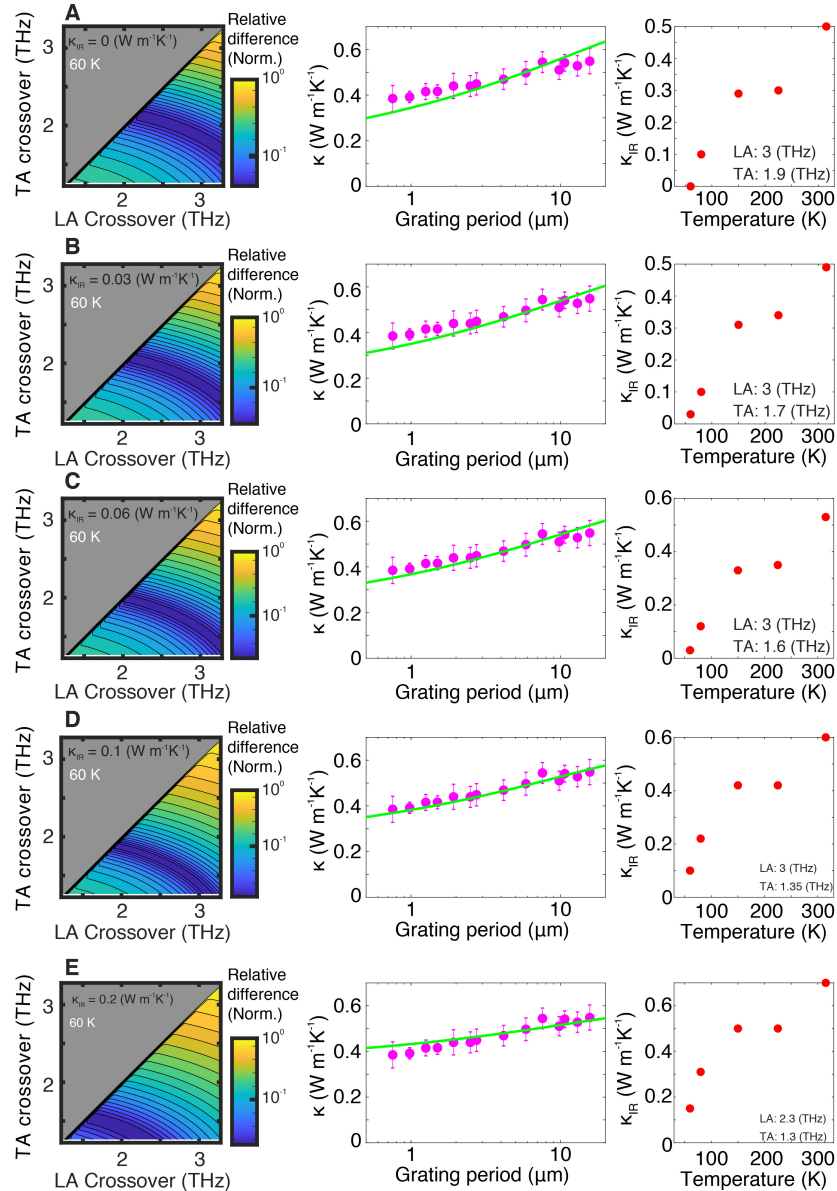


Figure 5.18: (Left) Calculated relative differences at 60 K for (A) $\kappa_{IR} = 0 \text{ W m}^{-1} \text{ K}^{-1}$, (B) $\kappa_{IR} = 0.03 \text{ W m}^{-1} \text{ K}^{-1}$, (C) $\kappa_{IR} = 0.06 \text{ W m}^{-1} \text{ K}^{-1}$, (D) $\kappa_{IR} = 0.1 \text{ W m}^{-1} \text{ K}^{-1}$, and (E) $\kappa_{IR} = 0.2 \text{ W m}^{-1} \text{ K}^{-1}$. The blue area indicates the range of optimized LA / TA crossover frequency which minimize the relative difference. (Center) Calculated thermal conductivity versus grating period (κ_{calc}) using optimized crossover frequencies and experiments at 60 K. As the κ_{IR} increases, the slope of the κ_{calc} becomes less steep. (Right) Optimized κ_{IR} at higher temperatures using optimized crossover frequency determined from minimum relative difference at 60 K.

corrected specific heat. The temperature dependence of the measurements generally agrees with the theory although the theory slightly underestimates the actual values.

Figure 5.19B shows κ_{IR} normalized to its room temperature value along with the normalized heat capacity. The κ_{IR} trend with temperature matches that of the heat capacity.

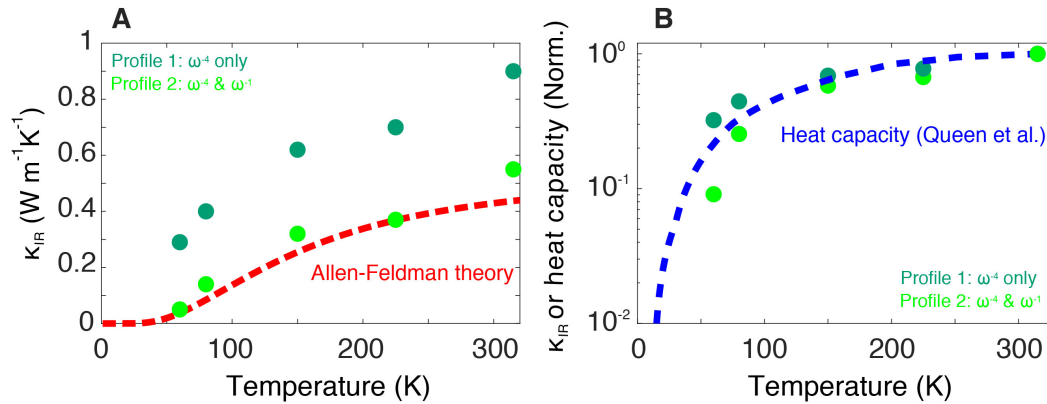


Figure 5.19: (A) Thermal conductivity (κ_{IR}) contributed by excitations above the IR frequency versus temperature for different MFP profiles discussed in the main text. The red dashed line is a prediction using harmonic approximation in disordered solid shown in Ref. [199, 200] for frequencies ≥ 10 THz for LA and ≥ 5 THz for TA. (B) The values in A normalized by their 315 K values along with the normalized heat capacity versus temperature (dashed blue line, Ref. [196]). The thermal conductivity (κ_{IR}) follows the temperature dependence of the heat capacity.

5.6 Unusually weak damping of acoustic excitation in aSi

The extracted MFPs versus frequency for LA and TA branches are shown in Fig. 5.20 along with prior measurements on vitreous silica. The trend for aSi agrees well with these and other measurements in that similar power-law dependencies are observed [28, 156, 158–161, 164, 201]. The $n = 4$ Rayleigh scattering trend for both glasses occurs in the 1 – 3 THz range with a transition to a weaker power law in the sub-THz frequencies. Thus qualitatively, acoustic damping in aSi is not so different from those of other glasses.

However, comparing the attenuation between vitreous silica and aSi, differences also emerge. Comparing the LA MFPs at $\sim 1 - 2$ THz, the attenuation due to Rayleigh scattering is weaker in aSi by around a factor of 5, expected as aSi is a monatomic glass with less atomic disorder. Further, at room temperature the $n = 4$ trend yields to a $n \approx 1 - 2$ trend at ~ 700 GHz in vitreous silica while the same transition occurs at $\sim 300 - 400$ GHz in aSi. At cryogenic temperatures ~ 1 K for vitreous silica, the transition frequencies in both materials are comparable. This difference indicates weaker damping by mechanisms such as two-level systems or

Akhiezer damping in amorphous Si and has an important consequence: excitations with MFPs in the micron range occur at frequencies of $\sim 200 - 1000$ GHz in aSi versus $\lesssim 100$ GHz in vitreous silica at room temperature owing to the steep $n = 4$ slope of Rayleigh scattering. The heat capacity of excitations in the former frequency range is larger by a factor of $(\omega_{aSi}/\omega_{SiO_2})^2 \sim 100$. The result is that in aSi, heat-carrying excitations at room temperature have micron-scale MFPs, while the MFPs of excitations in the same frequency band for vitreous silica are smaller by an order of magnitude. Excitations in vitreous silica with micron-scale MFPs have too low frequency to transport substantial heat at room temperature. Remarkably, the attenuation observed in aSi up to room temperature is of the same order as that measured in vitreous silica at 1 K, highlighting the unusually weak acoustic damping in aSi.

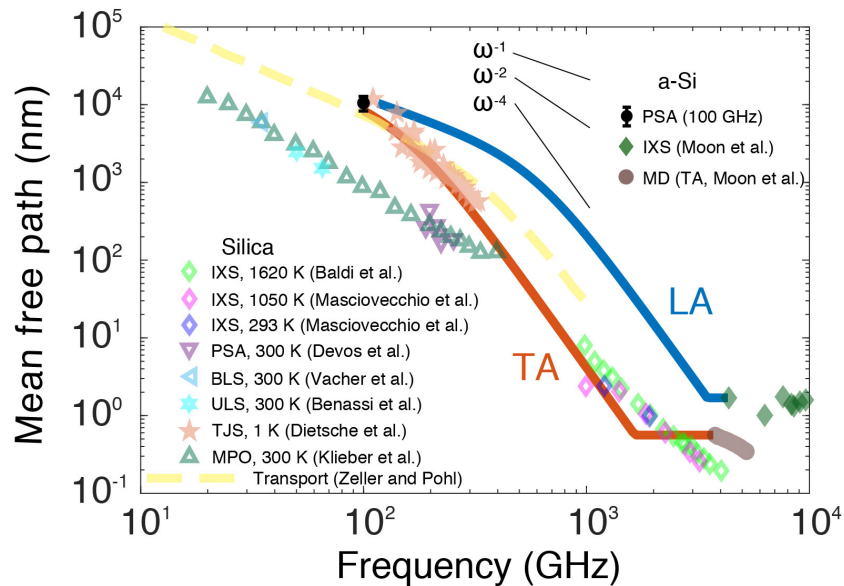


Figure 5.20: Mean free path versus frequency for thermal acoustic excitations in aSi at 300 K along with literature data for vitreous silica from inelastic x-ray scattering (diamonds, Ref. [28, 154]), picosecond acoustics (downward pointing triangles, Ref. [161]), Brillouin light scattering (left-pointing triangles, Ref. [158] and 6-pointed stars, Ref. [159]), tunnel junction spectroscopy (5-pointed stars, Ref. [156]), a multi-pulse optical technique (upward pointing triangles, Ref. [195]), and from transport measurements (dashed line, Ref. [18]).

Our conclusions on the origin of damping of sub-THz excitations in aSi are consistent with these prior studies of other glasses, and the extracted $\kappa_{IR}(T)$ for excitations above the IR frequency is compatible with Allen-Feldman theory. However, our

results are not consistent with the conclusions of numerical studies of excitations below the IR frequency [13, 16, 171, 172, 202]. In these studies, the Hamiltonian for atoms in a supercell is diagonalized in the harmonic approximation to yield normal modes. The original studies of Allen and Feldman used these normal modes to classify excitations in glasses as propagons, diffusons, and locons depending on the properties of the eigenvectors [200]. The lifetimes of these modes are obtained using normal mode decomposition and molecular dynamics [203, 204]. With these approaches, these studies have generally concluded that damping in aSi varies as ω^{-2} for frequencies around $\sim 1 - 2$ THz and below. From this trend, the damping mechanism has been postulated to involve anharmonicity [171, 172] and to exhibit a temperature dependence [16].

Discussion

We first address the classification of acoustic excitations. Various numerical [14, 16, 171] and experimental works [170] have noted a transition in the character of vibrations in aSi around $\sim 1 - 2$ THz, leading to the introduction of “diffusons” as non-propagating yet delocalized vibrations in Refs. [14, 16]. In contrast, our work attributes this change to a frequency-dependent damping of collective acoustic excitations. The crossover from propagons and diffusons at $\sim 1 - 2$ THz coincides with the transition from Rayleigh scattering to the Kittel regime in the present work and thus can be explained without the definition of a new type of vibration. The IR crossover for the transition from collective excitations to incoherent excitations, which occurs well above 1-2 THz in amorphous Si, is sufficient to describe the different characters of excitations in glasses.

The second inconsistency is the prediction by normal-mode analysis of the frequency-dependence ($n = 2$) and anharmonic origin of damping in the few THz frequency range. Specifically, the MFPs predicted from normal mode analysis are on the order of 20 nm at ~ 1 THz (smaller by factor of 5 compared to present value of ~ 100 nm) and vary as ω^{-2} (see Fig. 4B of Ref. [171]), which cannot explain the measurements of the present work. Here, the inconsistency appears to arise from the implicit assumption of the normal mode decomposition that the heat-carrying excitations in glasses are the normal modes of the supercell. This assumption is not compatible with basic many-body physics and scattering theory, which instead gives the proper definition and lifetime of a collective excitation of a many-body system using the self-energy and the single-particle Green’s function [205]. Rather than normal modes, a physical picture of acoustic excitations of a glass that is compatible

with this framework is that originally postulated by Kittel [17] in the continuum limit and later by Zeller and Pohl [18], in which a glass is imagined to consist of a fictitious atomic lattice along with perturbations representing the mass and force constant disorder in the actual glass. The undamped excitations of the fictitious atomic lattice acquire a lifetime owing to the disorder of the actual glass. The dispersion and lifetimes of these excitations can be measured experimentally using inelastic scattering, as has been performed for many glasses in the past decades [28, 151–155]. In contrast, the lifetimes of normal modes do not appear to be experimentally accessible or physically meaningful as they are unable to explain the thermal conductivity measurements presented here.

5.7 Summary

In summary, we have obtained measurements of the frequency-dependent MFPs of sub-THz acoustic excitations in amorphous silicon using picosecond acoustics and transient grating spectroscopy. The MFPs lack a temperature dependence and exhibit a trend characteristic of structural scattering by point defects and density fluctuations. This result is at variance with numerical studies based on normal mode analysis but is broadly consistent with prior studies of vitreous silica and other glasses. The micron-scale MFPs of heat-carrying excitations at room temperature are found to arise primarily from the weak anharmonic and two-level system damping of sub-THz excitations, leading to room temperature attenuation coefficients comparable to those of other glasses at cryogenic temperatures.

CONCLUSION AND FUTURE WORKS

6.1 Summary

The rapid experimental advancement in recent years has promised better understanding of the microscopic heat transport properties in materials. In this context, the focus of this thesis is on addressing a critical problem in heat conduction: understanding and characterizing microscopic transport that drives the bulk thermal properties in thermally conductive polymers and amorphous materials. The elucidation of the mechanism can resolve long-standing questions over decades, and provide useful insights for their applications. Using thermal transient grating (TG) as a tool for MFP spectroscopy, we introduced a new picture and route for better understanding of the transport of the heat-carrying vibrations in these substances.

In chapter 2, we introduced the TG and described its leverage for measuring the thermal transport in crystalline thin films. We have motivated by introducing the TG and explaining the key requirements for the TG, which can improve its ability of adaptation for experimental probe with relevant length and time scales. Finally, we validated TG's capability by demonstrating measurements of the bulk thermal properties of crystalline silicon thin-film.

In chapter 3, we presented in-plane vibrational properties of free-standing MoS₂ membranes. We have described the adaptiveness of the TG by introducing a time-resolved transient grating with a temporal resolution less than 100 fs for measuring thermal and elastic properties, concurrently. We first experimentally reported in-plane sound velocity of $7000 \pm 40 \text{ m s}^{-1}$, which demonstrated an excellent agreement with ab-initio prediction of the phonon group velocity along the $\Gamma-K$ Brillouin zone. We also reported a value of in-plane thermal conductivity of $74 \pm 21 \text{ Wm}^{-1}\text{K}^{-1}$, which we do not observe a grating period dependent thermal conductivity. We explained our observation based on the ab-initio calculation of the accumulated thermal conductivity versus the phonon mean free path; mean free paths of the thermal acoustic phonons are smaller than the thermal length scale considered in this experiment.

In chapter 4, we discussed our measurements of TG to resolve the microscopic transport of heat carrying acoustic phonons in highly oriented semi-crystalline

polyethylene (PE). For this purpose, we began with bulk measurements concerning the in-plane thermal anisotropy along with temperature dependent thermal conductivity; qualitative description of the mesoscopic transport phenomena in partially oriented PE was provided. Next, we presented our measurements of the mean free path of heat-carrying acoustic phonons in actual samples of highly oriented polyethylene. For extracting accumulated thermal conductivity, a Bayesian inference was applied; we showed that phonons with mean free paths (MFP) on micron length scales are the dominant heat carriers in highly oriented polyethylene. We further showed a frequency resolved MFP using a low-energy anisotropic Debye model; we found evidence of one-dimensional density states of phonons with a frequency less than ~ 2 THz. The transition frequency is consistent with prior observations in highly oriented PE; the stiff longitudinal branch makes the acoustic phonons to have a wavelength of 8 nm which is comparable to prior reports of fiber diameter ~ 10 nm. Therefore, the wavelength of low-frequency heat-carrying acoustic phonons exceeds the fiber diameter dimension. Our results provide insights into the actual upper-limit of the thermal conductivity in highly oriented polymers that will prove useful for developing thermally conductive polymers.

In chapter 5, we described the microscopic origin of the heat-carrying acoustic excitation in amorphous materials. Over the decade, the transport of the excitations in amorphous silicon has been contentious; numerous predictions showed contradictions with experimental results. To address this, we presented a novel approach in which we probed thermal conduction at sub-micron length scales in thin amorphous Si films using transient grating spectroscopy and picosecond acoustics. We provided an evidence of ballistic excitations over the grating period that allows us to discover the primary damping mechanisms versus frequency from 0.1 - 3 THz. We found that the primary damping mechanism in amorphous Si is Rayleigh scattering, contrary to the predictions of normal mode analysis; the absence of anharmonic or two-level system damping enables micron-scale mean free paths at room temperature. We provided a clear picture of acoustic damping in amorphous Si and our approach thus allows us to confirm or refute this widely-used theory by understanding vibrations as acoustic excitation rather than propagons, diffusons, and locons.

6.2 Outlook and future insight

Concerning the heat transport in semicrystalline polymers and amorphous materials, there exist numerous questions that remain unresolved.

In polymers, one future work is decreasing a considerable knowledge gap between computational predictions and experiments. As earlier mentioned, the computations cannot accurately capture the role of the microstructures on the transport of heat-carrying acoustic phonons. In fact, our understandings from the computations are limited to smaller computational domains (single chain or perfect molecular crystal), therefore explicit structure affected phonon properties was less described. For instance, despite experimental evidences regarding phonon-interchain interactions, there is a lack of quantitative description on them. In collaboration with improved computations, our experimental findings in chapter 4 will aid to establish a comprehensive picture for microscopic heat transport that are subject to the microstructure.

In this regard, considering the importance of the impact of the structure to the transport of the heat-carrying acoustic phonons, a systematic experimental study at different draw ratio (DR) needs to be done. The draw ratios of the polymers that were analyzed in this thesis are limited: DR4, 5, 7.5, and 200. A systematic study for semi-crystalline polymers with various DR will further improve our understanding of the heat transport in polymers.

Regarding amorphous silicon, the understanding of the transport of the excitations has relied on a classification introduced by Allen and Feldman; a concept of propagons, diffusons, locons was proposed based on normal mode analysis. As earlier mentioned, according to this theory, propagons are phonon-like, delocalized, propagating vibrations; locons as localized modes; and diffusons as delocalized yet non-propagating vibrations. Dozens of papers have been written on the atomic vibrations of glasses with this framework as a starting point, but have faced discrepancies with experiments. Therefore, the criteria of the classification of the normal mode analysis should be examined again. We believe that our experimental results in chapter 5 will set the stage for establishing a clear picture in a basis of collective acoustic excitations rather than propagon, diffuson, and locons.

On the experimental side, the transient grating as a tool for MFP spectroscopy can be further improved, we highlight that the results of TG can be better explained with a combination of other technique, which can potentially provide tight constraints for the frequency-resolved MFPs. For example, in this thesis, we presented a table-top approach using the results from a dominant phonon approximation on prior results or picosecond acoustics measurements. To move forward in aSi, results of higher frequency excitations from in-elastic x-ray scattering and in-elastic

neutron scattering can further provide the constraints, therefore enabling to probe the phonon transport in a wide range of frequencies. Second, to study heat transport of disordered materials, the relevant length and time scales should be provided. In particular, the measurement of transport in amorphous regions is difficult without further enhancing the spatial resolution. The minimum thermal length scale shown in this thesis is an order of 100 nm, which may be still far longer than the MFP of heat-carrying acoustic excitations in amorphous materials with a strong damping. This can be addressed by employing extreme UV as a source, which is just being developed.

Another future work is experimentally exploring a new transport regime using TG. The transport regimes that are presented in this thesis are weak quasi-ballistic and diffusive regimes. On the other hand, numerical predictions have suggested that there are other transport regimes including collective-diffusive, strongly ballistic, and hydrodynamic transport regimes. Further improvements in TG combined with advances in the sample preparation can confirm the numerical suggestions.

To conclude, we have utilized the capabilities of TG to provide useful insights for the damping of the heat-carrying acoustic excitations in semi-crystalline polymers and amorphous materials. We believe that our approaches and results here will provide fundamental insights into the transport of the heat-carrying acoustic excitations in these substances, which were challenging with various conventional methods. A better understanding of heat transport in these substances will eventually provide an opportunity for promising applications beyond conventional use.

BIBLIOGRAPHY

- [1] Matthew C Wingert, Jianlin Zheng, Soonshin Kwon, and Renkun Chen. Thermal transport in amorphous materials: a review. *Semiconductor Science and Technology*, 31(11):113003, oct 2016. doi: 10.1088/0268-1242/31/11/113003. URL <https://doi.org/10.1088/0268-1242/31/11/113003>.
- [2] D.A. Reay. The use of polymers in heat exchangers. *Heat Recovery Systems and CHP*, 9(3):209 – 216, 1989. ISSN 0890-4332. doi: [https://doi.org/10.1016/0890-4332\(89\)90004-5](https://doi.org/10.1016/0890-4332(89)90004-5). URL <http://www.sciencedirect.com/science/article/pii/0890433289900045>.
- [3] Taesoo D. Lee and Abasifreke U. Ebong. A review of thin film solar cell technologies and challenges. *Renewable and Sustainable Energy Reviews*, 70:1286 – 1297, 2017. ISSN 1364-0321. doi: <https://doi.org/10.1016/j.rser.2016.12.028>. URL <http://www.sciencedirect.com/science/article/pii/S136403211631070X>.
- [4] James E. Mark, editor. *Physical Properties of Polymers Handbook*. Springer-Verlag, New York, 2 edition, 2007. ISBN 978-0-387-31235-4. doi: 10.1007/978-0-387-69002-5. URL <https://www.springer.com/gp/book/9780387312354>.
- [5] L Piraux, M Kinany-Alaoui, J. P Issi, D Begin, and D Billaud. Thermal conductivity of an oriented polyacetylene film. *Solid State Communications*, 70(4):427–429, March 1989. ISSN 0038-1098. doi: 10.1016/0038-1098(89)91073-9. URL <http://www.sciencedirect.com/science/article/pii/0038109889910739>.
- [6] C. L. Choy, F. C. Chen, and W. H. Luk. Thermal conductivity of oriented crystalline polymers. *Journal of Polymer Science: Polymer Physics Edition*, 18(6):1187–1207, 1980. doi: 10.1002/pol.1980.180180603. URL <https://onlinelibrary.wiley.com/doi/abs/10.1002/pol.1980.180180603>.
- [7] Basil D. Washo and David Hansen. Heat conduction in linear amorphous high polymers: Orientation anisotropy. *Journal of Applied Physics*, 40(6): 2423–2427, 1969. doi: 10.1063/1.1658009. URL <https://doi.org/10.1063/1.1658009>.
- [8] D Greig and M Sahota. Thermal conductivity of extruded polyethylene. *Polymer*, 19(5):503 – 505, 1978. ISSN 0032-3861. doi: [https://doi.org/10.1016/0032-3861\(78\)90271-9](https://doi.org/10.1016/0032-3861(78)90271-9). URL <http://www.sciencedirect.com/science/article/pii/0032386178902719>.

- [9] Yanfei Xu, Daniel Kraemer, Bai Song, Zhang Jiang, Jiawei Zhou, James Loomis, Jianjian Wang, Mingda Li, Hadi Ghasemi, Xiaopeng Huang, Xiaobo Li, and Gang Chen. Nanostructured polymer films with metal-like thermal conductivity. *Nature Communications*, 10(1):1–8, April 2019. ISSN 2041-1723. doi: 10.1038/s41467-019-09697-7. URL <https://www.nature.com/articles/s41467-019-09697-7>.
- [10] Virendra Singh, Thomas L. Bougher, Annie Weathers, Ye Cai, Kedong Bi, Michael T. Pettes, Sally A. McMnamin, Wei Lv, Daniel P. Resler, Todd R. Gattuso, David H. Altman, Kenneth H. Sandhage, Li Shi, Asegun Henry, and Baratunde A. Cola. High thermal conductivity of chain-oriented amorphous polythiophene. *Nature Nanotechnology*, 9(5):384–390, 2014. doi: 10.1038/nnano.2014.44. URL <https://doi.org/10.1038/nnano.2014.44>.
- [11] Soonshin Kwon, Jianlin Zheng, Matthew C. Wingert, Shuang Cui, and Renkun Chen. Unusually high and anisotropic thermal conductivity in amorphous silicon nanostructures. *ACS Nano*, 11(3):2470–2476, 2017. doi: 10.1021/acsnano.6b07836. URL <https://doi.org/10.1021/acsnano.6b07836>. PMID: 28117979.
- [12] Xiao Liu, B. E. White, Jr., R. O. Pohl, E. Iwanizcko, K. M. Jones, A. H. Mahan, B. N. Nelson, R. S. Crandall, and S. Veprek. Amorphous solid without low energy excitations. *Phys. Rev. Lett.*, 78:4418–4421, Jun 1997. doi: 10.1103/PhysRevLett.78.4418. URL <https://link.aps.org/doi/10.1103/PhysRevLett.78.4418>.
- [13] Jaroslav Fabian and Philip B. Allen. Theory of sound attenuation in glasses: The role of thermal vibrations. *Phys. Rev. Lett.*, 82:1478–1481, Feb 1999. doi: 10.1103/PhysRevLett.82.1478. URL <https://link.aps.org/doi/10.1103/PhysRevLett.82.1478>.
- [14] Philip B. Allen, Joseph L. Feldman, Jaroslav Fabian, and Frederick Wooten. Diffusons, locons and propagons: Character of atomic vibrations in amorphous si. *Philosophical Magazine B*, 79(11-12):1715–1731, 1999. doi: 10.1080/13642819908223054. URL <https://doi.org/10.1080/13642819908223054>.
- [15] D. B. Hondongwa, B. C. Daly, T. B. Norris, B. Yan, J. Yang, and S. Guha. Ultrasonic attenuation in amorphous silicon at 50 and 100 ghz. *Phys. Rev. B*, 83:121303, Mar 2011. doi: 10.1103/PhysRevB.83.121303. URL <https://link.aps.org/doi/10.1103/PhysRevB.83.121303>.
- [16] Jaroslav Fabian and Philip B. Allen. Anharmonic decay of vibrational states in amorphous silicon. *Phys. Rev. Lett.*, 77:3839–3842, Oct 1996. doi: 10.1103/PhysRevLett.77.3839. URL <https://link.aps.org/doi/10.1103/PhysRevLett.77.3839>.

- [17] Charles Kittel. Interpretation of the thermal conductivity of glasses. *Phys. Rev.*, 75:972–974, Mar 1949. doi: 10.1103/PhysRev.75.972. URL <https://link.aps.org/doi/10.1103/PhysRev.75.972>.
- [18] R. C. Zeller and R. O. Pohl. Thermal conductivity and specific heat of noncrystalline solids. *Phys. Rev. B*, 4:2029–2041, Sep 1971. doi: 10.1103/PhysRevB.4.2029. URL <https://link.aps.org/doi/10.1103/PhysRevB.4.2029>.
- [19] Tom Klitsner and R. O. Pohl. Phonon scattering at silicon crystal surfaces. *Phys. Rev. B*, 36:6551–6565, Oct 1987. doi: 10.1103/PhysRevB.36.6551. URL <https://link.aps.org/doi/10.1103/PhysRevB.36.6551>.
- [20] Robert O. Pohl, Xiao Liu, and EunJoo Thompson. Low-temperature thermal conductivity and acoustic attenuation in amorphous solids. *Rev. Mod. Phys.*, 74:991–1013, Oct 2002. doi: 10.1103/RevModPhys.74.991. URL <https://link.aps.org/doi/10.1103/RevModPhys.74.991>.
- [21] G. Chen. Size and Interface Effects on Thermal Conductivity of Superlattices and Periodic Thin-Film Structures. *Journal of Heat Transfer*, 119(2):220–229, 05 1997. ISSN 0022-1481. doi: 10.1115/1.2824212. URL <https://doi.org/10.1115/1.2824212>.
- [22] G. Chen. *Nanoscale Energy Transport and Conversion: A Parallel Treatment of Electrons, Molecules, Phonons, and Photons*. MIT-Pappalardo Series in Mechanical Engineering. Oxford University Press, 2005. ISBN 9780199774685. URL <https://books.google.com/books?id=M3n31UJpYDYC>.
- [23] A. Majumdar. Microscale Heat Conduction in Dielectric Thin Films. *Journal of Heat Transfer*, 115(1):7–16, 02 1993. ISSN 0022-1481. doi: 10.1115/1.2910673. URL <https://doi.org/10.1115/1.2910673>.
- [24] Y. S. Ju and K. E. Goodson. Phonon scattering in silicon films with thickness of order 100 nm. *Applied Physics Letters*, 74(20):3005–3007, 1999. doi: 10.1063/1.123994. URL <https://doi.org/10.1063/1.123994>.
- [25] A J Minnich. Advances in the measurement and computation of thermal phonon transport properties. *Journal of Physics: Condensed Matter*, 27(5):053202, jan 2015. doi: 10.1088/0953-8984/27/5/053202. URL <https://doi.org/10.1088%2F0953-8984%2F27%2F5%2F053202>.
- [26] A. Mermet, L. David, M. Lorenzen, and M. Krisch. Inelastic x-ray scattering from stretch-oriented polyethylene. *The Journal of Chemical Physics*, 119(3):1879–1884, 2003. doi: 10.1063/1.1579681. URL <https://doi.org/10.1063/1.1579681>.

- [27] S. Kavesh and J. M. Schultz. Lamellar and interlamellar structure in melt-crystallized polyethylene. i. degree of crystallinity, atomic positions, particle size, and lattice disorder of the first and second kinds. *Journal of Polymer Science Part A-2: Polymer Physics*, 8(2):243–276, 1970. doi: 10.1002/pol.1970.160080205. URL <https://onlinelibrary.wiley.com/doi/abs/10.1002/pol.1970.160080205>.
- [28] G. Baldi, V. M. Giordano, G. Monaco, and B. Ruta. Sound Attenuation at Terahertz Frequencies and the Boson Peak of Vitreous Silica. *Physical Review Letters*, 104(19):195501, May 2010. doi: 10.1103/PhysRevLett.104.195501. URL <https://link.aps.org/doi/10.1103/PhysRevLett.104.195501>.
- [29] O. Delaire, J. Ma, K. Marty, A. F. May, M. A. McGuire, M-H. Du, D. J. Singh, A. Podlesnyak, G. Ehlers, M. D. Lumsden, and B. C. Sales. Giant anharmonic phonon scattering in pbte. *Nature Materials*, 10(8):614–619, 2011. doi: 10.1038/nmat3035. URL <https://doi.org/10.1038/nmat3035>.
- [30] M. Zebarjadi, K. Esfarjani, M. S. Dresselhaus, Z. F. Ren, and G. Chen. Perspectives on thermoelectrics: from fundamentals to device applications. *Energy Environ. Sci.*, 5:5147–5162, 2012. doi: 10.1039/C1EE02497C. URL <http://dx.doi.org/10.1039/C1EE02497C>.
- [31] Yee Kan Koh and David G. Cahill. Frequency dependence of the thermal conductivity of semiconductor alloys. *Phys. Rev. B*, 76:075207, Aug 2007. doi: 10.1103/PhysRevB.76.075207. URL <https://link.aps.org/doi/10.1103/PhysRevB.76.075207>.
- [32] A. J. Minnich, J. A. Johnson, A. J. Schmidt, K. Esfarjani, M. S. Dresselhaus, K. A. Nelson, and G. Chen. Thermal conductivity spectroscopy technique to measure phonon mean free paths. *Phys. Rev. Lett.*, 107:095901, Aug 2011. doi: 10.1103/PhysRevLett.107.095901. URL <https://link.aps.org/doi/10.1103/PhysRevLett.107.095901>.
- [33] Jeremy A. Johnson, A. A. Maznev, John Cuffe, Jeffrey K. Eliason, Austin J. Minnich, Timothy Kehoe, Clivia M. Sotomayor Torres, Gang Chen, and Keith A. Nelson. Direct measurement of room-temperature nondiffusive thermal transport over micron distances in a silicon membrane. *Physical Review Letters*, 110(2):025901, January 2013. doi: 10.1103/PhysRevLett.110.025901. URL <http://link.aps.org/doi/10.1103/PhysRevLett.110.025901>.
- [34] A. A. Maznev, Jeremy A. Johnson, and Keith A. Nelson. Onset of nondiffusive phonon transport in transient thermal grating decay. *Phys. Rev. B*, 84:195206, Nov 2011. doi: 10.1103/PhysRevB.84.195206. URL <https://link.aps.org/doi/10.1103/PhysRevB.84.195206>.

- [35] A. J. Minnich. Determining phonon mean free paths from observations of quasiballistic thermal transport. *Phys. Rev. Lett.*, 109:205901, Nov 2012. doi: 10.1103/PhysRevLett.109.205901. URL <https://link.aps.org/doi/10.1103/PhysRevLett.109.205901>.
- [36] Navaneetha K. Ravichandran, Hang Zhang, and Austin J. Minnich. Spectrally resolved specular reflections of thermal phonons from atomically rough surfaces. *Phys. Rev. X*, 8:041004, Oct 2018. doi: 10.1103/PhysRevX.8.041004. URL <https://link.aps.org/doi/10.1103/PhysRevX.8.041004>.
- [37] Andrew B. Robbins, Stavros X. Drakopoulos, Ignacio Martin-Fabiani, Sara Ronca, and Austin J. Minnich. Ballistic thermal phonons traversing nanocrystalline domains in oriented polyethylene. *Proceedings of the National Academy of Sciences*, 116(35):17163–17168, 2019. ISSN 0027-8424. doi: 10.1073/pnas.1905492116. URL <https://www.pnas.org/content/116/35/17163>.
- [38] M D Fayer. Dynamics of molecules in condensed phases: Picosecond holographic grating experiments. *Annual Review of Physical Chemistry*, 33(1):63–87, 1982. doi: 10.1146/annurev.pc.33.100182.000431. URL <https://doi.org/10.1146/annurev.pc.33.100182.000431>.
- [39] John A. Rogers and Keith A. Nelson. Study of lamb acoustic waveguide modes in unsupported polyimide thin films using real-time impulsive stimulated thermal scattering. *Journal of Applied Physics*, 75(3):1534–1556, 1994. doi: 10.1063/1.356998. URL <https://doi.org/10.1063/1.356998>.
- [40] H. J. Eichler, P. Gunter, and D. W. Pohl. *Laser-induced dynamic gratings / H.J. Eichler, P. Gunter, D.W. Pohl*. Springer-Verlag Berlin ; New York, 1986. ISBN 0387158758.
- [41] A. A. Maznev, K. A. Nelson, and J. A. Rogers. Optical heterodyne detection of laser-induced gratings. *Opt. Lett.*, 23(16):1319–1321, Aug 1998. doi: 10.1364/OL.23.001319. URL <http://ol.osa.org/abstract.cfm?URI=ol-23-16-1319>.
- [42] Robert J Collier, Christoph B Burckhardt, and Lawrence H Lin. *Optical holography*. Academic Press, New York, NY, 1971. URL <http://cds.cern.ch/record/101210>.
- [43] Darius H. Torchinsky, Jeremy A. Johnson, and Keith A. Nelson. A direct test of the correlation between elastic parameters and fragility of ten glass formers and their relationship to elastic models of the glass transition. *The Journal of Chemical Physics*, 130(6):064502, 2009. doi: 10.1063/1.3072476. URL <https://doi.org/10.1063/1.3072476>.
- [44] Jeremy A. Johnson, Alexei A. Maznev, Mayank T. Bulsara, Eugene A. Fitzgerald, T. C. Harman, S. Calawa, C. J. Vineis, G. Turner, and Keith A.

- Nelson. Phase-controlled, heterodyne laser-induced transient grating measurements of thermal transport properties in opaque material. *Journal of Applied Physics*, 111(2):023503, 2012. doi: 10.1063/1.3675467. URL <http://dx.doi.org/10.1063/1.3675467>.
- [45] O. W. Käding, H. Skurk, A. A. Maznev, and E. Matthias. Transient thermal gratings at surfaces for thermal characterization of bulk materials and thin films. *Applied Physics A*, 61(3):253–261, 1995. doi: 10.1007/BF01538190. URL <https://doi.org/10.1007/BF01538190>.
- [46] John Cuffe, Jeffrey K. Eliason, A. A. Maznev, Kimberlee C. Collins, Jeremy A. Johnson, Andrey Shchepetov, Mika Prunnila, Jouni Ahopelto, Clivia M. Sotomayor Torres, Gang Chen, and Keith A. Nelson. Reconstructing phonon mean-free-path contributions to thermal conductivity using nanoscale membranes. *Phys. Rev. B*, 91:245423, Jun 2015. doi: 10.1103/PhysRevB.91.245423. URL <https://link.aps.org/doi/10.1103/PhysRevB.91.245423>.
- [47] Navaneetha K. Ravichandran, Hang Zhang, and Austin J. Minnich. Spectrally resolved specular reflections of thermal phonons from atomically rough surfaces. *Phys. Rev. X*, 8:041004, Oct 2018. doi: 10.1103/PhysRevX.8.041004. URL <https://link.aps.org/doi/10.1103/PhysRevX.8.041004>.
- [48] A. Vega-Flick, R. A. Duncan, J. K. Eliason, J. Cuffe, J. A. Johnson, J.-P. M. Peraud, L. Zeng, Z. Lu, A. A. Maznev, E. N. Wang, J. J. Alvarado-Gil, M. Sledzinska, C. M. Sotomayor Torres, G. Chen, and K. A. Nelson. Thermal transport in suspended silicon membranes measured by laser-induced transient gratings. *AIP Advances*, 6(12):121903, 2016. doi: 10.1063/1.4968610. URL <https://doi.org/10.1063/1.4968610>.
- [49] Kwangu Kang, Yee Kan Koh, Catalin Chiritescu, Xuan Zheng, and David G. Cahill. Two-tint pump-probe measurements using a femtosecond laser oscillator and sharp-edged optical filters. *Review of Scientific Instruments*, 79(11):114901, 2008. doi: 10.1063/1.3020759. URL <http://dx.doi.org/10.1063/1.3020759>.
- [50] L. M. Osterink and J. D. Foster. Thermal effects and transverse mode control in a nd:yag laser. *Applied Physics Letters*, 12(4):128–131, 1968. doi: 10.1063/1.1651922. URL <https://doi.org/10.1063/1.1651922>.
- [51] R.C. Weast, M.J. Astle, W.H. Beyer, C.R. Company, S.M. Selby, D.R. Lide, H.P.R. Frederikse, W.M. Haynes, J.R. Rumble, and T.J. Bruno. *CRC Handbook of Chemistry and Physics: A Ready-reference Book of Chemical and Physical Data*. CRC Press, 1965. ISBN 9781498784542. URL <https://books.google.com/books?id=8M93zQEACAAJ>.
- [52] J. A. Wilson and A. D. Yoffe. The transition metal dichalcogenides discussion and interpretation of the observed optical, electrical and structural

- properties. *Advances in Physics*, 18(73):193–335, May 1969. ISSN 0001-8732. doi: 10.1080/00018736900101307. URL <http://dx.doi.org/10.1080/00018736900101307>.
- [53] L. F. Mattheiss. Band structures of transition-metal-dichalcogenide layer compounds. *Physical Review B*, 8(8):3719–3740, October 1973. doi: 10.1103/PhysRevB.8.3719. URL <http://link.aps.org/doi/10.1103/PhysRevB.8.3719>.
- [54] Qing Hua Wang, Kouros Kalantar-Zadeh, Andras Kis, Jonathan N. Coleman, and Michael S. Strano. Electronics and optoelectronics of two-dimensional transition metal dichalcogenides. *Nature Nanotechnology*, 7(11):699–712, November 2012.
- [55] A. Kuc, N. Zibouche, and T. Heine. Influence of quantum confinement on the electronic structure of the transition metal sulfide TS_2 . *Physical Review B*, 83(24):245213, June 2011. doi: 10.1103/PhysRevB.83.245213. URL <http://link.aps.org/doi/10.1103/PhysRevB.83.245213>.
- [56] Deep Jariwala, Vinod K. Sangwan, Lincoln J. Lauhon, Tobin J. Marks, and Mark C. Hersam. Emerging device applications for semiconducting two-dimensional transition metal dichalcogenides. *ACS Nano*, 8(2):1102–1120, February 2014. ISSN 1936-0851. doi: 10.1021/nn500064s. URL <http://dx.doi.org/10.1021/nn500064s>.
- [57] Marco Bernardi, Maurizia Palummo, and Jeffrey C. Grossman. Extraordinary sunlight absorption and one nanometer thick photovoltaics using two-dimensional monolayer materials. *Nano Letters*, 13(8):3664–3670, August 2013. ISSN 1530-6984. doi: 10.1021/nl401544y. URL <http://dx.doi.org/10.1021/nl401544y>.
- [58] T. S. Sreeprasad, Phong Nguyen, Namhoon Kim, and Vikas Berry. Controlled, defect-guided, metal-nanoparticle incorporation onto MoS_2 via chemical and microwave routes: Electrical, thermal, and structural properties. *Nano Letters*, 13(9):4434–4441, September 2013. ISSN 1530-6984. doi: 10.1021/nl402278y. URL <http://dx.doi.org/10.1021/nl402278y>.
- [59] Morteza Kayyalha, Jesse Maassen, Mark Lundstrom, Li Shi, and Yong P. Chen. Gate-tunable and thickness-dependent electronic and thermoelectric transport in few-layer MoS_2 . *Journal of Applied Physics*, 120(13):134305, 2016. doi: 10.1063/1.4963364.
- [60] B. Radisavljevic, A. Radenovic, J. Brivio, V. Giacometti, and A. Kis. Single-layer MoS_2 transistors. *Nature Nanotechnology*, 6(3):147–150, March 2011. ISSN 1748-3387. doi: 10.1038/nnano.2010.279. URL <http://www.nature.com.clsproxy.library.caltech.edu/nnano/journal/v6/n3/abs/nnano.2010.279.html>.

- [61] Zelin Jin, Quanwen Liao, Haisheng Fang, Zhichun Liu, Wei Liu, Zhidong Ding, Tengfei Luo, and Nuo Yang. A revisit to high thermoelectric performance of single-layer MoS₂. *Scientific Reports*, 5:18342, December 2015. ISSN 2045-2322. doi: 10.1038/srep18342. URL <http://www.nature.com/srep/2015/151217/srep18342/full/srep18342.html>.
- [62] Zhiwei Ding, Jin-Wu Jiang, Qing-Xiang Pei, and Yong-Wei Zhang. In-plane and cross-plane thermal conductivities of molybdenum disulfide. *Nanotechnology*, 26(6):065703, 2015. ISSN 0957-4484. doi: 10.1088/0957-4484/26/6/065703. URL <http://stacks.iop.org/0957-4484/26/i=6/a=065703>.
- [63] Yongqing Cai, Jinghua Lan, Gang Zhang, and Yong-Wei Zhang. Lattice vibrational modes and phonon thermal conductivity of monolayer MoS₂. *Physical Review B*, 89(3):035438, January 2014. doi: 10.1103/PhysRevB.89.035438. URL <http://link.aps.org/doi/10.1103/PhysRevB.89.035438>.
- [64] Xiaokun Gu, Baowen Li, and Ronggui Yang. Layer thickness-dependent phonon properties and thermal conductivity of MoS₂. *Journal of Applied Physics*, 119(8):085106, 2016. doi: 10.1063/1.4942827. URL <http://dx.doi.org/10.1063/1.4942827>.
- [65] Xiaonan Wang and Alireza Tabarraei. Phonon thermal conductivity of monolayer MoS₂. *Applied Physics Letters*, 108(19):191905, 2016. doi: 10.1063/1.4949561. URL <http://dx.doi.org/10.1063/1.4949561>.
- [66] Wu Li, J. Carrete, and Natalio Mingo. Thermal conductivity and phonon linewidths of monolayer MoS₂ from first principles. *Applied Physics Letters*, 103(25):253103, 2013. doi: 10.1063/1.4850995. URL <http://dx.doi.org/10.1063/1.4850995>.
- [67] Yang Hong, Jingchao Zhang, and Xiao Cheng Zeng. Thermal conductivity of monolayer MoSe₂ and MoS₂. *The Journal of Physical Chemistry C*, 120(45):26067–26075, November 2016. ISSN 1932-7447. doi: 10.1021/acs.jpcc.6b07262. URL <http://dx.doi.org/10.1021/acs.jpcc.6b07262>.
- [68] Daniel O. Lindroth and Paul Erhart. Thermal transport in van der waals solids from first-principles calculations. *Phys. Rev. B*, 94:115205, Sep 2016. doi: 10.1103/PhysRevB.94.115205. URL <https://link.aps.org/doi/10.1103/PhysRevB.94.115205>.
- [69] Xufei Wu, Nuo Yang, and Tengfei Luo. Unusual isotope effect on thermal transport of single layer molybdenum disulphide. *Applied Physics Letters*, 107(19):191907, 2015. doi: 10.1063/1.4935603. URL <http://dx.doi.org/10.1063/1.4935603>.

- [70] Xian Zhang, Dezheng Sun, Yilei Li, Gwan-Hyoung Lee, Xu Cui, Daniel Chenet, Yumeng You, Tony F. Heinz, and James C. Hone. Measurement of lateral and interfacial thermal conductivity of single- and bilayer MoS₂ and MoSe₂ using refined optothermal raman technique. *ACS Applied Materials & Interfaces*, 7(46):25923–25929, November 2015. ISSN 1944-8244. doi: 10.1021/acsami.5b08580. URL <http://dx.doi.org/10.1021/acsami.5b08580>.
- [71] Rusen Yan, Jeffrey R. Simpson, Simone Bertolazzi, Jacopo Brivio, Michael Watson, Xufei Wu, Andras Kis, Tengfei Luo, Angela R. Hight Walker, and Huili Grace Xing. Thermal conductivity of monolayer molybdenum disulfide obtained from temperature-dependent raman spectroscopy. *ACS Nano*, 8(1): 986–993, January 2014. ISSN 1936-0851. doi: 10.1021/nn405826k. URL <http://dx.doi.org/10.1021/nn405826k>.
- [72] Andrzej Taube, Jarosław Judek, Anna Łęcińska, and Mariusz Zdrojek. Temperature-dependent thermal properties of supported MoS₂ monolayers. *ACS Applied Materials & Interfaces*, 7(9):5061–5065, March 2015. ISSN 1944-8244. doi: 10.1021/acsami.5b00690. URL <http://dx.doi.org/10.1021/acsami.5b00690>.
- [73] Satyaprakash Sahoo, Anand P. S. Gaur, Majid Ahmadi, Maxime J.-F. Guinel, and Ram S. Katiyar. Temperature-dependent raman studies and thermal conductivity of few-layer MoS₂. *The Journal of Physical Chemistry C*, 117(17):9042–9047, May 2013. ISSN 1932-7447. doi: 10.1021/jp402509w. URL <http://dx.doi.org/10.1021/jp402509w>.
- [74] Insun Jo, Michael Thompson Pettes, Eric Ou, Wei Wu, and Li Shi. Basal-plane thermal conductivity of few-layer molybdenum disulfide. *Applied Physics Letters*, 104(20):201902, 2014. doi: 10.1063/1.4876965. URL <http://dx.doi.org/10.1063/1.4876965>.
- [75] Jun Liu, Gyung-Min Choi, and David G. Cahill. Measurement of the anisotropic thermal conductivity of molybdenum disulfide by the time-resolved magneto-optic kerr effect. *Journal of Applied Physics*, 116(23): 233107, 2014. doi: 10.1063/1.4904513. URL <http://dx.doi.org/10.1063/1.4904513>.
- [76] J. L. Feldman. Elastic constants of 2H-MoS₂ and 2H-NbSe₂ extracted from measured dispersion curves and linear compressibilities. *Journal of Physics and Chemistry of Solids*, 37(12):1141–1144, January 1976. ISSN 0022-3697. doi: 10.1016/0022-3697(76)90143-8. URL <http://www.sciencedirect.com/science/article/pii/0022369776901438>.
- [77] Kristen Kaasbjerg, Kristian S. Thygesen, and Karsten W. Jacobsen. Phonon-limited mobility in *n*-type single-layer MoS₂ from first principles. *Physical Review B*, 85(11):115317, March 2012. doi: 10.1103/PhysRevB.85.115317. URL <http://link.aps.org/doi/10.1103/PhysRevB.85.115317>.

- [78] Yingchun Ding and Bing Xiao. Thermal expansion tensors, Grüneisen parameters and phonon velocities of bulk MoS_2 ($m = w$ and mo ; $t = s$ and se) from first principles calculations. *RSC Adv.*, 5:18391–18400, 2015. doi: 10.1039/C4RA16966B.
- [79] Wenxu Zhang, Zhishuo Huang, Wanli Zhang, and Yanrong Li. Two-dimensional semiconductors with possible high room temperature mobility. *Nano Research*, 7(12):1731–1737, December 2014. ISSN 1998-0124, 1998-0000. doi: 10.1007/s12274-014-0532-x. URL <https://link.springer.com/article/10.1007/s12274-014-0532-x>.
- [80] H. Peelaers and C. G. Van de Walle. Elastic constants and pressure-induced effects in MoS_2 . *The Journal of Physical Chemistry C*, 118(22):12073–12076, June 2014. ISSN 1932-7447. doi: 10.1021/jp503683h. URL <http://dx.doi.org/10.1021/jp503683h>.
- [81] Shaofeng Ge, Xuefeng Liu, Xiaofen Qiao, Qinsheng Wang, Zhen Xu, Jun Qiu, Ping-Heng Tan, Jimin Zhao, and Dong Sun. Coherent longitudinal acoustic phonon approaching THz frequency in multilayer molybdenum disulfide. *Scientific Reports*, 4:5722, July 2014. ISSN 2045-2322. doi: 10.1038/srep05722. URL <http://www.nature.com/srep/2014/140717/srep05722/full/srep05722.html>.
- [82] B. L. Evans and P. A. Young. Optical absorption and dispersion in molybdenum disulfide. *Proceedings of the Royal Society of London A: Mathematical, Physical and Engineering Sciences*, 284(1398):402–422, March 1965. ISSN 1364-5021, 1471-2946. doi: 10.1098/rspa.1965.0071. URL <http://rspa.royalsocietypublishing.org/content/284/1398/402>.
- [83] Tawinan Cheiwchanamngij and Walter R. L. Lambrecht. Quasiparticle band structure calculation of monolayer, bilayer, and bulk MoS_2 . *Physical Review B*, 85(20):205302, May 2012. doi: 10.1103/PhysRevB.85.205302. URL <http://link.aps.org/doi/10.1103/PhysRevB.85.205302>.
- [84] E. Fortin and W. M. Sears. Photovoltaic effect and optical absorption in MoS_2 . *Journal of Physics and Chemistry of Solids*, 43(9):881 – 884, 1982. ISSN 0022-3697. doi: [http://dx.doi.org/10.1016/0022-3697\(82\)90037-3](http://dx.doi.org/10.1016/0022-3697(82)90037-3). URL <http://www.sciencedirect.com/science/article/pii/0022369782900373>.
- [85] Min-Rui Gao, Jin-Xia Liang, Ya-Rong Zheng, Yun-Fei Xu, Jun Jiang, Qiang Gao, Jun Li, and Shu-Hong Yu. An efficient molybdenum disulfide/cobalt diselenide hybrid catalyst for electrochemical hydrogen generation. *Nature Communications*, 6:5982, January 2015. ISSN 2041-1723. doi: 10.1038/ncomms6982. URL <http://www.nature.com/ncomms/2015/150114/ncomms6982/full/ncomms6982.html>.

- [86] Yi-Hsien Lee, Xin-Quan Zhang, Wenjing Zhang, Mu-Tung Chang, Cheng-Te Lin, Kai-Di Chang, Ya-Chu Yu, Jacob Tse-Wei Wang, Chia-Seng Chang, Lain-Jong Li, and Tsung-Wu Lin. Synthesis of large-area MoS₂ atomic layers with chemical vapor deposition. *Advanced Materials*, 24 (17):2320–2325, May 2012. ISSN 1521-4095. doi: 10.1002/adma.201104798. URL <http://onlinelibrary.wiley.com.clsproxy.library.caltech.edu/doi/10.1002/adma.201104798/abstract>.
- [87] Akira Harata, Hiroyuki Nishimura, and Tsuguo Sawada. Laser-induced surface acoustic waves and photothermal surface gratings generated by crossing two pulsed laser beams. *Applied Physics Letters*, 57(2):132–134, 1990. doi: 10.1063/1.103964. URL <http://dx.doi.org/10.1063/1.103964>.
- [88] John A. Rogers, Alex A. Maznev, and Matthew J. Banet, and Keith A. Nelson. Optical generation and characterization of acoustic waves in thin films: Fundamentals and applications. *Annual Review of Materials Science*, 30(1):117–157, 2000. doi: 10.1146/annurev.matsci.30.1.117. URL <http://dx.doi.org/10.1146/annurev.matsci.30.1.117>.
- [89] Aditya Sood, Feng Xiong, Shunda Chen, Ramez Cheaito, Feifei Lian, Mehdi Asheghi, Yi Cui, Davide Donadio, Kenneth E. Goodson, and Eric Pop. Quasi-ballistic thermal transport across mos₂ thin films. *Nano Letters*, 19 (4):2434–2442, 2019. doi: 10.1021/acs.nanolett.8b05174. URL <https://doi.org/10.1021/acs.nanolett.8b05174>. PMID: 30808167.
- [90] N. Wakabayashi, H. G. Smith, and R. M. Nicklow. Lattice dynamics of hexagonal mos₂ studied by neutron scattering. *Phys. Rev. B*, 12:659–663, Jul 1975. doi: 10.1103/PhysRevB.12.659. URL <https://link.aps.org/doi/10.1103/PhysRevB.12.659>.
- [91] Jong-Young Kim, Soon-Mok Choi, Won-Seon Seo, and Woo-Seok Cho. Thermal and electronic properties of exfoliated metal chalcogenides. *Bulletin of the Korean Chemical Society*, 31 (11):3225–3227, 2010. ISSN 0253-2964. doi: 10.5012/bkcs.2010.31.11.3225. URL http://www.koreascience.or.kr/article/ArticleFullRecord.jsp?cn=JCGMCS_2010_v31n11_3225.
- [92] Ruiqiang Guo, Young-Dahl Jho, and Austin J. Minnich. Coherent control of thermal phonon transport in van der waals superlattices. *Nanoscale*, 10: 14432–14440, 2018. doi: 10.1039/C8NR02150C. URL <http://dx.doi.org/10.1039/C8NR02150C>.
- [93] Hongyu Chen, Valeriy V. Ginzburg, Jian Yang, Yunfeng Yang, Wei Liu, Yan Huang, Libo Du, and Bin Chen. Thermal conductivity of polymer-based composites: Fundamentals and applications. *Progress in Polymer Science*, 59:41–85, August 2016. ISSN 00796700. doi: 10.1016/j.progpolymsci.2016.03.001. URL <https://linkinghub.elsevier.com/retrieve/pii/S0079670016000216>.

- [94] D. Hansen and G. A. Bernier. Thermal conductivity of polyethylene: The effects of crystal size, density and orientation on the thermal conductivity. *Polymer Engineering & Science*, 12(3):204–208, 1972. doi: 10.1002/pen.760120308. URL <https://onlinelibrary.wiley.com/doi/abs/10.1002/pen.760120308>.
- [95] C. L. Choy, W. H. Luk, and F. C. Chen. Thermal conductivity of highly oriented polyethylene. *Polymer*, 19(2):155–162, February 1978. ISSN 0032-3861. doi: 10.1016/0032-3861(78)90032-0. URL <http://www.sciencedirect.com/science/article/pii/0032386178900320>.
- [96] C. L. Choy, Y. W. Wong, G. W. Yang, and Tetsuo Kanamoto. Elastic modulus and thermal conductivity of ultradrawn polyethylene. *Journal of Polymer Science Part B: Polymer Physics*, 37(23):3359–3367, 1999. ISSN 1099-0488. doi: 10.1002/(SICI)1099-0488(19991201)37:23<3359::AID-POLB11>3.0.CO;2-S. URL <https://onlinelibrary.wiley.com/doi/abs/10.1002/%28SICI%291099-0488%2819991201%2937%3A23%3C3359%3A%3AAID-POLB11%3E3.0.CO%3B2-S>.
- [97] B. Taylor, H. J. Maris, and C. Elbaum. Focusing of phonons in crystalline solids due to elastic anisotropy. *Phys. Rev. B*, 3:1462–1472, Feb 1971. doi: 10.1103/PhysRevB.3.1462. URL <https://link.aps.org/doi/10.1103/PhysRevB.3.1462>.
- [98] Peter A. Irvine and Paul Smith. Development of the axial young's modulus with draw ratio of flexible-chain polymers. *Macromolecules*, 19(1):240–242, 1986. doi: 10.1021/ma00155a038. URL <https://doi.org/10.1021/ma00155a038>.
- [99] A. G. Gibson, D. Greig, M. Sahota, I. M. Ward, and C. L. Choy. Thermal conductivity of ultrahigh-modulus polyethylene. *Journal of Polymer Science: Polymer Letters Edition*, 15(4):183–192, 1977. doi: 10.1002/pol.1977.130150401. URL <https://onlinelibrary.wiley.com/doi/abs/10.1002/pol.1977.130150401>.
- [100] Ramesh Shrestha, Pengfei Li, Bikramjit Chatterjee, Teng Zheng, Xufei Wu, Zeyu Liu, Tengfei Luo, Sukwon Choi, Kedar Hippalgaonkar, Maarten P. de Boer, and Sheng Shen. Crystalline polymer nanofibers with ultra-high strength and thermal conductivity. *Nature Communications*, 9(1):1–9, April 2018. ISSN 2041-1723. doi: 10.1038/s41467-018-03978-3. URL <https://www.nature.com/articles/s41467-018-03978-3>.
- [101] Sheng Shen, Asegun Henry, Jonathan Tong, Ruiting Zheng, and Gang Chen. Polyethylene nanofibres with very high thermal conductivities. *Nature Nanotechnology*, 5(4):251–255, April 2010. ISSN 1748-3395. doi: 10.1038/nnano.2010.27. URL <https://www.nature.com/articles/nnano.2010.27>.

- [102] Sanjay Rastogi, Yefeng Yao, Sara Ronca, Johan Bos, and Joris van der Eem. Unprecedented high-modulus high-strength tapes and films of ultrahigh molecular weight polyethylene via solvent-free route. *Macromolecules*, 44(14):5558–5568, 2011. doi: 10.1021/ma200667m. URL <https://doi.org/10.1021/ma200667m>.
- [103] Sara Ronca, Tamito Igarashi, Giuseppe Forte, and Sanjay Rastogi. Metallic-like thermal conductivity in a lightweight insulator: Solid-state processed Ultra High Molecular Weight Polyethylene tapes and films. *Polymer*, 123:203–210, August 2017. ISSN 0032-3861. doi: 10.1016/j.polymer.2017.07.027. URL <http://www.sciencedirect.com/science/article/pii/S0032386117306869>.
- [104] Xiaojia Wang, Victor Ho, Rachel A. Segalman, and David G. Cahill. Thermal conductivity of high-modulus polymer fibers. *Macromolecules*, 46(12):4937–4943, 2013. doi: 10.1021/ma400612y. URL <https://doi.org/10.1021/ma400612y>.
- [105] Chenhao Lu, Sum Wai Chiang, Hongda Du, Jia Li, Lin Gan, Xing Zhang, Xiaodong Chu, Youwei Yao, Baohua Li, and Feiyu Kang. Thermal conductivity of electrospinning chain-aligned polyethylene oxide (peo). *Polymer*, 115:52–59, 2017. ISSN 0032-3861. doi: <https://doi.org/10.1016/j.polymer.2017.02.024>. URL <http://www.sciencedirect.com/science/article/pii/S0032386117301477>.
- [106] Asegun Henry and Gang Chen. High thermal conductivity of single polyethylene chains using molecular dynamics simulations. *Phys. Rev. Lett.*, 101:235502, Dec 2008. doi: 10.1103/PhysRevLett.101.235502. URL <https://link.aps.org/doi/10.1103/PhysRevLett.101.235502>.
- [107] Nina Shulumba, Olle Hellman, and Austin J. Minnich. Lattice thermal conductivity of polyethylene molecular crystals from first-principles including nuclear quantum effects. *Phys. Rev. Lett.*, 119:185901, Oct 2017. doi: 10.1103/PhysRevLett.119.185901. URL <https://link.aps.org/doi/10.1103/PhysRevLett.119.185901>.
- [108] Peishi Cheng, Nina Shulumba, and Austin J. Minnich. Thermal transport and phonon focusing in complex molecular crystals: Ab initio study of polythiophene. *Phys. Rev. B*, 100:094306, Sep 2019. doi: 10.1103/PhysRevB.100.094306. URL <https://link.aps.org/doi/10.1103/PhysRevB.100.094306>.
- [109] Xinjiang Wang, Massoud Kaviani, and Baoling Huang. Phonon coupling and transport in individual polyethylene chains: a comparison study with the bulk crystal. *Nanoscale*, 9(45):18022–18031, 2017. doi: 10.1039/C7NR06216H. URL <http://dx.doi.org/10.1039/C7NR06216H>.

- [110] Zhibin Ye, Shiping Zhu, Wen-Jun Wang, Hatem Alsyouri, and Y. S. Lin. Morphological and mechanical properties of nascent polyethylene fibers produced via ethylene extrusion polymerization with a metallocene catalyst supported on mcm-41 particles. *Journal of Polymer Science Part B: Polymer Physics*, 41(20):2433–2443, 2003. doi: 10.1002/polb.10588. URL <https://onlinelibrary.wiley.com/doi/abs/10.1002/polb.10588>.
- [111] K. Anandakumaran, S. K. Roy, and R. St. John Manley. Drawing-induced changes in the properties of polyethylene fibers prepared by gelation/crystallization. *Macromolecules*, 21(6):1746–1751, 1988. doi: 10.1021/ma00184a036. URL <https://doi.org/10.1021/ma00184a036>.
- [112] Toshio Mugishima, Yoshiaki Kogure, Yosio Hiki, Kenji Kawasaki, and Hiroaki Nakamura. Phonon conduction in polyethylene. *Journal of the Physical Society of Japan*, 57(6):2069–2079, 1988.
- [113] A. Peterlin. Crystalline character in polymers. *Journal of Polymer Science Part C: Polymer Symposia*, 9(1):61–89, 1965. doi: 10.1002/polc.5070090106. URL <https://onlinelibrary.wiley.com/doi/abs/10.1002/polc.5070090106>.
- [114] A. Peterlin. Drawing and extrusion of semi-crystalline polymers. *Colloid and Polymer Science*, 265(5):357–382, 1987. doi: 10.1007/BF01412215. URL <https://doi.org/10.1007/BF01412215>.
- [115] N. A. J. M. Van Aerle and A. W. M. Braam. A structural study on solid state drawing of solution-crystallized ultra-high molecular weight polyethylene. *Journal of Materials Science*, 23(12):4429–4436, 1988. doi: 10.1007/BF00551941. URL <https://doi.org/10.1007/BF00551941>.
- [116] K. Kaji, T. Mochizuki, A. Akiyama, and R. Hosemann. Crystallite size determination and identification of lamellar surfaces of microparacrystallites for uniaxially and doubly oriented polyethylene films. *Journal of Materials Science*, 13(5):972–984, 1978. doi: 10.1007/BF00544692. URL <https://doi.org/10.1007/BF00544692>.
- [117] Kenichi Furuhashi, Takuya Yokokawa, Chang Seoul, and Keizo Miyasaka. Drawing of ultrahigh-molecular-weight polyethylene single-crystal mats: The crystallinity. *Journal of Polymer Science Part B: Polymer Physics*, 24(1):59–67, 1986. doi: 10.1002/polb.1986.180240107. URL <https://onlinelibrary.wiley.com/doi/abs/10.1002/polb.1986.180240107>.
- [118] Paul Smith and Piet J. Lemstra. Ultra-high-strength polyethylene filaments by solution spinning/drawing. *Journal of Materials Science*, 15(2):505–514, 1980. doi: 10.1007/BF00551705. URL <https://doi.org/10.1007/BF00551705>.

- [119] Y. A. Zubov, S. N. Chvalun, V. I. Selikhova, M. B. Konstantinopolskaya, and N. Ph. Bakeev. The structure of highly oriented high modulus polyethylene. *Polymer Engineering & Science*, 32(17):1316–1324, 1992. doi: 10.1002/pen.760321720. URL <https://onlinelibrary.wiley.com/doi/abs/10.1002/pen.760321720>.
- [120] V. M. Litvinov, Jianjun Xu, C. Melian, D. E. Demco, M. Möller, and J. Simmelink. Morphology, chain dynamics, and domain sizes in highly drawn gel-spun ultrahigh molecular weight polyethylene fibers at the final stages of drawing by saxs, waxes, and 1h solid-state nmr. *Macromolecules*, 44(23):9254–9266, 2011. doi: 10.1021/ma201888f. URL <https://doi.org/10.1021/ma201888f>.
- [121] J. Clements and I.M. Ward. Crystallite thickness measurements on ultrahigh modulus linear polyethylene: effect of draw temperature. *Polymer*, 24(1):27 – 29, 1983. ISSN 0032-3861. doi: [https://doi.org/10.1016/0032-3861\(83\)90075-7](https://doi.org/10.1016/0032-3861(83)90075-7). URL <http://www.sciencedirect.com/science/article/pii/0032386183900757>.
- [122] A. Peterlin and R. Corneliussen. Small-angle x-ray diffraction studies of plastically deformed polyethylene. ii. influence of draw temperature, draw ratio, annealing temperature, and time. *Journal of Polymer Science Part A-2: Polymer Physics*, 6(7):1273–1282, 1968. doi: 10.1002/pol.1968.160060706. URL <https://onlinelibrary.wiley.com/doi/abs/10.1002/pol.1968.160060706>.
- [123] A. Peterlin and F. J. Baltá-Calleja. Plastic deformation of polypropylene. iii. small-angle x-ray scattering in the neck region. *Journal of Applied Physics*, 40(11):4238–4242, 1969. doi: 10.1063/1.1657181. URL <https://doi.org/10.1063/1.1657181>.
- [124] W.-G Hu and K Schmidt-Rohr. Characterization of ultradrawn polyethylene fibers by nmr: crystallinity, domain sizes and a highly mobile second amorphous phase. *Polymer*, 41(8):2979 – 2987, 2000. ISSN 0032-3861. doi: [https://doi.org/10.1016/S0032-3861\(99\)00429-2](https://doi.org/10.1016/S0032-3861(99)00429-2). URL <http://www.sciencedirect.com/science/article/pii/S0032386199004292>.
- [125] Jean M. Brady and Edwin L. Thomas. Conversion of single crystal mats to ultrahigh modulus polyethylene: the formation of a continuous crystalline phase. *Polymer*, 30(9):1615 – 1622, 1989. ISSN 0032-3861. doi: [https://doi.org/10.1016/0032-3861\(89\)90320-0](https://doi.org/10.1016/0032-3861(89)90320-0). URL <http://www.sciencedirect.com/science/article/pii/0032386189903200>.
- [126] Paul Smith, Alain Boudet, and Henri Chanzy. The structure of ultradrawn high molecular weight polyethylene revealed by electron microscopy at 100 and 1500 kV. *Journal of Materials Science Letters*, 4(1):13–18, January 1985. ISSN 0261-8028, 1573-4811. doi: 10.1007/BF00719883. URL <http://link.springer.com/10.1007/BF00719883>.

- [127] Yujing Tang, Zhiyong Jiang, Yongfeng Men, Lijia An, Hans-Friedrich Endlerle, Dieter Lilge, Stephan V. Roth, Rainer Gehrke, and Jens Rieger. Uniaxial deformation of overstretched polyethylene: In-situ synchrotron small angle x-ray scattering study. *Polymer*, 48(17):5125 – 5132, 2007. ISSN 0032-3861. doi: <https://doi.org/10.1016/j.polymer.2007.06.056>. URL <http://www.sciencedirect.com/science/article/pii/S0032386107006313>.
- [128] Jürgen Hennig. Anisotropy and structure in uniaxially stretched amorphous high polymers. *Journal of Polymer Science Part C: Polymer Symposia*, 16(5):2751–2761, 1967. doi: 10.1002/polc.5070160528. URL <https://onlinelibrary.wiley.com/doi/abs/10.1002/polc.5070160528>.
- [129] C.L. Choy. Thermal conductivity of polymers. *Polymer*, 18(10):984 – 1004, 1977. ISSN 0032-3861. doi: [https://doi.org/10.1016/0032-3861\(77\)90002-7](https://doi.org/10.1016/0032-3861(77)90002-7). URL <http://www.sciencedirect.com/science/article/pii/0032386177900027>.
- [130] Motowo Takayanagi, Shinsaku Uemura, and Shunsuke Minami. Application of equivalent model method to dynamic rheo-optical properties of crystalline polymer. *Journal of Polymer Science Part C: Polymer Symposia*, 5(1):113–122, 1964. doi: 10.1002/polc.5070050111. URL <https://onlinelibrary.wiley.com/doi/abs/10.1002/polc.5070050111>.
- [131] Andrew B. Robbins, Stavros X. Drakopoulos, Ignacio Martin-Fabiani, Sara Ronca, and Austin J. Minnich. Ballistic thermal phonons traversing nanocrystalline domains in oriented polyethylene. *Proceedings of the National Academy of Sciences*, 116(35):17163–17168, August 2019. ISSN 0027-8424, 1091-6490. doi: 10.1073/pnas.1905492116. URL <https://www.pnas.org/content/116/35/17163>.
- [132] Stavros X. Drakopoulos, Oreste Tarallo, Linlin Guan, Ignacio Martin-Fabiani, and Sara Ronca. Nanocomposites of Au/Disentangled UHMWPE: A Combined Optical and Structural Study. *Molecules*, 25(14):3225, January 2020. doi: 10.3390/molecules25143225. URL <https://www.mdpi.com/1420-3049/25/14/3225>. Number: 14 Publisher: Multidisciplinary Digital Publishing Institute.
- [133] Stavros Drakopoulos. Disentangled ultra-high molecular weight polyethylene and its nanocomposites: relaxation dynamics, entanglement formation and anisotropic properties due to orientation. 12 2019. doi: 10.26174/thesis.lboro.11324012.v1. URL https://repository.lboro.ac.uk/articles/thesis/Disentangled_ultra-high_molecular_weight_polyethylene_and_its_nanocomposites_relaxation_dynamics_entanglement_formation_and_anisotropic_properties_due_to_orientation/11324012.
- [134] Andrew Beyer Robbins. *Exploring Microscopic Thermal Transport Properties of Molecular Crystals with Simulations and Experiments*. phd, California

Institute of Technology, 2019. URL <https://resolver.caltech.edu/CaltechTHESIS:02062019-144758624>.

- [135] SS Chang. Heat capacities of polyethylene from 2 to 360 k. ii. two high density linear polyethylene samples and thermodynamic properties of crystalline linear polyethylene. *J. Res. NBS A Phys. Chem*, 3, 1974.
- [136] J. Hone, M. Whitney, C. Piskoti, and A. Zettl. Thermal conductivity of single-walled carbon nanotubes. *Phys. Rev. B*, 59:R2514–R2516, Jan 1999. doi: 10.1103/PhysRevB.59.R2514. URL <https://link.aps.org/doi/10.1103/PhysRevB.59.R2514>.
- [137] Jin Yu, Rajiv K. Kalia, and Priya Vashishta. Phonons in graphitic tubules: A tight-binding molecular dynamics study. *The Journal of Chemical Physics*, 103(15):6697–6705, 1995. doi: 10.1063/1.470400. URL <https://doi.org/10.1063/1.470400>.
- [138] Lorin X. Benedict, Steven G. Louie, and Marvin L. Cohen. Heat capacity of carbon nanotubes. *Solid State Communications*, 100(3):177 – 180, 1996. ISSN 0038-1098. doi: [https://doi.org/10.1016/0038-1098\(96\)00386-9](https://doi.org/10.1016/0038-1098(96)00386-9). URL <http://www.sciencedirect.com/science/article/pii/0038109896003869>.
- [139] C. L. Choy, Y. Fei, and T. G. Xi. Thermal conductivity of gel-spun polyethylene fibers. *Journal of Polymer Science Part B: Polymer Physics*, 31(3):365–370, 1993. doi: 10.1002/polb.1993.090310315. URL <https://onlinelibrary.wiley.com/doi/abs/10.1002/polb.1993.090310315>.
- [140] D. B. Mergenthaler and M. Pietralla. Heat conduction in highly oriented polyethylene. *Zeitschrift für Physik B Condensed Matter*, 94(4):461–468, 1994. doi: 10.1007/BF01317408. URL <https://doi.org/10.1007/BF01317408>.
- [141] Bowen Zhu, Jing Liu, Tianyu Wang, Meng Han, Shah Valloppilly, Shen Xu, and Xinwei Wang. Novel polyethylene fibers of very high thermal conductivity enabled by amorphous restructuring. *ACS Omega*, 2(7):3931–3944, 2017. doi: 10.1021/acsomega.7b00563. URL <https://doi.org/10.1021/acsomega.7b00563>.
- [142] Hiroyuki Fujishiro, Manabu Ikebe, Toshihiro Kashima, and Atsuhiko Yamanaka. Thermal conductivity and diffusivity of high-strength polymer fibers. *Japanese Journal of Applied Physics*, 36(Part 1, No. 9A):5633–5637, sep 1997. doi: 10.1143/jjap.36.5633. URL <https://doi.org/10.1143/2Fjjap.36.5633>.
- [143] Bernhard Wunderlich. Motion in polyethylene. i. temperature and crystallinity dependence of the specific heat. *The Journal of Chemical Physics*, 37(6):

- 1203–1207, 1962. doi: 10.1063/1.1733266. URL <https://doi.org/10.1063/1.1733266>.
- [144] V. K Malinovsky, V. N Novikov, P. P Parshin, A. P Sokolov, and M. G Zemlyanov. Universal form of the low-energy (2 to 10 meV) vibrational spectrum of glasses. *Europhysics Letters (EPL)*, 11(1):43–47, jan 1990. doi: 10.1209/0295-5075/11/1/008. URL <https://doi.org/10.1209/0295-5075/11/1/008>.
- [145] X Liu and H. v Löhneysen. Specific-heat anomaly of amorphous solids at intermediate temperatures (1 to 30 k). *Europhysics Letters (EPL)*, 33(8):617–622, mar 1996. doi: 10.1209/epl/i1996-00388-9. URL <https://doi.org/10.1209/epl/i1996-00388-9>.
- [146] J. Jäckle, L. Piché, W. Arnold, and S. Hunklinger. Elastic effects of structural relaxation in glasses at low temperatures. *Journal of Non-Crystalline Solids*, 20(3):365–391, May 1976. ISSN 0022-3093. doi: 10.1016/0022-3093(76)90119-8. URL <http://www.sciencedirect.com/science/article/pii/0022309376901198>.
- [147] W. A. Phillips. Tunneling states in amorphous solids. *Journal of Low Temperature Physics*, 7(3):351–360, 1972. doi: 10.1007/BF00660072. URL <https://doi.org/10.1007/BF00660072>.
- [148] S. HUNKLINGER and W. ARNOLD. 3 - ultrasonic properties of glasses at low temperatures. volume 12 of *Physical Acoustics*, pages 155 – 215. Academic Press, 1976. doi: <https://doi.org/10.1016/B978-0-12-477912-9.50008-4>. URL <http://www.sciencedirect.com/science/article/pii/B9780124779129500084>.
- [149] P. W. Anderson, B. I. Halperin, and C. M. Varma. Anomalous low-temperature thermal properties of glasses and spin glasses. *The Philosophical Magazine: A Journal of Theoretical Experimental and Applied Physics*, 25(1):1–9, 1972. doi: 10.1080/14786437208229210. URL <https://doi.org/10.1080/14786437208229210>.
- [150] M. P. Zaitlin and A. C. Anderson. An explanation for the plateau in the thermal conductivity of non-crystalline solids. *physica status solidi (b)*, 71(1):323–327, 1975. doi: 10.1002/pssb.2220710132. URL <https://onlinelibrary.wiley.com/doi/abs/10.1002/pssb.2220710132>.
- [151] Jaeyun Moon, Raphaël P. Hermann, Michael E. Manley, Ahmet Alatas, Ayman H. Said, and Austin J. Minnich. Thermal acoustic excitations with atomic-scale wavelengths in amorphous silicon. *Phys. Rev. Materials*, 3: 065601, Jun 2019. doi: 10.1103/PhysRevMaterials.3.065601. URL <https://link.aps.org/doi/10.1103/PhysRevMaterials.3.065601>.

- [152] Giulio Monaco and Valentina M. Giordano. Breakdown of the Debye approximation for the acoustic modes with nanometric wavelengths in glasses. *Proceedings of the National Academy of Sciences*, 106(10):3659–3663, March 2009. ISSN 0027-8424, 1091-6490. doi: 10.1073/pnas.0808965106. URL <https://www.pnas.org/content/106/10/3659>.
- [153] B. Rufflé, G. Guimbretière, E. Courtens, R. Vacher, and G. Monaco. Glass-specific behavior in the damping of acousticlike vibrations. *Phys. Rev. Lett.*, 96:045502, Jan 2006. doi: 10.1103/PhysRevLett.96.045502. URL <https://link.aps.org/doi/10.1103/PhysRevLett.96.045502>.
- [154] C. Masciovecchio, G. Ruocco, F. Sette, M. Krisch, R. Verbeni, U. Bergmann, and M. Soltwisch. Observation of large momentum phononlike modes in glasses. *Phys. Rev. Lett.*, 76:3356–3359, Apr 1996. doi: 10.1103/PhysRevLett.76.3356. URL <https://link.aps.org/doi/10.1103/PhysRevLett.76.3356>.
- [155] Francesco Sette, Michael H. Krisch, Claudio Masciovecchio, Giancarlo Ruocco, and Giulio Monaco. Dynamics of glasses and glass-forming liquids studied by inelastic x-ray scattering. *Science*, 280(5369):1550–1555, 1998. ISSN 0036-8075. doi: 10.1126/science.280.5369.1550. URL <https://science.sciencemag.org/content/280/5369/1550>.
- [156] W. Dietsche and H. Kinder. Spectroscopy of Phonon Scattering in Glass. *Physical Review Letters*, 43(19):1413–1417, November 1979. doi: 10.1103/PhysRevLett.43.1413. URL <https://link.aps.org/doi/10.1103/PhysRevLett.43.1413>.
- [157] R. Vacher, H. Sussner, and S. Hunklinger. Brillouin scattering in vitreous silica below 1 k. *Phys. Rev. B*, 21:5850–5853, Jun 1980. doi: 10.1103/PhysRevB.21.5850. URL <https://link.aps.org/doi/10.1103/PhysRevB.21.5850>.
- [158] R. Vacher and J. Pelous. Behavior of thermal phonons in amorphous media from 4 to 300 k. *Phys. Rev. B*, 14:823–828, Jul 1976. doi: 10.1103/PhysRevB.14.823. URL <https://link.aps.org/doi/10.1103/PhysRevB.14.823>.
- [159] P. Benassi, S. Caponi, R. Eramo, A. Fontana, A. Giugni, M. Nardone, M. Sampoli, and G. Viliiani. Sound attenuation in a unexplored frequency region: Brillouin ultraviolet light scattering measurements in ν -SiO₂. *Phys. Rev. B*, 71:172201, May 2005. doi: 10.1103/PhysRevB.71.172201. URL <https://link.aps.org/doi/10.1103/PhysRevB.71.172201>.
- [160] T. C. Zhu, H. J. Maris, and J. Tauc. Attenuation of longitudinal-acoustic phonons in amorphous sio₂ at frequencies up to 440 ghz. *Phys. Rev. B*, 44:4281–4289, Sep 1991. doi: 10.1103/PhysRevB.44.4281. URL <https://link.aps.org/doi/10.1103/PhysRevB.44.4281>.

- [161] A. Devos, M. Foret, S. Ayrihac, P. Emery, and B. Rufflé. Hypersound damping in vitreous silica measured by picosecond acoustics. *Phys. Rev. B*, 77:100201, Mar 2008. doi: 10.1103/PhysRevB.77.100201. URL <https://link.aps.org/doi/10.1103/PhysRevB.77.100201>.
- [162] J. J. Freeman and A. C. Anderson. Thermal conductivity of amorphous solids. *Phys. Rev. B*, 34:5684–5690, Oct 1986. doi: 10.1103/PhysRevB.34.5684. URL <https://link.aps.org/doi/10.1103/PhysRevB.34.5684>.
- [163] K. E. Goodson, M. I. Flik, L. T. Su, and D. A. Antoniadis. Prediction and Measurement of the Thermal Conductivity of Amorphous Dielectric Layers. *Journal of Heat Transfer*, 116(2):317–324, 05 1994. ISSN 0022-1481. doi: 10.1115/1.2911402. URL <https://doi.org/10.1115/1.2911402>.
- [164] J. E. Graebner, B. Golding, and L. C. Allen. Phonon localization in glasses. *Phys. Rev. B*, 34:5696–5701, Oct 1986. doi: 10.1103/PhysRevB.34.5696. URL <https://link.aps.org/doi/10.1103/PhysRevB.34.5696>.
- [165] M. Von Haumer, U. Strom, and S. Hunklinger. Acoustic Anomalies in Amorphous Thin Films of Si and SiO₂. *Physical Review Letters*, 44(2):84–87, January 1980. doi: 10.1103/PhysRevLett.44.84. URL <https://link.aps.org/doi/10.1103/PhysRevLett.44.84>.
- [166] L. Wiczorek, H. J. Goldsmid, and G. L. Paul. *Thermal Conductivity of Amorphous Films*, pages 235–241. Springer US, Boston, MA, 1989. ISBN 978-1-4613-0761-7. doi: 10.1007/978-1-4613-0761-7_22. URL https://doi.org/10.1007/978-1-4613-0761-7_22.
- [167] B. S. W. Kuo, J. C. M. Li, and A. W. Schmid. Thermal conductivity and interface thermal resistance of si film on si substrate determined by photothermal displacement interferometry. *Applied Physics A*, 55(3):289–296, 1992. doi: 10.1007/BF00348399. URL <https://doi.org/10.1007/BF00348399>.
- [168] Seungjae Moon, Mutsuko Hatano, Minghong Lee, and Costas P. Grigoropoulos. Thermal conductivity of amorphous silicon thin films. *International Journal of Heat and Mass Transfer*, 45(12):2439–2447, June 2002. ISSN 00179310. doi: 10.1016/S0017-9310(01)00347-7. URL <http://linkinghub.elsevier.com/retrieve/pii/S0017931001003477>.
- [169] Xiao Liu, J. L. Feldman, D. G. Cahill, R. S. Crandall, N. Bernstein, D. M. Photiadis, M. J. Mehl, and D. A. Papaconstantopoulos. High thermal conductivity of a hydrogenated amorphous silicon film. *Phys. Rev. Lett.*, 102:035901, Jan 2009. doi: 10.1103/PhysRevLett.102.035901. URL <https://link.aps.org/doi/10.1103/PhysRevLett.102.035901>.
- [170] Jeffrey L. Braun, Christopher H. Baker, Ashutosh Giri, Mirza Elahi, Kateryna Artyushkova, Thomas E. Beechem, Pamela M. Norris, Zayd C. Leseman,

- John T. Gaskins, and Patrick E. Hopkins. Size effects on the thermal conductivity of amorphous silicon thin films. *Phys. Rev. B*, 93:140201, Apr 2016. doi: 10.1103/PhysRevB.93.140201. URL <https://link.aps.org/doi/10.1103/PhysRevB.93.140201>.
- [171] Jason M. Larkin and Alan J. H. McGaughey. Thermal conductivity accumulation in amorphous silica and amorphous silicon. *Phys. Rev. B*, 89:144303, Apr 2014. doi: 10.1103/PhysRevB.89.144303. URL <https://link.aps.org/doi/10.1103/PhysRevB.89.144303>.
- [172] K. Säskilähti, J. Oksanen, J. Tulkki, A. J. H. McGaughey, and S. Volz. Vibrational mean free paths and thermal conductivity of amorphous silicon from non-equilibrium molecular dynamics simulations. *AIP Advances*, 6(12):121904, 2016. doi: 10.1063/1.4968617. URL <https://doi.org/10.1063/1.4968617>.
- [173] Jeremy A. Johnson, A. A. Maznev, John Cuffe, Jeffrey K. Eliason, Austin J. Minnich, Timothy Kehoe, Clivia M. Sotomayor Torres, Gang Chen, and Keith A. Nelson. Direct measurement of room-temperature nondiffusive thermal transport over micron distances in a silicon membrane. *Phys. Rev. Lett.*, 110:025901, Jan 2013. doi: 10.1103/PhysRevLett.110.025901. URL <https://link.aps.org/doi/10.1103/PhysRevLett.110.025901>.
- [174] Jaeyun Moon, Benoit Latour, and Austin J. Minnich. Propagating elastic vibrations dominate thermal conduction in amorphous silicon. *Phys. Rev. B*, 97:024201, Jan 2018. doi: 10.1103/PhysRevB.97.024201. URL <https://link.aps.org/doi/10.1103/PhysRevB.97.024201>.
- [175] J. T. KRAUSE and C. R. KURKJIAN. Vibrational anomalies in inorganic glass formers. *Journal of the American Ceramic Society*, 51(4):226–227, 1968. doi: 10.1111/j.1151-2916.1968.tb11880.x. URL <https://ceramics.onlinelibrary.wiley.com/doi/abs/10.1111/j.1151-2916.1968.tb11880.x>.
- [176] R. E. Strakna and H. T. Savage. Ultrasonic relaxation loss in SiO_2 , GeO_2 , B_2O_3 , and As_2O_3 glass. *Journal of Applied Physics*, 35(5):1445–1450, 1964. doi: 10.1063/1.1713648. URL <https://doi.org/10.1063/1.1713648>.
- [177] D G Cahill and R O Pohl. Lattice vibrations and heat transport in crystals and glasses. *Annual Review of Physical Chemistry*, 39(1):93–121, 1988. doi: 10.1146/annurev.pc.39.100188.000521. URL <https://doi.org/10.1146/annurev.pc.39.100188.000521>.
- [178] Robert O. Pohl, Xiao Liu, and EunJoo Thompson. Low-temperature thermal conductivity and acoustic attenuation in amorphous solids. *Rev. Mod. Phys.*, 74:991–1013, Oct 2002. doi: 10.1103/RevModPhys.74.991. URL <https://link.aps.org/doi/10.1103/RevModPhys.74.991>.

- [179] J.C. Lasjaunias and R. Maynard. Analysis of the specific heat and thermal conductivity of vitreous selenium above 1 k. *Journal of Non-Crystalline Solids*, 6(2):101 – 106, 1971. ISSN 0022-3093. doi: [https://doi.org/10.1016/0022-3093\(71\)90048-2](https://doi.org/10.1016/0022-3093(71)90048-2). URL <http://www.sciencedirect.com/science/article/pii/0022309371900482>.
- [180] A.J. Leadbetter, A.P. Jeapes, C.G. Waterfield, and K.E. Wycherley. The low temperature heat capacity of some glass ceramics. *Chemical Physics Letters*, 52(3):469 – 472, 1977. ISSN 0009-2614. doi: [https://doi.org/10.1016/0009-2614\(77\)80487-9](https://doi.org/10.1016/0009-2614(77)80487-9). URL <http://www.sciencedirect.com/science/article/pii/0009261477804879>.
- [181] M. S. Love and A. C. Anderson. Estimate of phonon thermal transport in amorphous materials above 50 k. *Phys. Rev. B*, 42:1845–1847, Jul 1990. doi: [10.1103/PhysRevB.42.1845](https://doi.org/10.1103/PhysRevB.42.1845). URL <https://link.aps.org/doi/10.1103/PhysRevB.42.1845>.
- [182] D. Walton. Random-network model, density fluctuation, and thermal conductivity of glasses. *Solid State Communications*, 14(4):335 – 339, 1974. ISSN 0038-1098. doi: [https://doi.org/10.1016/0038-1098\(74\)90913-2](https://doi.org/10.1016/0038-1098(74)90913-2). URL <http://www.sciencedirect.com/science/article/pii/0038109874909132>.
- [183] Josef Jäckle. On the ultrasonic attenuation in glasses at low temperatures. *Zeitschrift für Physik A Hadrons and nuclei*, 257:212–223, 1972.
- [184] K. A. Topp and David G. Cahill. Elastic properties of several amorphous solids and disordered crystals below 100 k. *Zeitschrift für Physik B Condensed Matter*, 101(2):235–245, 1996. doi: [10.1007/s002570050205](https://doi.org/10.1007/s002570050205). URL <https://doi.org/10.1007/s002570050205>.
- [185] David G. Cahill and R.O. Pohl. Heat flow and lattice vibrations in glasses. *Solid State Communications*, 70(10):927 – 930, 1989. ISSN 0038-1098. doi: [https://doi.org/10.1016/0038-1098\(89\)90630-3](https://doi.org/10.1016/0038-1098(89)90630-3). URL <http://www.sciencedirect.com/science/article/pii/0038109889906303>.
- [186] David G. Cahill, S. K. Watson, and R. O. Pohl. Lower limit to the thermal conductivity of disordered crystals. *Phys. Rev. B*, 46:6131–6140, Sep 1992. doi: [10.1103/PhysRevB.46.6131](https://doi.org/10.1103/PhysRevB.46.6131). URL <https://link.aps.org/doi/10.1103/PhysRevB.46.6131>.
- [187] A. Einstein. Elementare betrachtungen über die thermische molekularbewegung in festen körpern. *Annalen der Physik*, 340(9):679–694, 1911. doi: [10.1002/andp.19113400903](https://doi.org/10.1002/andp.19113400903). URL <https://onlinelibrary.wiley.com/doi/abs/10.1002/andp.19113400903>.
- [188] David Turnbull and Morrel H. Cohen. Free-volume model of the amorphous phase: Glass transition. *The Journal of Chemical Physics*, 34(1):120–125,

1961. doi: 10.1063/1.1731549. URL <https://doi.org/10.1063/1.1731549>.
- [189] C. Thomsen, H. T. Grahn, D. Young, H. J. Maris, and J. Tauc. Picosecond acoustic interferometry. In Ansel C. Anderson and James P. Wolfe, editors, *Phonon Scattering in Condensed Matter V*, pages 392–394, Berlin, Heidelberg, 1986. Springer Berlin Heidelberg. ISBN 978-3-642-82912-3.
- [190] Aaron Jerome Schmidt. *Optical characterization of thermal transport from the nanoscale to the macroscale*. Thesis, Massachusetts Institute of Technology, 2008. URL <http://dspace.mit.edu/handle/1721.1/44798>.
- [191] Richard L. Cole, B. George Barisas, and Nancy E. Levinger. Logarithmic based optical delay for time-resolved data collection. *Review of Scientific Instruments*, 81(9):093101, 2010. doi: 10.1063/1.3474226. URL <https://doi.org/10.1063/1.3474226>.
- [192] Walter G. Mayer and E. A. Hiedemann. Optical methods for the ultrasonic determination of the elastic constants of sapphire. *The Journal of the Acoustical Society of America*, 30(8):756–760, 1958. doi: 10.1121/1.1909753. URL <https://doi.org/10.1121/1.1909753>.
- [193] B. C. Daly, K. Kang, Y. Wang, and David G. Cahill. Picosecond ultrasonic measurements of attenuation of longitudinal acoustic phonons in silicon. *Phys. Rev. B*, 80:174112, Nov 2009. doi: 10.1103/PhysRevB.80.174112. URL <https://link.aps.org/doi/10.1103/PhysRevB.80.174112>.
- [194] C. J. Morath and H. J. Maris. Phonon attenuation in amorphous solids studied by picosecond ultrasonics. *Phys. Rev. B*, 54:203–213, Jul 1996. doi: 10.1103/PhysRevB.54.203. URL <https://link.aps.org/doi/10.1103/PhysRevB.54.203>.
- [195] C. Klieber, E. Peronne, K. Katayama, J. Choi, M. Yamaguchi, T. Pezeril, and Keith A. Nelson. Narrow-band acoustic attenuation measurements in vitreous silica at frequencies between 20 and 400 ghz. *Applied Physics Letters*, 98(21):211908, 2011. doi: 10.1063/1.3595275. URL <https://doi.org/10.1063/1.3595275>.
- [196] D. R. Queen, X. Liu, J. Karel, T. H. Metcalf, and F. Hellman. Excess specific heat in evaporated amorphous silicon. *Phys. Rev. Lett.*, 110:135901, Mar 2013. doi: 10.1103/PhysRevLett.110.135901. URL <https://link.aps.org/doi/10.1103/PhysRevLett.110.135901>.
- [197] David G. Cahill, M. Katiyar, and J. R. Abelson. Thermal conductivity of a-si:h thin films. *Phys. Rev. B*, 50:6077–6081, Sep 1994. doi: 10.1103/PhysRevB.50.6077. URL <https://link.aps.org/doi/10.1103/PhysRevB.50.6077>.

- [198] B. L. Zink, R. Pietri, and F. Hellman. Thermal conductivity and specific heat of thin-film amorphous silicon. *Phys. Rev. Lett.*, 96:055902, Feb 2006. doi: 10.1103/PhysRevLett.96.055902. URL <https://link.aps.org/doi/10.1103/PhysRevLett.96.055902>.
- [199] Philip B. Allen and Joseph L. Feldman. Thermal conductivity of disordered harmonic solids. *Phys. Rev. B*, 48:12581–12588, Nov 1993. doi: 10.1103/PhysRevB.48.12581. URL <https://link.aps.org/doi/10.1103/PhysRevB.48.12581>.
- [200] Joseph L. Feldman, Mark D. Kluge, Philip B. Allen, and Frederick Wooten. Thermal conductivity and localization in glasses: Numerical study of a model of amorphous silicon. *Phys. Rev. B*, 48:12589–12602, Nov 1993. doi: 10.1103/PhysRevB.48.12589. URL <https://link.aps.org/doi/10.1103/PhysRevB.48.12589>.
- [201] M. P. Zaitlin and A. C. Anderson. Phonon thermal transport in noncrystalline materials. *Phys. Rev. B*, 12:4475–4486, Nov 1975. doi: 10.1103/PhysRevB.12.4475. URL <https://link.aps.org/doi/10.1103/PhysRevB.12.4475>.
- [202] Yuping He, Davide Donadio, and Giulia Galli. Heat transport in amorphous silicon: Interplay between morphology and disorder. *Applied Physics Letters*, 98(14):144101, 2011. doi: 10.1063/1.3574366. URL <https://doi.org/10.1063/1.3574366>.
- [203] Anthony J. C. Ladd, Bill Moran, and William G. Hoover. Lattice thermal conductivity: A comparison of molecular dynamics and anharmonic lattice dynamics. *Phys. Rev. B*, 34:5058–5064, Oct 1986. doi: 10.1103/PhysRevB.34.5058. URL <https://link.aps.org/doi/10.1103/PhysRevB.34.5058>.
- [204] A. J. H. McGaughey and M. Kaviani. Quantitative validation of the boltzmann transport equation phonon thermal conductivity model under the single-mode relaxation time approximation. *Phys. Rev. B*, 69:094303, Mar 2004. doi: 10.1103/PhysRevB.69.094303. URL <https://link.aps.org/doi/10.1103/PhysRevB.69.094303>.
- [205] Piers Coleman. *Introduction to Many-Body Physics*. Cambridge University Press, 2015. doi: 10.1017/CBO9781139020916. URL <https://doi.org/10.1017/CBO9781139020916>.